



AALBORG UNIVERSITY
DENMARK

Design of Mechanical Systems

MASTER THESIS

SPRING 2017

**Inverse Parameter Identification for
Multilinear Cohesive Laws**

GROUP 1.121 B

MARIO JAVIER MARTOS SANCHEZ AND SIMON MOSBJERG JENSEN



AALBORG UNIVERSITY
STUDENT REPORT

**Study Board of Industry and Global
Business Development**

Design of Mechanical Systems

Fibigerstræde 16, 9220 Aalborg

Phone +45 99 40 93 09

<http://info@m-tech.aau.dk>

Title:

Inverse Parameter Identification for
Multilinear Cohesive Laws

Theme:

Fracture Mechanics, Finite element
modeling, Interface elements, Con-
stitutive Relations and Optimiza-
tion

Semester:

DMS4, Spring semester 2017

Semester theme:

Master Thesis

Project duration:

01/02/2017 to 02/05/2017

ECTS:

30

Project group:

1.121 B

Authors:

Simon Mosbjerg Jensen
Mario Javier Martos Sanchez

Supervisors:

Esben Lindgaard
Brian L. V. Bak

Number of pages:

111

Submission date:

02/05/2017

Synopsis:

Through this report a methodology for characterization of fracture related parameters for numerical modelling of delamination in composite materials is developed. The methodology relies on concepts of inverse parameter identification and optimization techniques. The numerical modelling is done through use of the finite element method and cohesive zone modelling.

An experiment is simulated in a parametric finite element model and a residual is defined as the discrepancy in some given response from the numerical model and the physical experiment. The parameter identification is then done by minimization of the residual.

The crack propagation is modelled using user-defined interface elements through ANSYS. A mixed mode multilinear cohesive law for the user-defined interface element is developed for this purpose. Since the parameter identification is based on optimization techniques, much time is spent on formulating a proper objective function. Initially, the objective function is based on global structural response, but use of local measurements in the fracture process zone is also investigated.

The motivation for this method is to reduce usual assumptions involved in characterization of cohesive zone parameters, increase the practical applicability by not limiting the approach to coupon testing, and gain as much information from few but costly experiments.

Resumé

Dette kandidatspeciale omhandler parameter identifikation af kohæsive zone love til numerisk modellering af delaminering i komposit materialer. Parameter identifikation udføres gennem brug af invers modellering og optimeringsteknikker. Invers modellering er matematisk set den inverse proces af at bestemme afhængige variable på baggrund af uafhængige variable, eller alternativt formuleret, er det processen af at bestemme input parametre som funktion af output parametre. I henhold til dette speciale er de omtalte input parametre kohæsive zone parametre og output parametre er et strukturelt respons som måles i både et fysisk eksperiment og den numeriske finite element model. En mindste kvadraters formulering af et residual, som udtrykker forskelle i det eksperimentelle og numeriske respons, minimeres ved hjælp af gradient-baseret optimeringsalgoritmer gennem MATLAB.

Det kommercielle finite element program ANSYS (MAPDL v. 17.2) anvendes til at modellere delaminering. Mere specifikt, anvendes en brugerdefineret interface elementrutine, UserElem, til at modellere selve revnevæksten. En multilinear kohæsiv zone lov, bestående af et arbitrært nummer af linje segmenter, udvikles til dette formål. Loven er af generel karakter og kan anvendes for en hvilken som helst grad af revneåbningsforhold.

En kort gennemgang af rapportens indhold følger. Indledningsvist er et historisk overblik givet af emnet kohæsiv zone modellering og dets anvendelse i forbindelse med finite element metoden. Efterfølgende præsenteres randværdiproblemet, som indeholder en stærk diskontinuitet, og de styrende ligninger for systemet, som er iboende ulineære som følge af den ulineære materiale lov i den kohæsive model, og generelt også geometrisk ulineært.

Konstitutive betingelser for det kohæsive interface element er udledt fra en skadesmekanisk betragtning, med indirekte anvendelse af klassisk brudmekanik. Herunder opstilles en skadesmodel, en konstitutive tangent stivhedstensor og en relation mellem revneflade forskydning og traktion. Skadesmodellen indeholder kriterier for skadesinitiering og revne udbredelse, samt interpolationsfunktioner til behandling af blandet revneåbningsforhold. De konstitutive betingelser er implementeret i UserElem, som indeholder de resterende nødvendigheder for en komplet beskrivelse af elementet, udarbejdet tidligere på Institut for Materialer og Produktion Aalborg Universitet.

Kohæsive zone parametre identificeres ved at sammenholde et respons fra den numeriske model og det fysiske eksperiment ved minimering af et residual. Optimeringsværktøjer gennem MATLAB er anvendt til minimering af residualen. Valget af algoritme er træffet på baggrund af en kort teoretisk redegørelse samt indledende tests. Afgørende for valget er grad af ikke-linearitet og konveksitet, skalering af design variable, samt mulighed for indførelse af uligheds-betingelser. En 2. ordens gradient baseret algoritme er anvendt i kombination med en multilinear kohæsiv zone lov bestående af 15-linje segmenter til at bestemme parametre herfor, til modellering af delaminering i et DCB testemne under ren type I revneåbning. Efterfulgt resultatbehandlingen, udføres en sensitivitets analyse og indflydelsen af 3D effekter undersøges nærmere.

Preface

This master thesis includes the findings of the group 1.121-B during the 4th semester of the master program “Design of Mechanical Systems” hold at Aalborg University. The project period started the 1st of February 2017 and concluded the 2nd of June 2017. In this thesis, the results of the numerical simulations and the novel optimization program IPIT-CZL have been obtained using a cluster owned by the Mechanical and Production Department. The cluster have 2 processors Intel Xeon CPU E5-2687W v4 3.00 GHz (24 cores) and 256 GB RAM, although 6 to 8 cores have been used normally.

The content of the compressed folder submitted together with this document is arranged in the following manner:

- IPIT-Bilinear\
 - ~ \Program\: Includes the MATLAB scripts and ANSYS macros files required to execute IPIT-CZL for the problem considered in Sec. 4.2.
 - ~ \SettingUp\: Includes the results and plotting tools that have been utilized to set up the optimization tool, Sec. 4.2.3 - 4.2.6.
- IPIT-Multilinear\
 - ~ \PlottingTools\: Includes the MATLAB scripts in charge of plot results.
 - ~ \Program\: Includes the MATLAB scripts and ANSYS macros files required to execute IPIT-CZL for the problem considered in Sec. 5.3.
 - ~ \Results\: Includes all the results presented in Sec. 5.4.
 - ~ \SensitivityStudy\: Includes the results from the sensitivity studies in Sec. 6.1.
- 1121B_DMS4_Spring2017.pdf: A digital version of the present document in pdf format.

The authors acknowledge the supervisors of this work Associate Professor, Ph.D. Esben Lingaard and Assistant Professor, Ph.D. Brian Bak for all the suggestions, guidance and facilities provided. Last but not least, a special thanks go to our families for all the support and love received.

Table of contents

1	Introduction	3
1.1	Motivation	3
1.2	Historical Review / State of the Art	5
1.3	Problem Specification	7
2	Cohesive Zone Modelling	11
2.1	Governing System of Equation	11
2.2	Constitutive Relation	21
2.3	Damage Mechanics Model	22
2.4	Mode Mixity Interaction	28
2.5	Cont'd Constitutive Tangent Stiffness Tensor	38
3	Interface Element Formulation	41
3.1	Interface Element Formulation	41
3.2	Programming of Interface Element Constitutive Relation	44
3.3	Verifying Implementation	51
4	Inverse Parameter Identification Tool for CZ Laws	55
4.1	Introduction	55
4.2	Optimization	57
4.3	IPIT-CZL Subroutines	66
5	Assessment of Delamination	71
5.1	Experimental Setup	71
5.2	Finite Element Model	74
5.3	Design Problem Formulation for Multilinear CZ Law	77
5.4	Assessment of Delamination with IPIT-CZL	81
5.5	Progression of IPIT-CZL Optimizer	90
6	Sensitivity Studies and 3D Effects	95
6.1	Sensitivity Studies of IPIT-CZL	95
6.2	3D Effects	100
7	Conclusion	105
8	Further Work	107
	Bibliography	111

List of figures

1.1	(a) Fuselage section of a Boeing 787 Dreamliner, showing formers, stringers, and skin all made of composite material [Boffoli, 2007]. (b) Sectioned wind turbine blade, showing skin, flanges and web. (c) Flange tip delamination of a thick-flanged stiffener test specimen [Haugen, 1998]. (d) Web and flange-skin delamination of thin-flanged stiffener test specimen [Haugen, 1998].	4
2.1	Boundary value problem for crack propagation problem.	11
2.2	Body V is split into two by a discontinuous singular interior surface S	13
2.3	A simple planar representation of surfaces \bar{S} , S^+ , S^- and their outward unit normal vectors.	14
2.4	A cut-out of the crack path surface Γ^d in deformed and undeformed configuration.	17
2.5	(a) Separation vector $\vec{\delta}$ and its components for use in damage models. 3D description includes the whole light grey box, while the 2D description is confined to the blue plane. (b) Local coordinate system at interfacial midsurface \bar{S}	23
2.6	Concept of work conjugate traction norm, the figure is based on [Hansen and Lund, 2009]	26
2.7	(a) An illustration of the integration path for the J-integral for a plane problem and a cohesive zone. (b) Concept of self-similar crack growth. δ^* represents the separation at the end opening, while δ' represents the separation at a point inside the cohesive zone.	29
2.8	(a) Symbolic n-segmented mixed mode multilinear CZ law in $(\bar{\sigma}; \bar{\delta})$ -space. (b) Multilinear CZ laws and interpolation between pure mode material data.	33
2.9	(a) A one-dimensional equivalent CZ law for a given mode mixity. (b) Line segment containing three points in separation-traction space.	35
2.10	Illustration of the situation dependence of the tangent stiffness tensor. Here the tangent stiffness tensor is shown in mode I space, that is the third traction and separation components are considered.	39
3.1	8-noded, brick, isoparametric interface solid element.	41
3.2	(a) n-degree multi linear cohesive law. (b) Illustrate concept of d_i^{lim} parameter. (c) Arbitrary line segment of multi linear law for a given separation range. (d) The fracture energy left for a given separation.	45
3.3	(a) FE model for verification test. (b) Pure mode I loading - reloading sequence.	51
3.4	(a) Works well. (b) Works well. (c) Problem: Restoration of cohesive state. (d) Ideal loading/unloading of CZ law in fig. (c).	52
3.5	Verification example for 3 mode mixity ratios β	53
4.1	IPIT-CZL flowchart	56

4.2	(a) End-loaded DCB specimen (b) Bilinear constitutive law.	57
4.3	FE model of the end-loaded DCB specimen, σ_y is shown.	58
4.4	Sensitivity study to find an appropriate perturbation size for (a) $x_1 = G_{Ic}$ and (b) $x_2 = \sigma_3^{(1)}$	63
4.5	(a) Contour plot and (b) Surface plot of the design space. (c) Contour plot (optimum displayed as a green dot) and (d) Surface plot of the convex area.	64
5.1	(a) Illustration of DCB specimen under pure moment loading (b) Real experimental set up of the DCB specimen and moment arms (c) Pulley system and connection to Zwick tensile testing machine (d) A single moment arm, its orientation and the resulting force couple.	72
5.2	(a) Moment arms grips. (b) Clip gauge mounted in the test set up.	73
5.3	Global structural responses: (a) Applied moment versus end opening separation δ^* (b) Applied moment versus angle of rotation	73
5.4	Geometric differences between the experiment and the numerical simulations, due to the moment introduction in the specimen.	75
5.5	DCB model under pure bending, nodal solution, σ_y , corresponding to the last substep ($\varphi = 16.3^\circ$). The end at the left hand side is fixed.	76
5.6	Multilinear CZ law for pure mode I crack opening	78
5.7	Zoom in: End opening separation versus moment per width for test specimen 0deg - 5.	80
5.8	CZ laws of the reference set and all the initial guesses IG1-4. Left: NCT region. Right: FB region.	81
5.9	Global structural responses of the reference CZ law and all the initial guesses.	82
5.10	Evolution of the global structural response for the execution IG3. (a) Initial guess (b) through (g) 1'st to 6'th iteration (h) converged solution.	83
5.11	Evolution of the global structural response for the execution IG3. (a) Initial guess (b) through (g) 1'st to 6'th iteration (h) converged solution.	85
5.12	Converged CZ laws of (a) IG1 through IG4 (b) restarted IG1 through IG4.	87
5.13	Converged global structural responses of (a) IG1 through IG4 (b) restarted IG1 through IG4.	88
5.14	Comparison of numerical and experimental global structural responses for all solutions: (a) Applied moment versus angle of rotation (b) Applied moment versus end opening separation.	90
5.15	History data for initial guess 3.	91
6.1	Comparison of CZ laws obtained for the different sensitivity studies with the original result.	97
6.2	Converged solution for the sensitivity studies (A) and (B). Comparison of numerical and experimental global structural responses : (a) Applied moment versus angle of rotation (b) Applied moment versus end opening separation.	98
6.3	Global structural responses for test specimen 0deg - 3 and 0deg - 5 (a) Applied moment versus angle of rotation (b) Applied moment versus end opening separation.	99
6.4	Converged solution using the data set 0deg - 3. Comparison of numerical and experimental global structural responses : (a) Applied moment versus angle of rotation (b) Applied moment versus end opening separation.	99
6.5	Comparison of CZ laws obtained for the data set 0deg - 5 (Original) and 0deg - 3 (Sensitivity Study (C))	99
6.6	Poisson effect leading to anticlastic deformation of the cross section.	100

6.7	(a) DCB specimen loaded by pure moments in pure mode I crack opening (b) Cutaway of a section in the process zone where the separation δ_3 at the edge is larger than 0.	100
6.8	Isosurface contour plots at angle of rotation $\varphi^* = 11.41^\circ$, σ_y is displayed (a) Full width $\nu_{xz} = 0$ model (b) Full width model.	101
6.9	IPIT-CZL solutions: Comparison of CZ laws obtained of the full width, the full width-zero Poisson's ratio ν_{xz} and the unit width model	101
6.10	IPIT-CZL solutions: Comparison of numerical global structural responses of the full width, the full width-zero Poisson ratio ν_{xz} and the unit width model: (a) Applied moment versus angle of rotation (b) Applied moment versus end opening separation.	102
6.11	Anticlastic effect: Comparison of numerical global structural responses of the full width, the full width-zero Poisson ratio ν_{xz} and the unit width model for the same CZ law named CIG4R: (a) Applied moment versus angle of rotation (b) Applied moment versus end opening separation.	103

List of tables

3.1	Relations between UserElem outputs and APDL commands.	52
3.2	Prescribed displacements for three tests of different mode mixity ratio.	53
4.1	Sensitivity study to find an appropriate perturbation size for $x_1 = G_{Ic}$ and $x_2 = \sigma_3^{(1)}$	62
4.2	Benchmark test results for different optimization algorithms.	65
5.1	Geometric and material properties for the test series.	71
5.2	Material properties used in the FE model presented in this section.	74
5.3	Parameters and DV for 15'th order multilinear CZ law	78
5.4	The four initial guesses used.	82
5.5	Results obtained from IPIT-CZL for the selected experiment with four initial guesses. Part I	86
5.6	Results obtained from IPIT-CZL for the selected experiment with four initial guesses. Part II	86
6.1	Various distributions of fixed separation points $\delta_3^{(i)}$ for a pure mode I CZ law. Changes compared to the original distribution are marked in bold text	96
6.2	Tractions $\sigma_3^{(i)}$ of the converged CZ law for each sensitivity study. The separations can be seen in the previous table.	97

Nomenclature

Note that the units have been applied consistently during the whole report. Dimensions [mm], mass [t]¹ and time [s], leading to force [N], pressure [MPa], fracture resistance-energy release rate [kJ/m^2] and so on. The specific parameters and their units are given below.

Greek Letters

Symbol	Units	Description
β	[-]	Mode mixity ratio
ε_{ij}	[-]	Strain tensor
δ_{ij}	[-]	Kronecker's delta
$\vec{\Delta}, \vec{\delta}$	[mm]	Local displacement jump vector
$\Delta^{(1)}, \delta^{(1)}$	[mm]	Onset of damage separation
$\Delta^{(n)}, \delta^{(n)}$	[mm]	Final separation, fully damaged
λ	[mm]	Equivalent displacement jump norm
ρ	[-]	Mode mixity ratio
σ_{ij}	[MPa]	Stress tensor
$\vec{\tau}, \vec{\sigma}$	[MPa]	Interfacial traction vector
$\bar{\sigma}$	[MPa]	Equivalent interfacial traction vector norm
$\tau^{(1)}, \sigma^{(1)}$	[MPa]	Onset of damage traction

Roman Letters

Symbol	Units	Description
a	[mm]	Crack length
b	[mm]	Specimen width
d	[-]	Damage parameter $d \in [0; 1]$
D_{ij}^0	[MPa]	Undamaged stiffness tensor
D_{ij}^{tan}	[MPa]	Constitutive tangent stiffness tensor
E	[MPa]	Young's modulus
G	[kJ/m ²]	Energy release rate
G_c	[kJ/m ²]	Critical energy release rate
I, II, III	[-]	Refers to crack mode 1, 2 and 3
$[I]$	[-]	Identity matrix
J	[kJ/m ²]	Fracture resistance
K	[MPa]	Penalty stiffness
L	[mm]	Length
M	[Nmm]	Moment
P	[N]	Force
q	[mm]	Vector containing nodal displacements
r	[mm]	Damage threshold value
t	[s]	Time or pseudo solution time
W	[kJ/m ²]	Work of interfacial separations per unit area

Additional Symbols

Symbol	Units	Description
--------	-------	-------------

¹Metric ton.

\dot{a}	[–]	Time derivative
$\langle a \rangle$	[–]	MacAuley bracket
$\{a\}$	[–]	Vector notation
$[a]$	[–]	Matrix notation
$\lceil a \rceil$	[–]	Diagonal matrix

Introduction

1.1 Motivation

A powerful quality of composite structures is their ability to have tailored material properties for a specific application. In the wake of the introduction of composite materials during the mid-twentieth century, came an unprecedented and separate class of failure mechanisms, such as delamination, matrix failure/yielding, fiber-matrix debonding, kink band failure, fiber micro-buckling, fiber failure, which can be either brittle- or brushing-like depending on the strength of the adhesive. The diversity of failure mechanisms are mainly attributed to the inherently heterogeneous microstructure of composites, their anisotropy, and often laminated applications. In real-life engineering structures using multidirectional composites, the most common failure mechanism is delamination, due to the relatively weak interface strength of a laminate [Overgaard and Lund, 2014].

Due to limitations in knowledge of these failure mechanisms, is the full potential of composite materials and their applicability for general engineering structures not yet fully exploited. This motivates the scope of this master thesis, which seeks to develop a tool for characterization of fracture related material properties for numerical modelling of delamination.

Delamination can be caused by numerous reasons, e.g. manufacturing problems such as resin-rich areas or areas of high degree of porosity which is potential sites of failure initiation and subsequent delamination growth. Further examples include delamination caused by high peel stresses or stress concentrations, which naturally occurs at many common types of structural details e.g. free edges of a laminate, ply-drops/-inserts and various structural joints.

The importance of proper assessment of delamination in practice is illustrated by considering a specific type of structural joint: A skin-stiffener joint, which is a connection of a (composite) skin to a stiffer member, e.g. a former, a stringer, a longeron or a bulkhead, to provide load transfer paths and structural integrity. Skin-stiffener joints are commonly encountered in aerospace and wind turbine industries.

Skin-stiffener structures are nearly used in all aircraft fuselage constructions. An example of a sectioned fuselage of a Boeing 787 Dreamliner is shown in Fig. 1.1a. A primary concern and common problem in thin-walled stiffened aircraft fuselages is delamination caused by pressure pillowing [Haugen, 1998]. During a flight, the cabin pressure in a commercial transport aircraft generates an internal pressure that is higher than the surrounding pressure outside the fuselage. The frames and stringers, as shown in Fig. 1.1a, prevent the fuselage skin from expanding as a membrane. Consequently the fuselage skin bulges outwards, or *pillows*, within each panel under the action of the internal pressure. The restraint against radial expansion

at the stiffener locations causes the formation of a bending boundary layer¹, which results in stress concentrations. As a result, peeling stresses and transverse shear stresses develops at the interface between the skin and stiffener which can lead to delamination [Haugen, 1998].

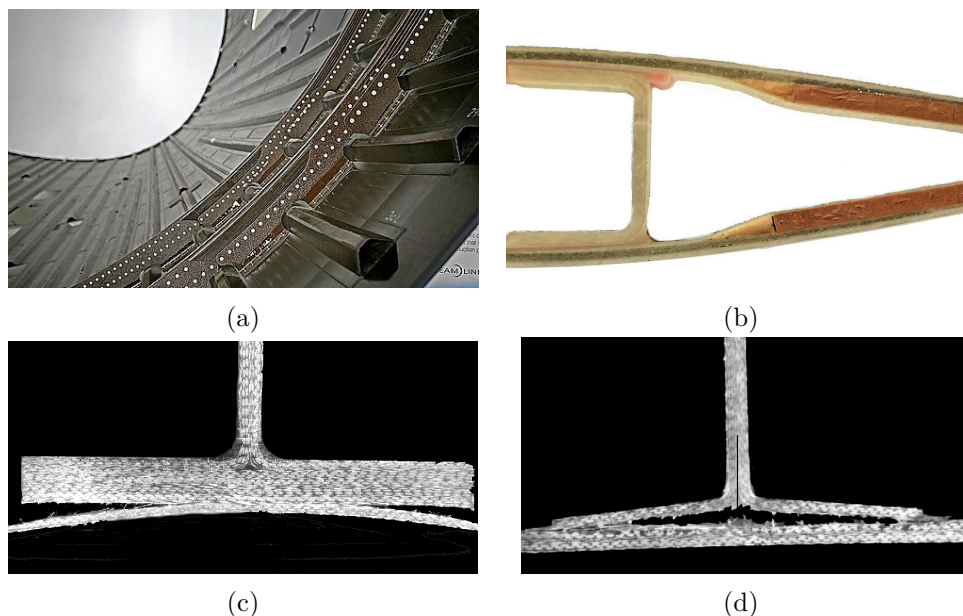


Figure 1.1: (a) Fuselage section of a Boeing 787 Dreamliner, showing formers, stringers, and skin all made of composite material [Boffoli, 2007]. (b) Sectioned wind turbine blade, showing skin, flanges and web. (c) Flange tip delamination of a thick-flanged stiffener test specimen [Haugen, 1998]. (d) Web and flange-skin delamination of thin-flanged stiffener test specimen [Haugen, 1998].

Another example of delamination in skin-stiffener joints in engineering structures is seen in Fig. 1.1b, showing a cross section of a wind turbine blade. The interfaces between the web, flange and skin in a wind turbine blade are often sites of fracture initiation and delamination growth. Potential sources of delamination initiation for such skin-stiffener T-joints include geometric discontinuities e.g. the geometric transition from the flange to the skin, the abrupt change in bending stiffness of the skin and the flange which can form a bending boundary layer, differences in ply-angles of adjacent plies in regions of a bending boundary layer, and manufacturing issues related to resin flow [Haugen, 1998].

Experimental testing on skin-stiffener T-joints, similar to those in common wind turbine blades, are performed by [Haugen, 1998] as shown in Fig. 1.1c and 1.1d. The figures show two details of different geometry; one having a thick flange and one having a thin flange. The skin is simply supported and a tensile load is applied to the web until complete pull off. In Fig. 1.1c failure initiates at the flange tips and delamination grows towards the center along the flange-skin interface. In Fig. 1.1d, failure initiates at the web-flange and fillet region, and delamination progresses towards the flange tips and along the web-centerline. Further information about material system, manufacturing, etc. are omitted, since the purpose is solely to illustrate delamination in practice.

The above discussion concerning delamination in general engineering structures and the severity of consequences of failure, motivates for a methodology for assessment of delamination suitable of analysing damage tolerant designs.

¹Bending boundary layer refers to localized zones of bending stresses and deformations.

1.2 Historical Review / State of the Art

In 1921, [Griffith, 1921] presented an energy criterion for crack propagation, which postulate that cracks propagate when the related energy release rate reaches its threshold value. Then, Linear Elastic Fracture Mechanics (LEFM) was used by [Irwin, 1957] to reformulate the crack propagation criterion using stress intensity factors. His work was continued by other researchers leading to a technique called Virtual Crack Closure (VCC) [Goyal, 2003, p.14]. VCC, the J-integral presented by [Rice, 1968] and the virtual crack extension by [Hellen, 1975] represent the most used direct applications of LEFM in crack propagation problems [Alfano and Crisfield, 2001]. The use of LEFM to predict the delamination growth has been proven accurate however its applicability is limited [Alfano and Crisfield, 2001] [Turon et al., 2006]:

- LEFM can be used in lack of other material non-linearities [Alfano and Crisfield, 2001] [Turon et al., 2006].
- LEFM only consider crack propagation, therefore it requires the existence of a crack of known initial extension and location [Alfano and Crisfield, 2001] [Turon et al., 2006] growing in a self-similar manner (a priori known trajectory) [Goyal, 2003, p.15].
- LEFM assumes the existence of infinite stresses in the crack tip.
- LEFM assumes that the crack tip is confined to a small region, thus it cannot represent the increase of fracture resistance due to fiber bridging over large process zones, which is referred to as R-curve behavior. During delamination of fiber-reinforced materials is commonly seen a prominent R-curve behavior due to large scale bridging.
- LEFM techniques in a Finite Element (FE) context are computationally inefficient due to how fracture parameters such as stress intensity factors or energy release rates are calculated [Turon et al., 2006]. Thus, it can be used for 2D stationary crack propagation, although for 2D progressive crack propagation the computational effort rises dramatically [Turon et al., 2006]. Moreover, computational issues emerge when dealing with the progression of multiple cracks in a 3D problem [Alfano and Crisfield, 2001] [Goyal, 2003, p.15].

Nonetheless, the cohesive zone modelling (CZM) represents an alternative approach to LEFM that overcome all the issues mentioned above. CZM simulates the behavior of the crack interface using the framework of damage mechanics in conjunction with indirect application of LEFM [Alfano and Crisfield, 2001]. The fundamental idea of CZM is that resistance to crack propagation can be described by a traction field acting on separated crack surfaces in the cohesive zone (CZ), a region that commences at the crack tip and spans in the wake of the crack. The traction field can be regard as a continuous distribution of nonlinear springs, independent of one another, holding the crack surfaces together. The CZ is defined by a CZ law, a constitutive relation between crack surface tractions and separations, which can be seen as the stiffness of the nonlinear springs. In addition, CZM incorporates the initiation of cracks using strength criterion. This allows one to model delamination growth in specimens where the crack location, size and trajectory do not have to be known beforehand. It is noted that CZM yields to the same results obtained by LEFM, when LEFM can be applied.

In regard to numerical models for delamination in FE analysis (FEA), the CZM is used in combination with interface elements, which can be placed between adjacent layers of the laminate. In short, delamination starts when the interlaminar traction surpass the interfacial strength, and the crack front progresses when the fracture toughness of the element surpass its critical value.

The fact that CZM unifies crack initiation and propagation in a single theory and its simple implementation in FEA makes it a very convenient tool to model delamination problems.

In relation to the origin of the CZM, it dates back to the late 50s and early 60s when Barenblatt [Barenblatt, 1959] and Dugdale [Dugdale, 1960] developed two independent models that overcome the singular stresses at the crack tip by application of a traction field around it, holding the crack faces together. Barenblatt proposed an equilibrium problem for elastic materials with brittle cracks including cohesive forces at the tip and in the wake of the crack. Dugdale argued that the stresses cannot increase beyond the yield strength of the material and proposed, for ductile materials, the existence of a traction field ahead of the crack tip, where nearby a plastic zone develops. Thereafter, Hillerborg presented in [Hillerborg et al., 1976] a similar model to Barenblatt's, including crack initiation and analyzed the CZ using FE methods (FEM). Needleman in [Needleman, 1987] used CZM to simulate the whole interface in a 2D FEA. During the 90s and until mid-2000s different CZ laws have been proposed and implemented in FE, some have trapezoidal shape as in [Tvergaard and Hutchinson, 1992], others exponential shape as in [Goyal-Singhal et al., 2004], and others bilinear shape as in [Alfano and Crisfield, 2001] or [Camanho et al., 2003]. These element formulations, besides [Goyal-Singhal et al., 2004], require that the mode mixity ratio is kept constant during delamination growth, otherwise dissipated energy could be restored due to how the threshold value have been defined. [Turon et al., 2006] presented a new formulation for interface elements using a bilinear CZ law addressing this issue.

More recently, [Bak et al., 2014] elaborated an interface element implementation based on [Turon et al., 2006], where the error stemming from the integration of the stiffness matrix and the element force vector is reduced by adaptively changing the quadrature order and integration rule (from Newton-Cotes to Gauss-Legendre) depending on the state of element damage. That brought an improvement of the overall convergence of the element and allowed the use of a more coarse mesh.

The present master thesis brings further development on the aforementioned implementation. A new constitutive relation is introduced extending the cohesive law from bilinear to multilinear, with any number of line segments. The delamination initiation criterion is the same as the one described in [Turon et al., 2006]. A novel propagation criterion for mixed mode crack opening is presented for a multilinear CZ law, where the mode mixity interpolations are chosen such that the resulting CZ law is energy consistent with the BK criterion. It is worth mentioning that the calculation of a mode mixity ratio at every interface element integration point is calculated using results from [Hansen and Lund, 2009], which dealt with a mixed mode trilinear CZ law.

In addition, the present master thesis introduces a methodology for characterization of material properties of quasi-static delamination in fiber-reinforced materials showing R-curve behaviour. The material properties are the CZ parameters for a n-segmented multilinear CZ law. An approach to determine CZ laws based on curve fitting and derivatives of the analytical J-integral for two dimensional (2D) plane problems is proposed in [Sørensen and Kirkegaard, 2006]. The approach presented here is not limited to 2D plane problems, as the previous approach, since it utilizes a FE model being able to account for 3D effects. The parameter identification is done using optimization techniques to minimize a response from a physical experiment and a parametric FE model. A more detailed explanation of the work contained in this master thesis is presented in the next section.

1.3 Problem Specification

The scope of this master thesis is to develop and test a methodology for characterization of material properties for numerical modelling of quasi-static delamination in composite materials. The methodology relies on finite element modelling and cohesive zone modelling, giving the opportunity to model both delamination onset and propagation. Consequently, the material properties to be determined are cohesive zone parameters. A physical experiment is conducted and simulated in a parametric finite element model. The cohesive zone parameters are then determined through use of inverse parameter identification in conjunction with optimization techniques by minimization of a difference in some measured response from the experiment and the numerical model.

The master thesis is a continuation of work done in a previous semester. An outline is given here to clarify what was done on the previous semester (3rd semester of the master program), and what is done in this semester (4th).

The point of departure is a user-defined element subroutine, `UserElem.f`, which is used in conjunction with the commercial finite element program ANSYS MAPDL v. 17.2, and has been available to the authors of this master thesis since the beginning of the 3rd semester. The `UserElem.f` element routine defines a cohesive zone interface element, which in essence, includes a kinematic description, constitutive relations, a damage mechanics model, numerical integration schemes, formulation of an element stiffness matrix and internal force vector, and subroutines for post processing, which is all developed by researchers at Department of Mechanical and Manufacturing Engineering at Aalborg University. In this project the primary objective of interest is the damage mechanics model, wherein the mixed mode cohesive zone law is formulated and partially the element stiffness matrix computation. The user-defined element subroutine originally included a mixed mode bilinear cohesive zone law.

1.3.1 3rd Semester

An outline of the work done on the 3rd semester project is given here. Further information is found in [Jensen and Martos, 2016]. The aim of the report is to be able to simulate a delamination process in a finite element model such that structural responses agree with results obtained from a physical experiment. The experiments are done using double cantilever beam (DCB) specimens loaded under pure bending and pure mode I crack opening. The material system under consideration is unidirectional glass fibre epoxy composites. Experiments have been carried out, however, due to inconsistencies in the experimental data, lack of time, and the computational convenience of using smaller test specimens than those originally given, the final experimental data is given by the supervisors. During delamination an R-curve behaviour is experienced due to fibre-bridging in the wake of the crack tip. The fibre-bridging complicates the fracture process zone, as failure mechanisms will occur at multiple length scales.

The simulation of delamination is done through use of cohesive zone modelling. The bilinear mixed mode cohesive zone law implemented in `UserElem.f` is not capable of simulating R-curve behaviour, since only failure mechanisms occurring in the crack tip region is captured by a bilinear cohesive zone law. By adding an extra line segment to the cohesive zone law, the model becomes capable of simulating multiple failure mechanisms on different length scales. Consequently, an extension of the bilinear cohesive zone law to a trilinear cohesive zone law is a necessity to be able to simulate the physical experiment due to the R-curve behaviour associated with the fibre-bridging.

The extension to a trilinear cohesive zone law is limited to pure mode I crack opening. Consequently, mixed mode interaction are not considered in the report. The implementation in the user-element subroutine is tested and verified.

Having formulated a cohesive zone model capable of simulating the failure mechanisms involved in the physical experiment, proper cohesive zone parameters need to be identified. This is done by inverse parameter identification, which in general is the process of determining inputs on the basis of outputs. In this sense, inputs are cohesive zone parameters for the finite element model and outputs are structural responses. Key to the identification process is utilization of optimization techniques.

A structural response is measured in the physical experiment and in the finite element model for some set of cohesive zone parameters. Their difference should be minimized by changing the cohesive zone parameters, which forms the basis of the objective function for the optimization procedure: A residual between numerically simulated and experimentally measured structural responses. In context of optimization theory, the cohesive zone parameters become the design variables. Ideally the residual is zero once the cohesive zone parameters have been identified.

A program is developed for the parameter identification, which is denoted IPIT-CZL, being short for Inverse Parameter Identification Tool for Cohesive Zone Laws. The program is made in MATLAB. Its major tasks is to control the optimization scheme for the minimization of the residual, generate and execute the finite element model for a given set of design variables, and extract and compare structural responses from the numerical model and the physical experiment. In this semester, the framework of IPIT-CZL is developed, which implies formulating the overall structure of IPIT-CZL on paper, implement it in MATLAB and make it work as intended. Naturally, as a first draft, there are room for improvements and further development. Additionally, some decisions are made with little theoretical reference due to time limitations.

Initial testing and benchmark tests have been run to make IPIT-CZL work as intended. Eventually, IPIT-CZL is tested for identifying cohesive zone parameters for use in a pure mode I trilinear cohesive zone law, to simulate a physical experiment showing R-curve behaviour. IPIT-CZL fails to obtain consistent cohesive zone parameters for different initial guesses. A lot of local minima are discovered and the best of the converged solutions does not represent the experimental structural response well. Nevertheless, the framework of IPIT-CZL has been developed and tested, and improvements are suggested for the 4th semester.

Lastly, it is noted that alternative approaches to obtain cohesive zone parameters from structural responses of a physical experiment are also investigated. An approach inspired by [Sørensen and Kirkegaard, 2006] and [Hansen et al., 2009] is used as standard of reference for IPIT-CZL. The alternative approach does not make use of finite element modelling in the parameter identification process, but relies on analytical J-integral calculations. Some parts of the 3rd semester project has been omitted in this review, since only essential things are pointed out to keep the overview rather compact.

1.3.2 4th Semester

The scope of this semester (4th) is to further develop IPIT-CZL to be able to accurately simulate delamination showing R-curve behaviour, and extend the cohesive zone model to any n-segmented multilinear cohesive zone law and generalize it to be capable of modelling delamination under mixed mode crack opening. The progress towards these aims are discussed in greater detail here.

The motivation for extending a bilinear cohesive zone law is clear from the previous semester: It gives the opportunity to model failure mechanisms on different length scales enabling the cohesive zone model to simulate R-curve behaviour. The addition of a single line segment, making the cohesive zone law a trilinear formulation, is the simplest way of introducing such effects. During the testing of IPIT-CZL using a trilinear cohesive zone law on the 3rd semester, it is however observed, that the trilinear law is not sufficient to model the R-curve behaviour seen in the physical experiment. The shape of the trilinear cohesive zone law is simply too restrictive, and is characterized by non-physical kinks in the structural response of the finite element model, that are not seen in the experimental structural response.

This motivates to introduce more line segments in the cohesive zone law formulation, making the shape less restrictive. For this purpose, the cohesive zone law is extended to handle an arbitrary number of line segments. Additionally, the cohesive zone law is generalized to be capable of modelling mixed mode crack opening, which calls for a novel formulation of mode mixity interactions for a multilinear cohesive zone law, which to the authors knowledge, has not been addressed by others. For some degree of mixed mode crack opening, interpolation functions are proposed to determine properties of a one-dimensional equivalent cohesive zone law. Verification tests have been run to validate the implementation of a mixed mode multilinear cohesive zone model.

The parameter identification methodology IPIT-CZL is tested for a pure bending loaded DCB specimen under pure mode I crack opening, similar to the one tested in the 3rd semester. The experiment is simulated using a 15 line-segmented multilinear cohesive zone law in the finite element model. This involves a relatively large number of cohesive zone parameters to be identified, however, the shape of the cohesive zone law is less restrictive.

To the authors knowledge, the common approach for simulating delamination is based on presuming the shape of the cohesive zone law to be e.g. bilinear, trilinear, trapezoidal, exponential etc. based on physical reasoning, and then determine cohesive zone parameters for that specific shape based on either material data obtained from coupon tests, or some structural response related to cohesive zone parameters, e.g. analytical J-integral relations. Here, the typical classification of cohesive zone law shapes is discarded, and the idea of determining the cohesive zone law shapes is based on discretization of the cohesive zone law into a relatively large number of piecewise linear functions, and then let the shape be determined directly by minimization of the residual in structural responses.

Experience from the previous semester regarding the performance of the optimizer in IPIT-CZL, suggests reformulating the optimization problem and investigate other options for algorithm selection. The objective function is defined as a least squares residual formulation of the structural responses in the experiment and the numerical model. The algorithm selection is limited to those available through MATLAB for minimization of constrained nonlinear optimization problems. A gradient-based interior-point algorithm is concluded to be best suited for the problem at hand through theoretical considerations and benchmark testing. The algorithm is capable of switching between second order quasi-newton methods in combination with a line search method for the step computation, and a trust-region method with

first order conjugate gradient steps depending on Hessian properties at the current design iterate.

The performance of the reformulated optimization problem is significantly improved compared to the previous semester. IPIT-CZL converges to optimum points of consistent cohesive zone parameters and objective function values, and a good agreement in terms of numerical and experimental structural responses. Further comments are left for the report.

At the very end, sensitivity studies of the IPIT-CZL are performed to anticipate robustness of the methodology. Additionally, the topic of 3D effects is considered which is a general challenge in state of the art methods for assessment of delamination.

Problem Formulation

The above discussion regarding the content of the master thesis should be covered by the following problem formulation. The scope of the master thesis is formulated in compact form as: Development and optimization of a methodology for inverse parameter identification of multilinear mixed mode cohesive zone laws through parametric finite element modelling and optimization for numerical assessment of quasi-static delamination in composite materials.

Cohesive Zone Modelling

2.1 Governing System of Equation

The governing system of equations to be solved are presented in the current section. The boundary value problem is presented in strong form, and eventually transformed into a weak formulation, by using the principle of virtual work. However, the principle of virtual of work in its original only applies for a continuous system. In order to apply the principle for a crack propagation problem, which is inherently discontinuous, the original body is divided into subdomains and extra boundary conditions are introduced. Ultimately, the governing system of equations are derived, and the need for solving it numerically is argued. The FEM will be used for numerical evaluation and hence the governing equations are arranged in a form suitable for the FEM. The derivation of the governing equation presented in this section is based on [Goyal, 2003], [Malvern, 1969] and [Turon et al., 2006].

2.1.1 Boundary Value Problem

In order to discuss the mechanics of interfacial surfaces, it is appropriate to take departure from the boundary value problem at hand. A crack propagation problem is inherently a discontinuous system, containing discontinuous singular surfaces. A surface is said to be singular, if one or more properties are discontinuous across that surface. The singular surfaces of crack propagation problems are categorized as strong discontinuous, since the displacement field jumps across the surface.

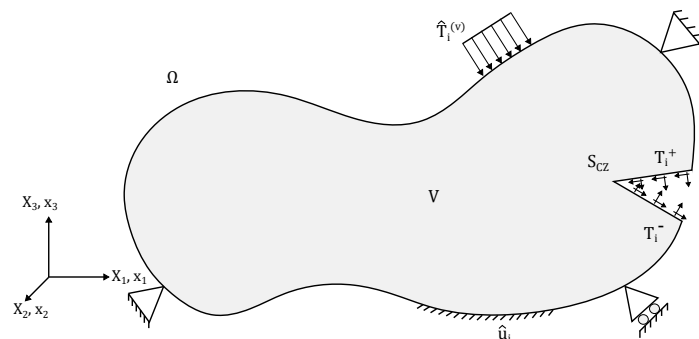


Figure 2.1: Boundary value problem for crack propagation problem.

Consider a solid deformable body V as shown in Fig. 2.1 containing a crack. The part of the crack on which a cohesive zone law is active is denoted by S_{cz} and is called the fracture process zone.

The body V is enclosed by an external surface Ω , which has an outward unit normal vector, denoted v_j . Let B_i and $\hat{T}_i^{(v)}$ represent body forces and prescribed surface tractions in the deformed state respectively. The surface Ω^T denotes the outer boundary on which tractions are prescribed, such that $\sigma_{ij}v_j = \hat{T}_i^{(v)}$ in accordance with Cauchy's formula. Let Ω^u denote the outer boundary on which the displacement field is prescribed as $u_i = \hat{u}_i$. The boundaries of prescribed tractions and displacements are defined such that their sum equals the total external boundary, $\Omega = \Omega^T + \Omega^u$. The stress field inside the domain V , is related to the external loading and tractions in the fracture process zone through equilibrium equations as given in Eq. (2.1.1) through Eq. (2.1.4) [Turon et al., 2006].

$$\sigma_{ij,j} + B_i = 0 \quad \text{inside } V \quad (2.1.1)$$

$$\sigma_{ij}v_j = \hat{T}_i^{(v)} \quad \text{on } \Omega^T \quad (2.1.2)$$

$$u_i = \hat{u}_i \quad \text{on } \Omega^u \quad (2.1.3)$$

$$\sigma_{ij}^+ v_j^+ = T_i^+ = -T_i^- = \sigma_{ij}^- v_j^- \quad \text{on } S_{cz} \quad (2.1.4)$$

The boundary value problem is a mixed problem, since both displacements and tractions are prescribed. The equilibrium equations in Eq. (2.1.1) are part of the strong formulation of the boundary value problem at hand, i.e. a system of partial differential equations which must be obeyed at every material point within the solid body. The governing system of equations can be categorized into equations of equilibrium, geometric equations and constitutive equations. A brief introduction to the governing system of equations are given next.

Having already introduced the equilibrium equations in Eq. (2.1.1), the geometric equations considered next. These equations establish a relation between the strain tensor ε_{ij} and the displacement field gradients $u_{i,j}$. Various strain measures are available depending on the magnitude of the deformations, and whether the reference geometry is the undeformed or deformed configuration. One example of a strain tensor definition is the Green-Lagrange strain tensor:

$$\varepsilon_{ij} = \frac{1}{2} \left(\frac{\partial u_i}{\partial X_j} + \frac{\partial u_j}{\partial X_i} + \frac{\partial u_k}{\partial X_i} \frac{\partial u_k}{\partial X_j} \right) \quad (2.1.5)$$

The Green-Lagrange strain tensor is defined in terms of the initial undeformed geometry and indicates what must occur during a given deformation. This strain tensor puts no restrictions on the magnitude of the strains by including the nonlinear product term in the round bracket of Eq. (2.1.5). The strain tensor in Eq. (2.1.5) is seen to be symmetric. By excluding the nonlinear product term, the infinitesimal strain tensor e_{ij} arises. However, for this to be valid, displacement field gradients must be well less than unity $|u_{i,j}| \ll 1$. The geometric equations also contain the equations of compatibility, to ensure a compatible displacement field during the deformation process.

Having briefly described the stress tensor arising from equilibrium considerations, and the strain tensor arising from kinematical considerations, these are next related to each other through constitutive relations. No further discussion of specific constitutive relations are given for now, since this is a major topic in the upcoming sections. Various stress tensors exists, likewise the strain tensor, depending on the magnitude of deformations and the reference configuration. It is noted, the constitutive relations depends on the stress and strain formulation chosen. The choice of a suitable stress and strain formulation is problem dependent. However, a pair of some stress- and strain tensor needs to be work consistent, meaning that the resulting internal work or strain energy density must be independent of the formulation chosen.

2.1.2 Principal of Virtual Work for Discontinuous Systems

During the presentation of the boundary value problem, it was argued that the crack propagation problem is indeed a discontinuous system. To develop the necessary mechanical relations, further notations and introduction of a predefined crack path are added to the original boundary value problem in Fig. 2.1. The crack path is denoted as S and acts as an interior discontinuous singular surface as illustrated in Fig. 2.2.

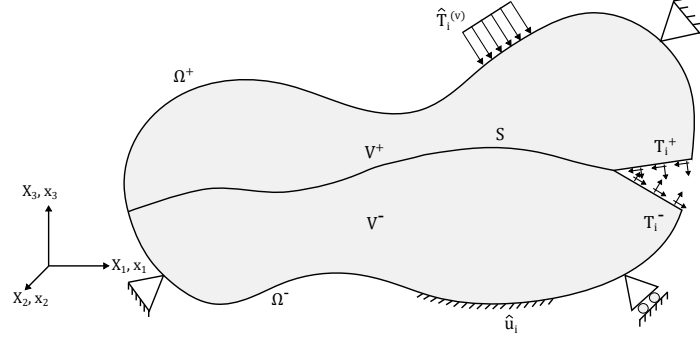


Figure 2.2: Body V is split into two by a discontinuous singular interior surface S .

The original domain V is divided into two subdomains V^+ and V^- by the interior surface S . In terms of real world applications, the body V could represent a composite laminate, and S would then represent the adhesive between two adjacent lamina V^+ and V^- . The surface S would in this case be the path of delamination.

In general the principle of virtual work does not apply to discontinuous systems, however, it can be used in its original form for each continuous subdomain, and the discontinuous system can then be represented by introduction of extra boundary conditions for the interior surface discontinuity. Therefore it is natural to review the principle of virtual work for continuous systems.

For this purpose, the solid deformable body in Fig. 2.1 is reconsidered. The whole body V is considered a continuous system and the crack at the right end of the figure is neglected. The external virtual work for such a system can be written as:

$$\delta W_{ext} = \int_V B_i \delta u_i dV + \int_{\Omega} \hat{T}_i \delta u_i d\Omega \quad (2.1.6)$$

Where the surface integral has been extended to cover the entire external surface Ω , since displacements are prescribed on Ω^u , meaning that $\delta u_i = 0$ on Ω^u , and therefore Ω^u does not contribute to the second integral of Eq. (2.1.6). Note that V and Ω refer to the deformed configuration. In the deformed state an internal virtual work will exist due to the stress and strain fields within the deformable body. The internal virtual work W_{int} is calculated in Eq. (2.1.7). The stress field is described in terms of Cauchy's stress tensor σ_{ij} , which represents the force in the deformed configuration per unit deformed area. Cauchy's stress tensor is work conjugate with the Almansi strain tensor. For small deformation analyses, the Almansi strain tensor is equal to the infinitesimal strain tensor e_{ij} [Kildegaard, 2013], which is given in Eq. (2.1.5) when the last nonlinear term is ignored. The internal virtual work can then be calculated as:

$$\delta W_{int} = \int_V \sigma_{ij} \delta e_{ij} dV \quad (2.1.7)$$

Having obtained expressions for δW_{ext} and δW_{int} , the principle of virtual work can be formulated. In terms of physics the principle states: A necessary condition for equilibrium is that for any kinematically compatible deformation field $(\delta u_i; \delta e_{ij})$, the external virtual work, with statically compatible external forces¹, must equal the internal virtual work. Note the principle is independent of any constitutive law and applies to all materials, within the limitations of small deformations. Mathematically the principle reads:

$$\delta W_{ext} = \delta W_{int} \tag{2.1.8}$$

Having refreshed the principle of virtual work for a continuous system, it is now applied for a discontinuous system as shown in Fig. 2.2. In crack propagation problems, the displacement field will be discontinuous across an interior surface of the body. According to the principle of virtual work, the deformation field variations need to be kinematically compatible, which implies satisfaction of any prescribed displacement boundary conditions, and possessing continuous first order partial derivatives wrt. spatial coordinates in the interior of the body. However, in case of an interior surface of displacement discontinuity, the kinematic compatibility are not satisfied [Malvern, 1969]. Therefore, the principle of virtual work cannot be applied for the whole domain at once. To circumvent this issue, the principle of virtual work is applied for each subdomain, in which the derivatives of the displacement field, $u_{i,j}$, are continuous [Goyal, 2003], [Malvern, 1969], and formulate the local tractions/separations resulting from the crack opening as extra boundary conditions along the interfacial surfaces S^\pm .

Following the approach in [Goyal, 2003], the original domain V in Fig. 2.1, is now divided into two subdomains V^+ and V^- as illustrated in Fig. 2.2, which is divided by an interior strong singular discontinuous surface S , across which, the displacement field might exhibit jumps. The surface S represents an interfacial surface, and is bounded by the upper and lower surfaces of V^+ and V^- referred as S^+ and S^- respectively, which is illustrated in Fig. 2.3. The surfaces S , S^+ and S^- are defined by their outward unit normal vectors. Note the presence of a global fixed Cartesian coordinate system. The X_i coordinates denotes material coordinates in the undeformed configuration, while x_i denotes material coordinates in the deformed configuration.

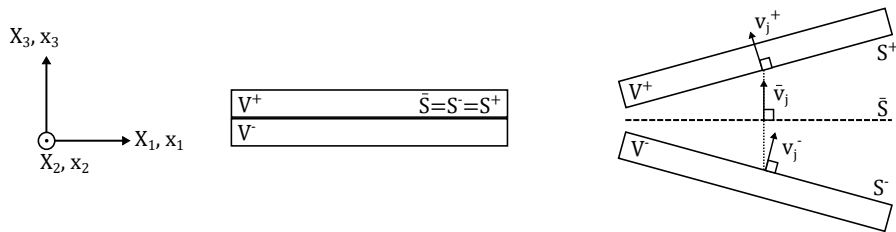


Figure 2.3: A simple planar representation of surfaces \bar{S} , S^+ , S^- and their outward unit normal vectors.

The surfaces S , S^+ and S^- are assumed to be coincident in the undeformed configuration, meaning the interface thickness is zero. During deformation, the surfaces S^+ and S^- displace independently of one another, creating a crack, having S^+ and S^- as newly formed crack faces. The crack faces are illustrated at the right end of Fig. 2.2. The arrows shown in the figure represent tractions, T_i^\pm , resulting from a material law, describing the interfacial surface.

¹The external loads are said to be statically compatible, if there is over all equilibrium for the body from a viewpoint of rigid-body mechanics.

The principle of virtual work, can be written separately for each continuous subdomain:

$$\int_{V^+} B_i \delta u_i dV + \int_{\Omega^+} \hat{T}_i^{(v)} \delta u_i d\Omega + \int_{S^+} T_i^+ \delta u_i^+ dS = \int_{V^+} \sigma_{ij} \delta e_{ij} dV \quad (2.1.9)$$

$$\int_{V^-} B_i \delta u_i dV + \int_{\Omega^-} \hat{T}_i^{(v)} \delta u_i d\Omega + \int_{S^-} T_i^- \delta u_i^- dS = \int_{V^-} \sigma_{ij} \delta e_{ij} dV \quad (2.1.10)$$

According to Newtons third law of action/reaction, the resultants due to the traction components acting on any interior surface must be continuous. However, the stress components are not necessarily continuous. A force balance equation is set up for the resultants acting on the interfacial surface [Goyal, 2003], that is for all $x_i \in S^\pm$, the following should apply:

$$\begin{aligned} \sigma_{ij}^+ v_j^+ dS^+ + \sigma_{ij}^- v_j^- dS^- &= 0 \quad \text{Or} \\ T_i^+ dS^+ + T_i^- dS^- &= 0 \quad \forall x_i \in S^\pm \end{aligned} \quad (2.1.11)$$

By adding Eq. (2.1.9) and Eq. (2.1.10), and substituting the relation in Eq. (2.1.11) in the resulting expression, one can obtain the following:

$$\begin{aligned} \int_V B_i \delta u_i dV + \int_\Omega \hat{T}_i^{(v)} \delta u_i d\Omega + \int_{S^+} T_i^+ (\delta u_i^+ - \delta u_i^-) \delta u_i dS &= \int_{V^+} \sigma_{ij} \delta e_{ij} dV \Leftrightarrow \\ \int_V B_i \delta u_i dV + \int_\Omega \hat{T}_i^{(v)} \delta u_i d\Omega &= \int_{V^+} \sigma_{ij} \delta e_{ij} dV - \int_{S^+} T_i^+ \delta (u_i^+ - u_i^-) dS \end{aligned} \quad (2.1.12)$$

Where it has also been utilized, that $V = V^+ + V^-$ and $\Omega = \Omega^+ + \Omega^-$. Note the variation in the second integral of the right hand side, $\delta(u_i^+ - u_i^-)$; this is an expression for the displacement jump across the surface.

A posteriori it is known to be convenient, to introduce an interfacial midsurface \bar{S} , from which the mechanics of the interface can be defined. The interior surface of strong discontinuity S is assumed coincide with the midsurface $S = \bar{S}$ throughout the deformation process. Accordingly, the traction and displacement jump vectors, will eventually be determined from this midsurface. The midsurface is defined as the average distance between points in S^+ and S^- which in the undeformed configuration is coincident. The mathematical description of the midsurface is explored further when the interface kinematics are also described in more detail in Sec. 2.1.3. For now, the midsurface is simply introduced in the governing equation of the interface, by reformulating the last integral of the right hand side of Eq. (2.1.12).

The previously defined tractions T_i^\pm are acting on the surfaces S^\pm . A traction vector associated with the midsurface is introduced as \bar{T}_i , whose components act in the direction of X_i . By use of Newtons third law, and treating the surface S^+ as reference, the traction acting on the midsurface is related to the traction acting on S^+ as follows:

$$T_i^+ dS^+ = -\bar{T}_i d\bar{S} \quad \forall x_i \in \{S^+; \bar{S}\}$$

With this relation, the governing equation in Eq. (2.1.12) can be rewritten in terms of the midsurface \bar{S} rather than the upper surface S^+ :

$$\int_V B_i \delta u_i dV + \int_\Omega \hat{T}_i^{(v)} \delta u_i d\Omega = \int_V \sigma_{ij} \delta e_{ij} dV + \int_{\bar{S}} \bar{T}_i \delta (u_i^+ - u_i^-) d\bar{S} \quad (2.1.13)$$

This equation is the principal of virtual work for a continuum with an interior surface of discontinuity in the displacement field. The expression is similar to the equation for a continuous system in Eq. (2.1.8), except the last integral which represents the virtual work done by the interfacial tractions in \bar{S} . The quantity \bar{T}_i is the interfacial traction component acting on

a unit deformed interfacial midsurface area, being work conjugate to the displacement jump, $(u_i^+ - u_i^-)$, and \bar{S} is the midsurface area.

Note the displacement jump component $(u_i^+ - u_i^-)$, is measured along the coordinate X_i . A description of the tractions and displacement jumps referring to the global coordinate system is not convenient, since it excludes the possibility to determine which traction and displacement jump components that are associated with normal and tangential directions of the midsurface. This is a complication in terms of the interface material law to be postulated, since it relies on knowing the normal and tangential directions locally at the midsurface. Therefore a local coordinate system will be defined, such that its basis vectors are normal and tangential to the midsurface \bar{S} . With this modification the virtual work of a discontinuous system reads:

$$\int_V B_i \delta u_i dV + \int_\Omega \hat{T}_i^{(v)} \delta u_i d\Omega = \int_V \sigma_{ij} \delta e_{ij} dV + \int_{\bar{S}} \Theta_{ij} \tau_j \delta (u_i^+ - u_i^-) d\bar{S} \quad (2.1.14)$$

Where τ_j are the interfacial traction components acting on a unit deformed interfacial midsurface area, Θ_{ij} is a second order rotation tensor relating the local midsurface coordinate system to the global fixed coordinate system (X_1, X_2, X_3) . With this modification, the components τ_j have a direct physical meaning in terms of normal and tangential directions to the midsurface; the components τ_1 and τ_2 are associated with tangential directions of the midsurface, while τ_3 is associated with the normal direction. The formulation of a proper rotation tensor and further elaboration on the local midsurface coordinate system are given in the following section.

2.1.3 Interface Kinematics

In the previous section it was argued, that the midsurface, \bar{S} , is assumed to follow the predefined crack path, S , depicted in Fig. 2.2. Additionally, the interfacial mechanics are referred to the midsurface, e.g. the traction vector components τ_j represents tangential and normal directions for a specific point on the midsurface. The crucial problem at hand is to determine the rotation tensor Θ_{ij} , which enables one to define the orientation of a local coordinate system $(\bar{e}_1, \bar{e}_2, \bar{e}_3)$, at some material point of the midsurface, \bar{S} , with respect to the global fixed Cartesian coordinate system (X_1, X_2, X_3) . Furthermore, the orientation of $(\bar{e}_1, \bar{e}_2, \bar{e}_3)$ should be expressed in terms of the upper and lower surface displacements u_i^\pm [Goyal, 2003].

Fig. 2.4 illustrates the deformation process of an arbitrary interfacial surface. Consider an arbitrary point P^0 in the undeformed configuration, here P^0 is coincident with more points: $P^+ \in S^+$ and $P^- \in S^-$. During the deformation process, the points will displace as described by vectors u_i^\pm . From the geometrical definition of the midsurface \bar{S} , a midpoint, \bar{P} , defined as the average distance between surfaces S^+ and S^- , will define a point within the midsurface, as illustrated by the point $\bar{P} \in \bar{S}$ in Fig. 2.4. In [Goyal, 2003] is an equation for points within the midsurface derived, \bar{x}_i , in terms of the global Cartesian coordinate system as:

$$\bar{x}_i = X_i + \frac{1}{2} (u_i^+ - u_i^-) \quad (2.1.15)$$

Where X_i are the coordinates of an arbitrary material point, e.g. P^0 , in the undeformed configuration, and u_i^\pm describes the displacement, measured along X_i , of the material point. Note the middle surface is coincident with S^0 when $u_i^+ = u_i^- = 0$.

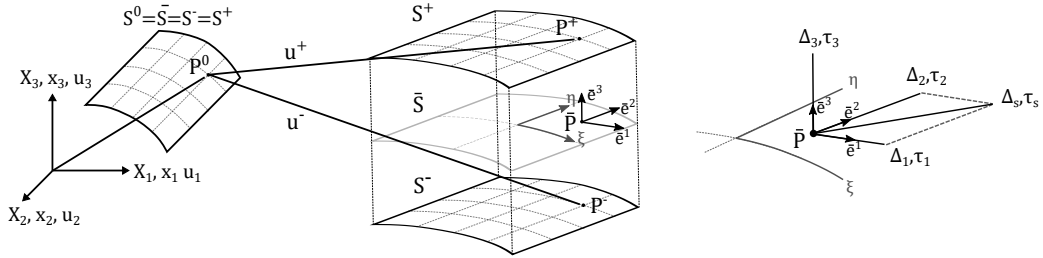


Figure 2.4: A cut-out of the crack path surface Γ^d in deformed and undeformed configuration.

Following the procedure in [Goyal, 2003], the local coordinate system, $(\bar{e}^1, \bar{e}^2, \bar{e}^3)$, is derived from a curvilinear coordinate system (ξ, η) located on the midsurface, as illustrated in the deformed configuration of Fig. 2.4. The tangential directions are obtained as the curvilinear gradients of the midsurface:

$$\nu_{\xi i} = \bar{x}_{i,\xi} \quad (2.1.16)$$

$$\nu_{\eta i} = \bar{x}_{i,\eta} \quad (2.1.17)$$

However, the curvilinear coordinates, and hence the gradients $\nu_{\xi i}$ and $\nu_{\eta i}$, are not in general mutually orthogonal. Alternatively, a local orthonormal coordinate system based on cross products and norms of the tangential curvilinear gradients is established. The i 'th component of the local coordinate system is denoted $(\bar{e}_i^1, \bar{e}_i^2, \bar{e}_i^3)$ and given as follows:

$$\bar{e}_i^1 = \frac{\nu_{\xi i}}{|\nu_{\xi i}|}, \quad \bar{e}_i^3 = \frac{\nu_{\xi i} \times \nu_{\eta i}}{|\nu_{\xi i} \times \nu_{\eta i}|}, \quad \bar{e}_i^2 = \bar{e}_i^3 \times \bar{e}_i^1, \quad \Theta_{ij} = \begin{bmatrix} \bar{e}_1^1 & \bar{e}_2^1 & \bar{e}_3^1 \\ \bar{e}_1^2 & \bar{e}_2^2 & \bar{e}_3^2 \\ \bar{e}_1^3 & \bar{e}_2^3 & \bar{e}_3^3 \end{bmatrix} \quad (2.1.18)$$

The components of $(\bar{e}_i^1, \bar{e}_i^2, \bar{e}_i^3)$ defines the rotation/transformation tensor Θ_{ij} at some material point $\bar{P} \in \bar{S}$.

The rotation tensor can be utilized to express the displacement jump vector, $(u_i^+ - u_i^-)$, in terms of normal and tangential directions in the local coordinate system at any material point in the midsurface \bar{S} . The resulting vector is denoted as the local displacement jump vector, Δ_i :

$$\Delta_i = \Theta_{ij}(u_i^+ - u_i^-) \quad (2.1.19)$$

The rotation tensor enables one to relate a global coordinate system to a local coordinate system, and identify tangential and normal directions locally. However, the rotation tensor is formulated without reference to the orientation of the crack front. Consequently, the kinematic interface model is incapable of distinguishing between the crack opening modes associated with the tangential direction of the overall crack front, hence shear modes mode II and mode III are indistinguishable. Therefore, a combined shear mode is often introduced, which is spanned by the local tangential directions \bar{e}^1 and \bar{e}^2 . This is illustrated by τ_s and Δ_s in Fig. 2.4.

2.1.4 Cont'd Principal of Virtual Work for Discontinuous Systems

In the previous sections, the strong form of the boundary value problem at hand has been transformed into a weak formulation by setting up a functional using virtual work principles. The weak form is given in Eq. (2.1.14). The surfaces and volume integrals in Eq. (2.1.14) refers to the volume and surfaces in the deformed configuration. The volume integral on the right hand side, which represents the internal virtual work of the bulk material, is now modified to be evaluated over the reference volume V^0 . This modification enables one to apply the Green-Lagrange strain tensor including the nonlinear terms given in Eq. (2.1.5). This strain tensor refers to the undeformed configuration and is capable of representing large strains, which in general is encountered in crack propagation problems [Goyal, 2003]. In order to have a work conjugate pair of stress and strain tensors in the functional, the stress tensor is also modified to the second Piola-Kirchhoff stress tensor (PK2), S_{ij} . The modified governing equation is shown in Eq. (2.1.20).

$$\int_V B_i \delta u_i dV + \int_\Omega \hat{T}_i^{(v)} \delta u_i d\Omega = \int_{V^0} S_{ij} \delta \varepsilon_{ij} dV + \int_{\bar{S}} \Theta_{ij} \tau_j \delta (u_i^+ - u_i^-) d\bar{S} \quad (2.1.20)$$

The switch of stress and strain tensors in calculating the internal virtual work of the bulk material changes nothing in the derivation process. The fundamental concept of the principle of virtual work for finite deformation analysis is the same as in case of infinitesimal deformation analysis. However, it necessitates to distinguish between undeformed and deformed configurations and use a suitable pair of work conjugate stress and strain tensors.

For convenience is the expression in Eq. (2.1.20) rewritten to a residual form as shown in Eq. (2.1.21). The variation of internal virtual work is shown as δW_{int} , representing variations of the work done by the stress state S_{ij} . The variation of the external work is shown as δW_{ext} and represents the variation of the work done by body forces and tractions acting on the external surface. The remaining integral represents work done by interfacial tractions.

$$I(u_i) = \underbrace{\int_V B_i \delta u_i dV + \int_\Omega \hat{T}_i^{(v)} \delta u_i d\Omega}_{\delta W_{ext}} - \left(\underbrace{\int_{V^0} S_{ij} \delta \varepsilon_{ij} dV + \int_{\bar{S}} \Theta_{ij} \tau_j \delta (u_i^+ - u_i^-) d\bar{S}}_{\delta W_{int}} \right) = 0 \quad (2.1.21)$$

2.1.5 Finite Element Discretization

The boundary value problem is too complex to be solved analytically for general structures and nonlinearities. Therefore a numerical solution is sought. The standard displacement based finite element method is used in this report to solve the system of nonlinear equations. The sources of nonlinearity are material nonlinearity of the interface material law, and potentially geometrical nonlinearity of the bulk material, which is often encountered in crack propagation problems [Goyal, 2003].

The FEM is based on weak formulations, i.e. the functional depends not on the state variables and its derivatives at a particular material point, but upon their integrated effect over the whole domain. Consequently, the boundary value problem is solved in weak form which means that conditions that must be fulfilled such as equilibrium conditions and non-essential boundary conditions (in general stress boundary conditions) are only satisfied in an average sense, and not at every material point [Cook et al., 2002].

The current mathematical model of the boundary value problem in Eq. (2.1.21) is exact and contains an infinite number of degrees of freedom (d.o.f.) (namely the displacement components of every material point). The FEM substitutes the exact mathematical model with an approximate mathematical model², by introduction of assumed displacement fields \tilde{u}_i and a finite number of degrees of freedom in the functional $I(u_i)$. However, the assumed displacement fields impose artificial constraints on the original mathematical model, since only a subclass of displacement fields are possible and therefore the displacement field is enforced to have a certain spatial variation. Consequently, the approximate solution is in general overly stiff compared to the original mathematical model [Cook et al., 2002].

The introduction of assumed displacement fields is done by discretizing the domain into a finite number of subdomains (elements), and interpolate the displacement field within each element from nodal d.o.f. d_k through use of shape functions N_{ik} .

$$\tilde{u}_i = N_{ik}d_k \quad (2.1.22)$$

The virtual displacement field $\delta\tilde{u}_i$ must be kinematically compatible, i.e. satisfy essential boundary conditions. The assumed displacement field \tilde{u}_i is a function of the nodal displacements. The variation of the assumed displacement field is obtained as:

$$\delta\tilde{u}_i = \frac{\partial\tilde{u}_i}{\partial d_k}\delta d_k = \frac{\partial}{\partial d_k}(N_{ik}d_k)\delta d_k = N_{ik}\delta d_k \quad (2.1.23)$$

Keeping in mind that the virtual displacement field $\delta\tilde{u}_i$ is a function of nodal displacements δd_k , the residual expression, $I(u_i)$ in Eq. (2.1.21) can be rewritten as:

$$I(\tilde{u}_i) = \int_V B_i \frac{\partial\tilde{u}_i}{\partial d_k} \delta d_k dV + \int_\Omega \hat{T}_i^{(v)} \frac{\partial\tilde{u}_i}{\partial d_k} \delta d_k d\Omega - \left(\int_{V^0} S_{ij} \frac{\partial\varepsilon_{ij}}{\partial d_k} \delta d_k dV + \int_{\bar{S}} \Theta_{ij}\tau_j \frac{\partial(u_i^+ - u_i^-)}{\partial d_k} \delta d_k d\bar{S} \right) = 0 \quad (2.1.24)$$

Direct application of the relation in Eq. (2.1.23) is used to rewrite this expression further. Additionally, since the virtual nodal displacement components δd_k are constants with respect to the integrations, these can be moved out side the integral signs.

$$I(\tilde{u}_i) = \delta d_k \left(\int_V B_i N_{ik} dV + \int_\Omega \hat{T}_i^{(v)} N_{ik} d\Omega - \left(\int_{V^0} S_{ij} \frac{\partial\varepsilon_{ij}}{\partial d_k} dV + \int_{\bar{S}} \Theta_{ij}\tau_j \frac{\partial(u_i^+ - u_i^-)}{\partial d_k} d\bar{S} \right) \right) = 0 \quad (2.1.25)$$

²A finite element form of the Ritz method.

The principle of virtual work states that equilibrium between internal and external virtual works, $I = 0$, should prevail for *any* small kinematical compatible variation of the displacement field. Given that the nodal displacement variables satisfy essential boundary conditions, the components δd_k can be chosen arbitrarily and independently of one another. Consequently, each nodal variable δd_k could be chosen non-zero, while the remaining nodal variables are identically zero. Thus for a finite system of n d.o.f. there exists n associated equations given as follows, for $k=1\dots n$:

$$I_k = \int_V B_i N_{ik} dV + \int_{\Omega} \hat{T}_i^{(v)} N_{ik} d\Omega - \left(\int_{V^0} S_{ij} \frac{\partial \varepsilon_{ij}}{\partial d_k} dV + \int_{\bar{S}} \Theta_{ij} \tau_j \frac{\partial (u_i^+ - u_i^-)}{\partial d_k} d\bar{S} \right) = 0 \quad (2.1.26)$$

Given the discretization of the whole domain into a finite number of elements, the volume and surface integrals can conveniently be split into a sum of integrals over each element volume and element surface, respectively. Suppose the whole element is divided into a number of $nElem$ elements, Eq. (2.1.26) can then be written as:

$$I_k = \sum_{m=1}^{nElem} \int_{V_m^e} B_i N_{ik} dV + \int_{\Omega_m^e} \hat{T}_i^{(v)} N_{ik} d\Omega - \left(\int_{V_m^{0e}} S_{ij} \frac{\partial \varepsilon_{ij}}{\partial d_k} dV + \int_{\bar{S}_m^e} \Theta_{ij} \tau_j \frac{\partial (u_i^+ - u_i^-)}{\partial d_k} d\bar{S} \right) = 0 \quad (2.1.27)$$

It is noted that equations I_k are formulated in four different integration domains: V^e , Ω^e , V^{0e} and \bar{S}^e . V^e represents the volume of an element within the bulk material in the deformed configuration. Ω^e represents the surface area of a boundary (external) element. V^{0e} represents the element volume of an element within the bulk material in the undeformed configuration. \bar{S}^e represents the midsurface area of an interface element in its deformed configuration. Consequently, for a given element number m in Eq. (2.1.27), not all integral terms enters the summation, since it depends on the element type. It is also noted that no extra approximations to the mathematical model are introduced by splitting the total volume and surface integrals into a sum of volume and surface integrals evaluated on element level and subsequently summed up.

Eq. (2.1.27) forms the governing system of equations for the finite element analysis to be conducted. The system consists of n equations in n unknowns. Each equation, k , represents an equilibrium equation which is obtained by discretization of the principle of virtual work for a discontinuous system, taking into account possible large deformations of the bulk material, and nonlinearity of the interfacial material law. The governing equation and the variables are summarized here in compact notation:

$$I_k(d_1, d_2, \dots, d_n) = 0, \quad \text{for } k = 1 \dots n \quad (2.1.28)$$

The integrals are evaluated numerically using Newton-Cotes quadrature rules. Regarding the interface elements, the order of integration rule applied, depends on the element damage state. In this work, for undamaged and fully damaged elements, a two point quadrature rule is used, while elements under damage development uses a 10 point quadrature rule, as suggested in [Bak et al., 2014].

2.2 Constitutive Relation

Formulating constitutive equations for a cohesive zone model, requires one to calculate cohesive tractions τ_i for any local displacement jump Δ_j . Additionally, to numerically implement the constitutive law, a constitutive tangent stiffness tensor is needed, to relate variations in tractions to variations in local displacement jumps. This is a necessity since the crack propagation problem is inherently nonlinear and must be solved incrementally.

Based on the derivation in [Turon et al., 2006] an expression for cohesive tractions for any value of the local displacement jump vector Δ_j and damage parameter d is given in Eq. (2.2.1):

$$\tau_i = (1 - d)D_{ij}^0\Delta_j \quad (2.2.1)$$

Wherein D_{ij}^0 is a second order stiffness tensor of the undamaged material, which in turn corresponds to the penalty stiffness. In case of equal elastic stiffness $K^{(eq)}$ in all three directions the tensor reduces to $D_{ij}^0 = K^{(eq)}\delta_{ij}$. As damage develops, the effective stiffness decreases. Negative values of the local displacement jump vector associated with mode I deformation, Δ_3 , would result in interfacial penetration of two layers. This do not have any physical meaning, because interpenetration is prevented by contact. Therefore a modification of Eq. (2.2.1) is proposed [Turon et al., 2006]:

$$\tau_i = (1 - d)D_{ij}^0\Delta_j - dD_{ij}^0(\delta_{3j}\langle -\Delta_3 \rangle) \quad (2.2.2)$$

In which $\langle \cdot \rangle$ is the MacAuley bracket defined as $\langle x \rangle = \frac{1}{2}(x + |x|)$. The modification ensures, that in case of negative Δ_3 the stiffness is unaffected by damage and becomes equal to the penalty stiffness, such that $\tau_3 = K_{33}\Delta_3$. This is clarified by writing the equation above in Voigt notation:

$$\begin{Bmatrix} \tau_1 \\ \tau_2 \\ \tau_3 \end{Bmatrix} = (1 - d) \begin{bmatrix} K_{11} & 0 & 0 \\ 0 & K_{22} & 0 \\ 0 & 0 & K_{33} \end{bmatrix} \begin{Bmatrix} \Delta_1 \\ \Delta_2 \\ \Delta_3 \end{Bmatrix} - d \begin{bmatrix} K_{11} & 0 & 0 \\ 0 & K_{22} & 0 \\ 0 & 0 & K_{33} \end{bmatrix} \begin{Bmatrix} 0 \\ 0 \\ \langle -\Delta_3 \rangle \end{Bmatrix} \quad (2.2.3)$$

The constitutive relation in Eq. (2.2.2) is completely defined if a damage evolution law describing the damage parameter at every time instant during the deformation process is formulated. However, before considering this further, the formulation of a constitutive tangent stiffness tensor is considered.

2.2.1 Constitutive Tangent Stiffness Tensor

The rate of change of tractions is related to the rate of change of the separations by the constitutive tangent stiffness tensor as expressed in Eq. (2.2.4):

$$\frac{d\tau_i}{dt} = D_{ij}^{tan} \frac{d\Delta_j}{dt} \quad (2.2.4)$$

Where t represents a pseudo solution time during a nonlinear solution process. This relation might equivalently be written in terms of variations as: $\delta\tau_i = D_{ij}^{tan}\delta\Delta_j$. Prior to deriving an expression for the tangent stiffness tensor, its situation dependent behaviour is highlighted; the tangent stiffness tensor not only depends on the current state of damage, but also whether loading/unloading/reloading is expected.

To establish an expression for the constitutive tangent stiffness tensor one needs the time derivative of Eq. (2.2.2). It is assumed that the penalty elastic stiffnesses in the 1-,2-, and 3-direction are equal, such that $D_{ij}^0 = K^{(eq)}\delta_{ij}$. Recalling that both the damage parameter d

and the interfacial separation Δ_j are functions of time.

$$\frac{d\tau_i}{dt} = -\dot{d}D_{ij}^0\Delta_j + (1-d)D_{ij}^0\dot{\Delta}_j - \dot{d}D_{ij}^0\delta_{3j}\langle-\Delta_3\rangle - dD_{ij}^0\delta_{3j}\frac{d(\langle-\Delta_3\rangle)}{dt}$$

Considering the last term and rewriting this:

$$\begin{aligned} -dD_{ij}^0\delta_{3j}\frac{d(\langle-\Delta_3\rangle)}{dt} &= -dD_{ij}^0\delta_{3j}\frac{\partial\langle-\Delta_3\rangle}{\partial\Delta_3}\frac{d\Delta_3}{dt} = \\ -dD_{ij}^0\delta_{3j}\frac{\langle-\Delta_3\rangle}{\Delta_3}\dot{\Delta}_3 &= -dD_{ij}^0\delta_{3j}\frac{\langle-\Delta_j\rangle}{\Delta_j}\dot{\Delta}_j \end{aligned}$$

Substituting this term into the expression for $d\tau_i/dt$, and using the relation $D_{ij}^0 = \delta_{ij}K^{(eq)}$

$$\begin{aligned} \dot{\tau}_i &= -\dot{d}\delta_{ij}K^{(eq)}\Delta_j + (1-d)\delta_{ij}K^{(eq)}\dot{\Delta}_j - \dot{d}\delta_{ij}K^{(eq)}\delta_{3j}\langle-\Delta_3\rangle - d\delta_{ij}K^{(eq)}\delta_{3j}\frac{\langle-\Delta_j\rangle}{\Delta_j}\dot{\Delta}_j \quad \Leftrightarrow \\ \dot{\tau}_i &= \delta_{ij}K^{(eq)}\left[(1-d) - d\delta_{3j}\frac{\langle-\Delta_j\rangle}{\Delta_j}\right]\dot{\Delta}_j - \delta_{ij}K^{(eq)}[\Delta_j + \delta_{3j}\langle-\Delta_3\rangle]\dot{d} \quad \Leftrightarrow \\ \dot{\tau}_i &= \delta_{ij}K^{(eq)}\left[1 - d\left(1 + \delta_{3j}\frac{\langle-\Delta_j\rangle}{\Delta_j}\right)\right]\dot{\Delta}_j - \delta_{ij}K^{(eq)}\left[1 + \delta_{3j}\frac{\langle-\Delta_j\rangle}{\Delta_j}\right]\Delta_j\dot{d} \quad (2.2.5) \end{aligned}$$

Thus, under the assumption of equal elastic stiffnesses in the 1-, 2-, and 3-direction, the time derivative of the interfacial traction $\dot{\tau}_i$ is given in Eq. (2.2.5). Since D_{ij}^{tan} explicitly relates $\dot{\tau}_i$ to $\dot{\Delta}_j$, an expression for the damage parameter d and its time derivative \dot{d} are still required. This is a topic of the following sections concerning the formulation of a damage model.

2.3 Damage Mechanics Model

A cohesive zone model is partially formulated in the framework of damage continuum mechanics, which motivates a further explanation of the damage parameter and its evolution, which is the topic of the current section. To arrive at an expression for the damage evolution law, the concept of an equivalent mixed mode CZ law is introduced and a discussion of mode mixity interaction is given.

The damage model describes the evolution of the damage parameter, d , which controls the degradation of the interface stiffness. The damage parameter is a scalar, which should develop concurrently with the energy dissipation during the fracture process. For an undamaged interface, the damage parameter is equal to zero, $d = 0$, and upon full damage it is equal unity $d = 1$, in which case, the effective interface stiffness is equal to zero. The damage parameter function must be monotonically increasing during the deformation process to ensure irreversibility.

Various approaches to formulate a mixed mode CZ model exists, such as models with decoupled mode I and II, potential based models, and equivalent one-dimensional cohesive zone models. In this report, the latter approach of an equivalent mixed mode CZ law is applied, i.e. a scalar expression relating norms of the traction and separation vectors as function of the damage parameter d will be established. Ergo, although the cohesive state is described by vectors of several components, the resulting CZ law is a one-dimensional law in terms of traction- and separation vector norms. The evolution of the damage parameter is controlled by this equivalent mixed mode CZ law.

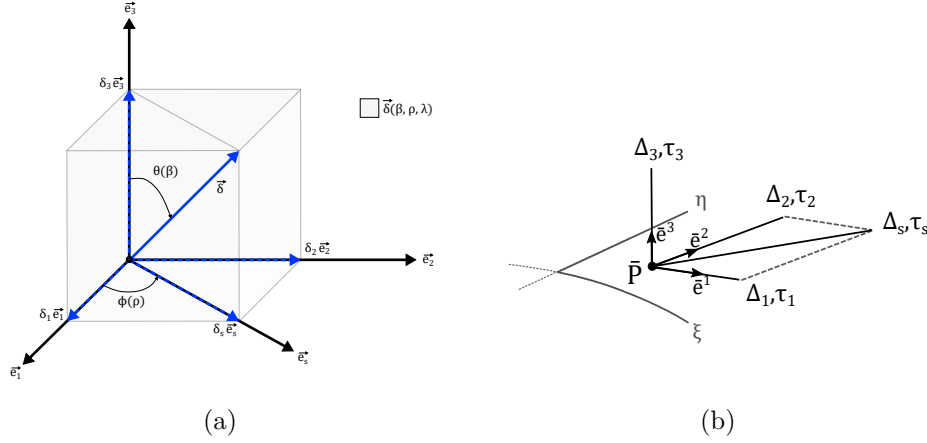


Figure 2.5: (a) Separation vector $\vec{\delta}$ and its components for use in damage models. 3D description includes the whole light grey box, while the 2D description is confined to the blue plane. (b) Local coordinate system at interfacial midsurface \bar{S} .

Damage development is directly related to fracture energy dissipation. The damage model is only concerned with tractions and separations that affect damage development. Hence, the full kinematic and constitutive relations given in the previous sections in terms of $\vec{\Delta}$ and $\vec{\tau}$, contains redundant information concerning situations where either no damage develops or cases where the damage development is identical. E.g. in case of $\Delta_3 < 0$ no damage will develop, and independently of the sign of shear associated separations, the damage development is the same.

Therefore, the damage model constitutive and kinematic equations are simplified to represent only tractions and separations that contribute to fracture energy dissipation. For this purpose, a new notation is introduced for use in the damage model. Here $\vec{\sigma}$ and $\vec{\delta}$ will represent tractions and separations in the cohesive zone respectively. These are related to the previously defined tractions and separations as follows:

$$\vec{\delta} = [\delta_1 \ \delta_2 \ \delta_3]^T = [|\Delta_1| \ |\Delta_2| \ \langle \Delta_3 \rangle]^T \quad (2.3.1)$$

$$\vec{\sigma} = [\sigma_1 \ \sigma_2 \ \sigma_3]^T = [|\tau_1| \ |\tau_2| \ \langle \tau_3 \rangle]^T \quad (2.3.2)$$

Note it is assumed that negative normal openings, $\Delta_3 < 0$, do not affect damage development, and positive and negative values of shear mode openings are treated equally. The two upcoming subsections regarding damage kinematic and damage constitutive relations, Sec. 2.3.1 and 2.3.2 respectively, are inspired by [Hansen and Lund, 2009], wherein the equivalent one-dimensional CZ law is also derived, but in a different kinematic description. In [Hansen and Lund, 2009], the mode mixity is described in terms trigonometric functions of angles θ and ϕ , whereas the kinematic description here is described in terms of mode mixity ratios β and ρ .

2.3.1 Damage Kinematic Relations

A local coordinate system at some point in the cohesive zone is shown in Fig. 2.5b. The coordinate system is spanned by three unit vectors \vec{e}_1 , \vec{e}_2 and \vec{e}_3 which are assumed to be associated with crack opening modes III, II and I, respectively. The separation vector $\vec{\delta}$ is shown in Fig. 2.5a in spherical coordinates; it is completely defined by its norm λ , and two angles $\theta(\beta)$ and $\phi(\varrho)$ describing the mode mixity. However, the angles are only used for illustration purposes, the mode mixity is actually described by parameters β and ϱ (to be defined). A shear separation norm is introduced as δ_s :

$$\delta_s = \sqrt{(\delta_1)^2 + (\delta_2)^2} \quad (2.3.3)$$

which makes the notation convenient. A single separation parameter is introduced as the Euclidean norm of δ_3 and δ_s and is denoted by λ :

$$\lambda = \sqrt{(\delta_3)^2 + (\delta_s)^2} \quad (2.3.4)$$

λ is referred to as the equivalent displacement jump norm. It is a non-negative and continuous function containing the MacAuley bracket in the definition of δ_3 . The introduction of an equivalent displacement jump norm, λ , in the damage model is convenient. It gives the possibility to define concepts of loading, unloading and reloading, since it provides one equivalent, or accumulated, measure of the displacement jump state. For instance how would one define whether the local displacement jump is in a state of unloading or loading, if δ_1 and δ_2 are both increasing, but δ_3 is slightly decreasing.

A mixed mode equivalent CZ law can be formulated on the basis of λ and mode mixity ratios. The mode mixity ratios are quantified by parameters β and ϱ and are given in Eq. (2.3.5). These mode mixity ratios are evaluated at every point in the cohesive zone from the separation components δ_i .

$$\beta = \frac{\delta_s}{\delta_s + \delta_3} \quad \varrho = \frac{\delta_2}{\delta_2 + \delta_1} \quad (2.3.5)$$

By comparing these expressions with Fig. 2.5a and 2.5b, it is seen that $\beta = 0$ corresponds to pure mode I, $\beta = 1 \wedge \varrho = 0$ corresponds to pure mode III, and $\beta = 1 \wedge \varrho = 1$ corresponds to pure mode II. Note by the introduction of ϱ , it is assumed that the mode II and mode III associated separations can be distinguished. To the authors knowledge, this has not yet been successfully implemented in a finite element model context, since the global orientation of the crack front with respect to the specimen dimensions and orientations are unknown. However, to keep the derivation of a mixed mode CZ law general, it is assumed that mode II and mode III separations can be distinguished, unless stated otherwise. The expressions in Eq. (2.3.5) can be rewritten such that ratios of the separation components are obtained:

$$\frac{\delta_3}{\delta_s} = \frac{1 - \beta}{\beta} \quad \frac{\delta_1}{\delta_2} = \frac{1 - \varrho}{\varrho} \quad (2.3.6)$$

Using the definition of λ in Eq. (2.3.4) and the expressions above, the following relations have been derived:

$$\frac{\delta_3}{\lambda} = \frac{1 - \beta}{\hat{\beta}}; \quad \frac{\delta_s}{\lambda} = \frac{\beta}{\hat{\beta}} \quad (2.3.7)$$

$$\frac{\delta_1}{\delta_s} = \frac{1 - \varrho}{\hat{\varrho}}; \quad \frac{\delta_2}{\delta_s} = \frac{\varrho}{\hat{\varrho}} \quad (2.3.8)$$

Wherein the values denoted by hat ($\hat{\cdot}$) are given as:

$$\hat{\beta} = \sqrt{1 + 2\beta^2 - 2\beta} \quad \hat{\varrho} = \sqrt{1 + 2\varrho^2 - 2\varrho} \quad (2.3.9)$$

Kinematic relations for every separation component δ_i can then be written in terms of the mode mixity parameters β and ϱ and the equivalent displacement jump norm λ , as given in Eq. (2.3.10) and illustrated in Fig. 2.5a.

$$\vec{\delta} = \begin{Bmatrix} \delta_1 \\ \delta_2 \\ \delta_3 \end{Bmatrix} = \lambda \begin{Bmatrix} \frac{\beta(1-\varrho)}{\hat{\beta}} \\ \frac{\beta\varrho}{\hat{\beta}} \\ \frac{1-\beta}{\hat{\beta}} \end{Bmatrix} \quad (2.3.10)$$

It is noted that the norm of the vector enclosed in curly brackets on the right hand side is equal to unity independently of the values of β and ϱ , hence the length of the separation vector is $|\vec{\delta}| = \lambda$. The separation vector $\vec{\delta}$ is then expressed as a function of the equivalent displacement jump norm and the mode mixity ratios.

2.3.2 Damage Constitutive Relation

The damage constitutive equation is written in terms of the traction- and separation vectors, the damage parameter and penalty stiffnesses in Eq. (2.3.11). Note that is written in terms of $\vec{\sigma}$ and $\vec{\delta}$ rather than $\vec{\tau}$ and $\vec{\Delta}$ for the reason explained in the beginning of this Sec. 2.3, regarding traction and separation values contributing to fracture energy dissipation.

$$\vec{\sigma} = (1-d)[D^0]\vec{\delta}; \quad [D_0] = \begin{bmatrix} K_{11} & 0 & 0 \\ 0 & K_{22} & 0 \\ 0 & 0 & K_{33} \end{bmatrix} \quad (2.3.11)$$

Non-isotropy of the elastic stiffness matrix $[D^0]$ is taken into account by allowing the penalty stiffnesses K_{ii} to be different. In the previous section, when D_{ij}^{tan} was derived, the elastic stiffnesses were assumed identical in all three directions, such that $K_{ii} = K^{(ea)}$. However, non-isotropy is taken into account for the sake of generality.

Eventually, the damage constitutive relation reduces to a scalar expression in terms of the norm of the separation and traction vectors known as the equivalent mixed mode CZ law. For the pair of traction and separation norms to be work conjugate, the vector associated with the work conjugate traction norm needs to be coincident with the separation vector $\vec{\delta}$. Reconsidering the damage constitutive relations in Eq. (2.3.11), the non-isotropy of the elastic stiffness matrix $[D^0]$ can cause the traction vector $\vec{\sigma}$ to be non-coincident with the separation vector $\vec{\delta}$, as illustrated in Fig. 2.6. Consequently the traction vector $\vec{\sigma}$ is in general not work conjugate with the separation vector $\vec{\delta}$.

To circumvent this issue, a work conjugate traction vector, denoted by a bar $\vec{\bar{\sigma}}$, is introduced, as the projection of $\vec{\sigma}$ onto $\vec{\delta}$, and denoted by $\vec{\bar{\sigma}}$.

$$\vec{\bar{\sigma}} = \mathbf{proj}_{\vec{\delta}}(\vec{\sigma}) = \frac{\vec{\sigma} \cdot \vec{\delta}}{\vec{\delta} \cdot \vec{\delta}} \vec{\delta} \quad (2.3.12)$$

This traction vector is coincident with the separation vector as illustrated in Fig. 2.6. Considering the numerator and the denominator of this fraction separately. By the definition of Euclidean norm of a vector, the denominator reduces to the following: $\vec{\delta} \cdot \vec{\delta} = |\vec{\delta}|^2 = \lambda^2$. The numerator $\vec{\sigma} \cdot \vec{\delta}$ is calculated as follows:

$$\begin{Bmatrix} \sigma_1 \\ \sigma_2 \\ \sigma_3 \end{Bmatrix} \cdot \begin{Bmatrix} \frac{\beta(1-\varrho)}{\hat{\beta}} \\ \frac{\beta\varrho}{\hat{\beta}} \\ \frac{1-\beta}{\hat{\beta}} \end{Bmatrix} \lambda = \left(\sigma_1 \frac{\beta(1-\varrho)}{\hat{\beta}} + \sigma_2 \frac{\beta\varrho}{\hat{\beta}} + \sigma_3 \frac{1-\beta}{\hat{\beta}} \right) \lambda$$

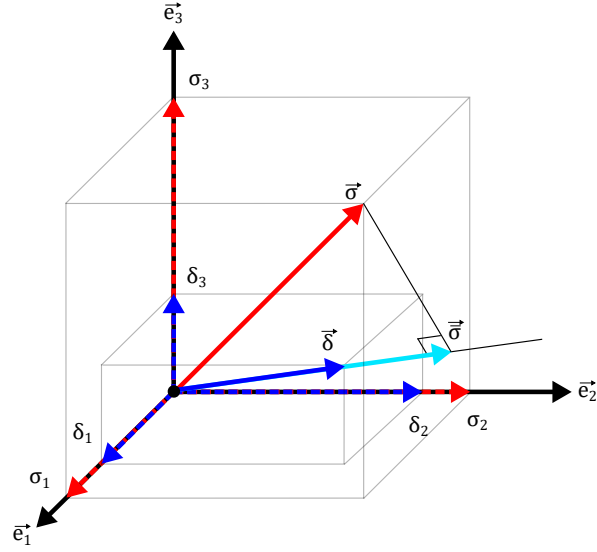


Figure 2.6: Concept of work conjugate traction norm, the figure is based on [Hansen and Lund, 2009]

The right hand side in Eq. (2.3.12) can then be written as follows:

$$\begin{aligned}\vec{\sigma} &= \left(\sigma_1 \frac{\beta(1-\varrho)}{\hat{\beta}\hat{\varrho}} + \sigma_2 \frac{\beta\varrho}{\hat{\beta}\hat{\varrho}} + \sigma_3 \frac{1-\beta}{\hat{\beta}} \right) \frac{\lambda}{\lambda^2} \vec{\delta} \Leftrightarrow \\ \vec{\sigma} &= \left(\sigma_1 \frac{\beta(1-\varrho)}{\hat{\beta}\hat{\varrho}} + \sigma_2 \frac{\beta\varrho}{\hat{\beta}\hat{\varrho}} + \sigma_3 \frac{1-\beta}{\hat{\beta}} \right) \frac{\vec{\delta}}{\lambda}\end{aligned}\quad (2.3.13)$$

An expression for a mixed mode work conjugate traction vector is then obtained. The norm of this vector is denoted $\bar{\sigma} = |\vec{\sigma}|$, being the mixed mode work conjugate traction norm, which plays an essential role when establishing the equivalent mixed mode CZ law. The norm of $\vec{\sigma}$ is readily calculated from Eq. (2.3.13) since $|c\vec{\delta}| = c|\vec{\delta}|$ with c being a scalar and the norm of the separation vector $|\vec{\delta}| = \lambda$. Hence, the fraction $\vec{\delta}/\lambda$ at the far right end cancels, and the norm of $\vec{\sigma}$ becomes:

$$\bar{\sigma} = \sigma_1 \frac{\beta(1-\varrho)}{\hat{\beta}\hat{\varrho}} + \sigma_2 \frac{\beta\varrho}{\hat{\beta}\hat{\varrho}} + \sigma_3 \frac{1-\beta}{\hat{\beta}} \quad (2.3.14)$$

Having established an expression for the work conjugate traction norm, the mixed mode CZ law can be calculated by using the damage constitutive relation in Eq. (2.3.11) and the damage kinematic relations in Eq. (2.3.10). Substituting the kinematic relation into Eq. (2.3.11), one obtains the following:

$$\begin{aligned}\begin{Bmatrix} \sigma_1 \\ \sigma_2 \\ \sigma_3 \end{Bmatrix} &= (1-d) \begin{bmatrix} K_{11} & 0 & 0 \\ 0 & K_{22} & 0 \\ 0 & 0 & K_{33} \end{bmatrix} \begin{Bmatrix} \frac{\beta(1-\varrho)}{\hat{\beta}\hat{\varrho}} \\ \frac{\beta\varrho}{\hat{\beta}\hat{\varrho}} \\ \frac{1-\beta}{\hat{\beta}} \end{Bmatrix} \lambda \Leftrightarrow \\ \begin{Bmatrix} \sigma_1 \\ \sigma_2 \\ \sigma_3 \end{Bmatrix} &= (1-d) \begin{Bmatrix} K_{11} \frac{\beta(1-\varrho)}{\hat{\beta}\hat{\varrho}} \\ K_{22} \frac{\beta\varrho}{\hat{\beta}\hat{\varrho}} \\ K_{33} \frac{1-\beta}{\hat{\beta}} \end{Bmatrix} \lambda\end{aligned}$$

The expression for every traction component σ_i is then substituted into Eq. (2.3.14) from which the following expression for the work conjugate traction norm can be obtained:

$$\bar{\sigma} = K(1 - d)\lambda \quad (2.3.15)$$

$$K = K_{11} \left(\frac{\beta(1 - \varrho)}{\hat{\beta}\hat{\varrho}} \right)^2 + K_{22} \left(\frac{\beta\varrho}{\hat{\beta}\hat{\varrho}} \right)^2 + K_{33} \left(\frac{1 - \beta}{\hat{\beta}} \right)^2 \quad (2.3.16)$$

This equation is referred to as the one-dimensional equivalent CZ law. It describes a relation between a work conjugate traction norm $\bar{\sigma}$ and the equivalent displacement jump norm λ as a function of the mode mixity ratios β and ϱ , the damage parameter d and elastic penalty stiffness parameters K_{ii} . The K parameter in Eq. (2.3.16) is an equivalent mixed mode penalty stiffness and is also given in the equation above. In the special case of equal elastic stiffness, e.g. $K_{11} = K_{22} = K_{33} = K^{(eq)}$, the mixed mode equivalent stiffness K reduces to $K = K^{(eq)}$ according to Eq. (2.3.16).

Using the one-dimensional equivalent CZ law, an expression for the damage parameter can be obtained:

$$d = 1 - \frac{\bar{\sigma}}{K\lambda} \quad (2.3.17)$$

Provided that a function $\bar{\sigma}(\lambda)$ is known, Eq. (2.3.17) can be utilized to determine an expression for the damage evolution $d(\lambda)$ once the damage threshold value is exceeded, which is discussed later in Sec. 2.4.3.

2.3.3 Damage Model Reduction

Until now, the separation vector $\vec{\delta}$ has been described in spherical coordinates as: $\vec{\delta}(\phi(\varrho), \theta(\beta), \lambda)$, which is illustrated in the light grey box in Fig. 2.5a. This representation of $\vec{\delta}$ has the possibility of distinguishing between mode II and mode III properties. However, the current damage model reduces the three basic local displacement jump components into two; one associated with mode I crack opening δ_3 , and one associated with a combined shear mode δ_s . The shear norm δ_s is defined as a combination of the two shearing components in Eq. (2.3.3). With this reduction the shear-shear mode mixity ratio ϱ becomes redundant.

The energy dissipation associated with the combined shear mode G_s is defined as: $G_s = G_{II} + G_{III}$. It can be shown that under the assumption of equal elastic shear stiffnesses, $K_s = K_{11} = K_{22}$, a combined shear traction σ_s can be consequently defined as:

$$\sigma_s = \sqrt{\sigma_1^2 + \sigma_2^2} \quad (2.3.18)$$

The derivation process is omitted here, but is started by enforcing $\int_0^{\delta_s^{(t)}} \sigma_s d\delta_s = \sum_{i=1}^2 \int_0^{\delta_i^{(t)}} \sigma_i d\delta_i$, and using the definition of δ_s in Eq. (2.3.3), along with rules of integration by substitution and assuming equal elastic shear stiffnesses. Effectively, this implies that the critical energy dissipation for mode II and III must be equal, and the critical energy dissipation of the combined shear mode $G_{sc} = G_{IIc} = G_{IIIc}$ [Overgaard et al., 2010].

2.4 Mode Mixity Interaction

When modelling progressive delamination using CZ modelling, one needs to define a crack initiation criterion and a crack propagation criterion. The possibility of combining initiation and propagation characteristics is a key advantage of CZ modelling compared to e.g. linear elastic fracture mechanics which is only concerned with propagation while various strength theories as e.g. Tsai-Wu [Jones and Devens, 1998] or Puck [Lund and Overgaard, 2016] are only concerned with failure initiation.

Imagine a crack opening in pure mode I; under these circumstances, failure/damage initiation will simply occur when the traction exceeds the onset traction $\sigma_3^{(1)}$, since after this point irreversible material damage will occur. However, under mixed mode loading, mode interaction must be taken into account for determining delamination initiation. In these cases, onset of delamination can occur even if each traction component is less than its corresponding maximum strength $\sigma_I^{(1)}$, $\sigma_{II}^{(1)}$ and $\sigma_{III}^{(1)}$. This is evident by comparison of Ye's quadratic interaction criterion, as shown in Eq. (2.4.1), and the maximum traction criterion as illustrated in [Turon et al., 2006].

$$\left(\frac{\sigma_1}{\sigma_1^{(1)}}\right)^2 + \left(\frac{\sigma_2}{\sigma_2^{(1)}}\right)^2 + \left(\frac{\sigma_3}{\sigma_3^{(1)}}\right)^2 = 1 \quad (2.4.1)$$

In accordance, with Griffith's crack propagation criterion, delamination propagates when the energy release rate equals its critical value. This is straight forward in case of pure mode crack opening. However, in case of mixed mode crack opening it is necessary to implement mode interaction into the propagation criterion. Various criteria for prediction of delamination propagation under mixed mode crack opening has been proposed.

It is highlighted that there is not any universal criterion for accurately predicting these quantities. The criteria for prediction of delamination initiation and propagation depends on the material system at hand. However, for composites using an epoxy resin or thermoplastic PEEK resin, the BK propagation criterion [Benzeggagh and Kenane, 1995] is reported to agree well with experimental data [Camanho et al., 2003]. This criteria predicts the critical energy release rate G_c as follows:

$$G_c = G_c^I + (G_c^{II} - G_c^I) \left(\frac{G^{II}}{G^I + G^{II}}\right)^\eta \quad (2.4.2)$$

The ratio of shear energy release rate to the total energy release rate, is essential to this criterion. The constant η is determined from curve-fitting of material data. The original BK-criterion, as stated in [Benzeggagh and Kenane, 1995], is modified to include the energy release rate associated with mode III, as done in [Turon et al., 2006]. Hence the numerator is modified to: $G^s = G^{II} + G^{III}$. Additionally, a total energy release rate G^T is introduced as the total sum of energy release rates for all modes: $G^T = G^I + G^s$. The modified BK criterion then states:

$$G_c = G_c^I + (G_c^{II} - G_c^I) \left(\frac{G^s}{G^T}\right)^\eta \quad (2.4.3)$$

The ratio of energy release rates will be denoted as the B-parameter as shown in Eq. (2.4.4), and is considered in more detail in the following section.

$$B = \frac{G^s}{G^T} \quad (2.4.4)$$

2.4.1 B for Mixed Mode CZ Law

An expression for B is sought, to be able to determine a crack propagation criterion based on the BK-criterion for the cohesive zone model in a finite element context. This topic has been addressed in various references, e.g. [Turon et al., 2006], [Hansen and Lund, 2009] and [Sarrado et al., 2012], which is given a brief explanation here. Prior to this explanation, the J-integral will be considered, as it reveals a fundamental relation, which is essential to the understanding of the approach in [Turon et al., 2006]. The J-integral is a path independent integral given by Eq. (2.4.5) for a solid in static equilibrium, and is evaluated over a contour Γ as illustrated in Fig. 2.7a in case of plane problems. Additionally, the J-integral can be used to calculate the energy release rate G [Rice, 1968], [Andreassen, 2015]:

$$G = J = \int_{\Gamma} \left(\omega dx_2 - T_i \frac{\partial u_i}{\partial x_j} ds^{\Gamma} \right) \quad (2.4.5)$$

Wherein ω is the strain energy density, T_i is the traction vector defined according to the outward unit normal v_j^{Γ} along the integration path Γ , such that $T_i = \sigma_{ij} v_j^{\Gamma}$. By using the path independent property of the J-integral and evaluating it along a local integration path Γ_{CZ} that encloses the cohesive zone, as illustrated by Γ_{CZ} in Fig. 2.7a, it can be shown that [Hansen et al., 2009]:

$$J = \sum_{i=s,3} \int_0^{\delta_i^*} \sigma_i d\delta_i = W \quad (2.4.6)$$

Wherein δ_i^* denotes the end-opening separation, being the i'th separation component of the outermost point of the cohesive zone. The equation states that the J integral, and hence the energy release rate ($J=G$), can be calculated by the work of interfacial separations per unit area at the end opening point of the cohesive zone. Note that Eq. (2.4.6) transforms a contour integral into a sum of integrals evaluated for each separation component at the end-opening point.

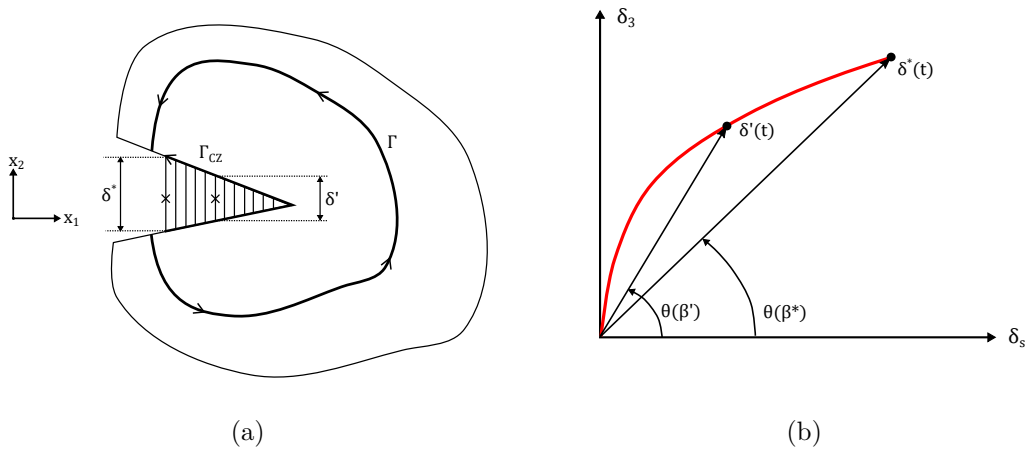


Figure 2.7: (a) An illustration of the integration path for the J-integral for a plane problem and a cohesive zone. (b) Concept of self-similar crack growth. δ^* represents the separation at the end opening, while δ' represents the separation at a point inside the cohesive zone.

A criterion for determining the critical fracture toughness under mixed mode loading is the modified BK-criterion (repeated here for convenience):

$$G_c = G_c^I + (G_c^s - G_c^I)B^\eta$$

$$B = \frac{G^s}{G^s + G^I}$$

The B parameter quantifies a ratio of decomposed energy release rates. The B-parameter can be expressed in terms of the work of interfacial separations at the end-opening according to Eq. (2.4.6). For instance, the energy release rate associated with the normal crack opening is computed as $G^I = \int_0^{\delta_3^*} \sigma_3 d\delta_3$.

$$B = \frac{G^s}{G^s + G^I} = \frac{W^s}{W^s + W^I} \Big|_{\text{for } \delta^*} \quad (2.4.7)$$

During the deformation process, the cohesive zone develops gradually and the B-parameter is varying with the interfacial separation as shown in e.g. [Turon et al., 2010] and [Hansen and Lund, 2009].

When using CZ interface elements, the B-parameter is computed locally at every integration point within the cohesive zone. Consequently, for some given time instant, the B-parameter is not necessarily the same at the end opening point and at an arbitrary point inside the cohesive zone, as illustrated by the two crosses in Fig. 2.7a. In LEFM-based techniques, the B definition is unique and serves as a global measure of mode mixity, as the crack tip is unambiguously defined in a confined small region. However, when using cohesive elements to simulate delamination, the B-parameter in Eq. (2.4.7) serves as an ‘‘averaged’’ mode mixity ratio of the fracture process zone as a whole [Sarrado et al., 2012], and is therefore not sufficient to be used at the level of element integration points.

This motivates the work of [Turon et al., 2006], which allows the mode mixity to vary through the fracture process zone, by calculating a B-parameter at every integration point in the cohesive zone at every time instant. Reconsidering the relation in Eq. (2.4.7), which is exact for the end-opening point δ^* , [Turon et al., 2006] assumes this relation holds for any point within the cohesive zone, such that:

$$B = \frac{G^s}{G^s + G^I} \approx \frac{W^s}{W^s + W^I} \Big|_{\text{for any } \delta'} \quad (2.4.8)$$

This mathematical approximation can in terms of physics be interpreted as assuming the crack to grow in a self-similar manner. The concept of self similar crack growth is illustrated in Fig. 2.7b, and basically means that, whatever history some point in the cohesive zone will experience, every other point in the cohesive zone will also experience.

Within this framework [Turon et al., 2006] develops a bilinear CZ law for simulation of delamination under variable mode. [Turon et al., 2006] derives an expression for B, under the assumption of equal elastic penalty stiffnesses in the three basic directions, which explicitly depends on the local mode mixity ratio β as given in Eq. (2.4.9). The B-parameter can be expressed in an alternative, but identical, form in terms of local separations components δ_3 and δ_s , which can be seen directly from the definition of β and δ_s in Eq. (2.3.5) and Eq. (2.3.3) respectively.

$$B = \frac{W^s}{W^s + W^I} = \frac{\beta^2}{1 + 2\beta^2 - 2\beta} = \frac{\delta_s^2}{\delta_s^2 + \delta_3^2} \quad (2.4.9)$$

This expression computes a ratio of energy release rates from instantaneous nodal displacements at every integration point inside the cohesive zone for every substep during the incremental Newton-Raphson based solution procedure. Due to the explicit dependence on β , this definition of the B-parameter is easily implemented in an interface element formulation. However, the expression is derived in preparation for a bilinear CZ law, which is not capable of simulating R-curve behavior as experienced in many composite laminates due to fiber-bridging.

In [Hansen and Lund, 2009], an equivalent one-dimensional trilinear CZ law is formulated as a simple approach to take multi-scale fracture mechanisms into consideration, i.e. mechanisms occurring at the crack tip (e.g. plasticity, viscoelastic deformation, matrix micro cracking) and at larger scales (e.g. fiber-bridging) can be modelled by the same CZ law. However, without reference to the specific shape (e.g. bilinear, trilinear or exponential) of the one-dimensional equivalent CZ law formulation, [Hansen and Lund, 2009] derives an expression for the B-parameter similar to the one shown in Eq. (2.4.9). The original expression for B in [Hansen and Lund, 2009] is derived using a different notation, as discussed previously, the damage kinematic description in [Hansen and Lund, 2009] is described in terms of trigonometric functions and mode mixity angles. Nevertheless, transforming the kinematic description to be consistent with the one used in this report, one arrives at an identical expression for B as given in Eq. (2.4.9) under the assumption of equal elastic penalty stiffnesses $K = K^{(eq)} = K_{11} = K_{22} = K_{33}$. Consequently, Eq. (2.4.9) also applies in case of a one-dimensional equivalent multilinear CZ law, which is also capable of modelling multi-scale fracture mechanisms. The critical energy release rate at some integration point in the cohesive zone with a given β , can thereby be estimated using the modified BK-criterion in Eq. (2.4.3) and the B-parameter in Eq. (2.4.9).

[Turon et al., 2006] and [Hansen and Lund, 2009] are examples of approaches wherein B can be estimated based on local and instantaneous measurements of mode mixity. Various other approaches for estimating the B-parameter are available in the literature. For instance, the commercial finite element code ABAQUS can use three measures of mode mixity in the cohesive interface element formulation, which in general can be quite different; two that are based on computing actual ratios of energy release rates (a) and (b) (without writing B explicitly in terms of nodal displacements) and one based on local interfacial tractions (c). Furthermore, the actual ratios of energy release rates can be based on the current state of deformation (a) (nonaccumulative measure of energy) or based on the history of deformation (b) (accumulative measure of energy) at an integration point [Abaqus].

A suitable measure of B is problem-dependent. Reconsidering the (a) and (b) options in ABAQUS, it is stated in the ABAQUS analysis reference [Abaqus], that a mode mixity B based on the instantaneous/current state of deformation is suited for mixed mode delamination simulations where the primary energy dissipation mechanism is associated with the creation of new surfaces due to failure in the cohesive zone (similar to cases where LEFM is adequate). On the other hand, a mode mixity ratio based on deformation history is suitable in situations where other significant dissipation mechanisms govern the overall structural response, e.g. fiber-bridging. Further guidelines are given in [Abaqus].

This suggests calculating B based on deformation history, when working with material systems where fiber-bridging is likely to occur. Under the assumption of self similar crack growth, the B-parameter can be computed according to Eq. (2.4.8) which is rewritten below in alternative but identical expression:

$$B = \frac{\sum_{i=1}^2 \left(\int_0^{\delta_i^{(t)}} \sigma_i d\delta_i \right)}{\sum_{i=1}^3 \left(\int_0^{\delta_i^{(t)}} \sigma_i d\delta_i \right)} \quad (2.4.10)$$

Instead of evaluating B instantaneously for a given β , the B-parameter is evaluated by pure mode integrals from (t=0) until the current time step (t) at every element integration point. Consequently, B in Eq. (2.4.10), is based on deformation history. In case of a multilinear CZ law, the integrals in Eq. (2.4.10) are evaluated exactly by applying a trapezoidal integration rule. Due to its ease of implementation and time limitations, B as given in Eq. (2.4.9) in terms of β is utilized in the following. However, one objective for further work is to evaluate B based on accumulative energy release rates, which could benefit when modelling fracture mechanisms including fiber-bridging [Abaqus].

In summary, the elastic stiffnesses are assumed to be equal for every direction $K^{(eq)} = K_{11} = K_{22} = K_{33}$. Consequently, the B-parameter can be expressed explicitly as a function of the normal-shear mode mixity ratio β as given in Eq. (2.4.9) for use in the BK-criterion. Additionally, the three basic separation components are collapsed into two: δ_3 and δ_s . Hence it is not possible to distinguish between mode II and mode III fracture properties. A combined shear traction component, σ_s , is defined as given is in Eq. (2.3.18), since the elastic shear stiffnesses are equal, $K_{11} = K_{22}$. This implies that the critical energy dissipation for mode II and mode III are assumed to be equal $G_{sc} = G_{IIc} = G_{IIIc}$.

2.4.2 Mixed Mode Interpolation of Multilinear CZ Laws

An n -segmented mixed mode multilinear CZ law contains a total of $2n$ model parameters to be determined: $\bar{\sigma}^{(i)}$ and $\bar{\delta}^{(i)}$ for $i = 1 \dots n$. Some of these parameters are fixed, e.g. the last traction point is identically zero $\bar{\sigma}^{(n)} = 0$, and some can be estimated directly from the experimental data, e.g. the final separation $\bar{\delta}^{(n)}$, which can be read from measurements of the separation at the initial crack tip. This is discussed further in Sec. 5.1. The remaining mixed mode CZ parameters needs to be related to pure mode material data through interpolation formulae. In this section, interpolation formulae for every discrete point $(\bar{\delta}^{(i)}; \bar{\sigma}^{(i)})$ of the one-dimensional equivalent traction-separation curve are defined. Traction $\bar{\sigma}^{(i)}$ are interpolated using a quadratic criterion similar to Ye's criterion in Eq. (2.4.1), but inspired by the BK-criterion. The interpolation of discrete separation points $\bar{\delta}^{(i)}$ are determined such that the critical energy release rate of the one-dimensional CZ law is energy consistent with the BK-criterion.

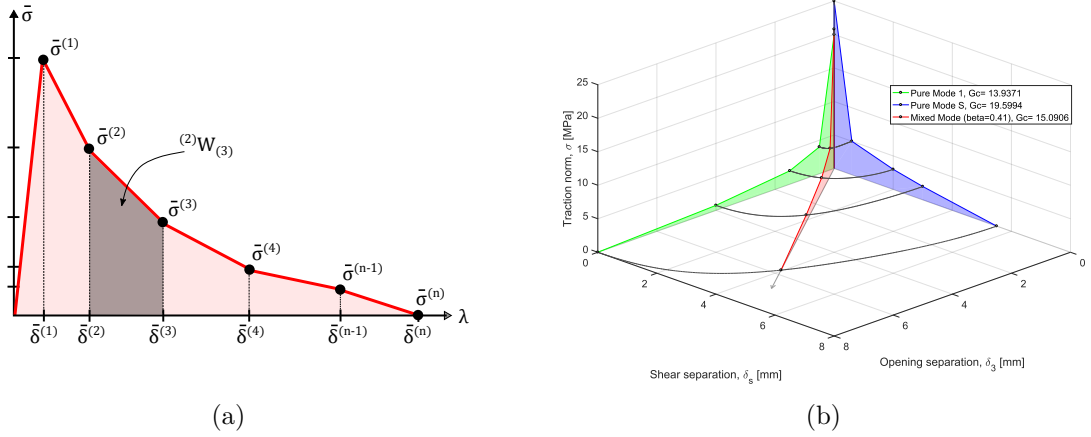


Figure 2.8: (a) Symbolic n -segmented mixed mode multilinear CZ law in $(\bar{\sigma}; \bar{\delta})$ -space. (b) Multilinear CZ laws and interpolation between pure mode material data.

In the absence of experimental data suggesting the effect of mode mixity on the onset traction $\bar{\sigma}^{(1)}$, [Turon et al., 2006] combines a quadratic interaction stress criterion, e.g. Ye's criterion in Eq. (2.4.1) and the idea of B from the BK-criterion to formulate a delamination initiation criterion as:

$$(\bar{\sigma}^{(1)})^2 = (\sigma_3^{(1)})^2 + \left[(\sigma_s^{(1)})^2 - (\sigma_3^{(1)})^2 \right] B^\eta \quad (2.4.11)$$

Where $\sigma_3^{(1)}$ and $\sigma_s^{(1)}$ represents the onset traction for the corresponding mode, and the $\bar{\sigma}^{(1)}$ represents the onset traction for the equivalent mixed mode CZ law, as illustrated in Fig. 2.8a. In this report, the criterion in Eq. (2.4.11) is modified. In case of no available experimental data, every discrete mixed mode equivalent tractions point $\bar{\sigma}^{(i)}$ is interpolated from pure mode material data I and s as follows:

$$(\bar{\sigma}^{(i)})^2 = (\sigma_3^{(i)})^2 + \left[(\sigma_s^{(i)})^2 - (\sigma_3^{(i)})^2 \right] B^\xi \quad (2.4.12)$$

The super index (i) denotes points in the traction-separation space as depicted in Fig. 2.8a. It is assumed that every discrete traction point in the equivalent mixed mode CZ law can be interpolated with the same curve fitting exponent ξ . Note the exponent ξ is different than the usual exponent η used for interpolation of energy release rates.

Given the equivalent mixed mode discrete traction points $\bar{\sigma}^{(i)}$ according to Eq. (2.4.12), the separations are considered next. The separations are determined such that the equivalent mixed mode CZ law is energy consistent with the BK-criterion. In order to determine separation points $\bar{\delta}^{(i)}$ from energy release rates, Eq. (2.4.5) and Eq. (2.4.6) are reconsidered. Under the assumption of self similar crack growth the energy release rate for any point inside the cohesive zone can be calculated by the work done by the interfacial separation at that specific point. In terms of the equivalent traction norm $\bar{\sigma}$ and the equivalent displacement jump norm λ , the total work of the separation per unit area is given in Eq. (2.4.13). This equation is rewritten as a sum of intervals for every two consecutive separation points $[\bar{\delta}^{(i-1)}; \bar{\delta}^{(i)}]$:

$$G_c = W = \int_0^{\bar{\delta}^{(n)}} \bar{\sigma}(\lambda) d\lambda = \int_0^{\bar{\delta}^{(1)}} \bar{\sigma}(\lambda) d\lambda + \sum_{i=1}^{(n-1)} \int_{\bar{\delta}^{(i)}}^{\bar{\delta}^{(i+1)}} \bar{\sigma}(\lambda) d\lambda \quad (2.4.13)$$

The integral for some interval $[\bar{\delta}^{(i-1)}; \bar{\delta}^{(i)}]$ in Eq. (2.4.13) will be denoted by ${}^{(i-1)}W_{(i)}$ as illustrated in Fig. 2.8a. Due to the piecewise line segmented shape of the CZ law, each of the integrals ${}^{(i-1)}W_{(i)}$ represents a trapezium. Therefore the integrals are exactly evaluated by use of a trapezoidal integration rule. The i 'th interval, the ${}^{(i-1)}W_{(i)}$ integral is computed as:

$${}^{(i-1)}W_i = \frac{1}{2}(\bar{\sigma}^{(i)} + \bar{\sigma}^{(i-1)})(\bar{\delta}^{(i)} - \bar{\delta}^{(i-1)}) \quad (2.4.14)$$

From here, an expression for the i 'th discrete separation point $\bar{\delta}^{(i)}$ can be derived:

$$\bar{\delta}^{(i)} = \bar{\delta}^{(i-1)} + \frac{2 {}^{(i-1)}W_i}{\bar{\sigma}^{(i)} + \bar{\sigma}^{(i-1)}} \quad (2.4.15)$$

It is assumed, that each interval of the work of separation per unit area ${}^{(i-1)}W_i$ (and thus the energy release rate) is interpolated using Eq. (2.4.16), which is based on the original BK-criterion for interpolating critical energy release rates, and here extended it to the W :

$${}^{(i-1)}W_i = {}^{(i-1)}W_i^I + \left({}^{(i-1)}W_i^s - {}^{(i-1)}W_i^I \right) B(\beta)^\eta \quad (2.4.16)$$

Where the mode mixity parameter B is calculated according to Eq. (2.4.9). Using Eq. (2.4.16) in Eq. (2.4.15), the discrete separation points of the mixed mode multilinear CZ law can be determined through interpolation of fracture energies. The combined expression is given in Eq. (2.4.17).

$$\bar{\delta}^{(i)} = \bar{\delta}^{(i-1)} + \frac{2 \left({}^{(i-1)}W_i^I + \left({}^{(i-1)}W_i^s - {}^{(i-1)}W_i^I \right) B(\beta)^\eta \right)}{\bar{\sigma}^{(i)} + \bar{\sigma}^{(i-1)}} \quad (2.4.17)$$

With this approach of determining each discrete separation point of the equivalent mixed mode multilinear CZ law, the critical energy release rate $G_c (= {}^0W_n)$ is consistent with the original BK-criterion. In summary, mixed mode equivalent tractions are interpolated from pure mode material data using a quadratic interaction criterion according to Eq. (2.4.12). Mixed mode separations are determined by assuming that each subinterval of the critical energy release rate, as discretized by a two consecutive separation points, can be interpolated using the BK-criterion. The interpolation of a mixed mode CZ law for a hypothetical material using these interpolation formulae are shown in Fig. 2.8b. The dark solid lines represent interpolation curves for discrete points $(\bar{\delta}^{(i)}; \bar{\sigma}^{(i)})$ for any mode mixity ratio β between 0 and 1.

2.4.3 Damage Evolution for Mixed Mode Multilinear CZ Law

In this section, an expression for the damage parameter for a mixed mode multilinear CZ law is derived. The evolution of the damage parameter is situation dependent. To completely define the damage evolution, one needs to define a damages threshold value and an expression for damage development as function of the equivalent displacement jump norm $d(\lambda)$.

Initially, an expression for $d(\lambda)$ is sought. For this purpose it is assumed that a point $(\lambda^{(t)}; \sigma^{(t)})$ lies on the multilinear CZ law, and hence not on the unloading/reloading secant stiffness lines. For a given mode mixity ratio β , an n-segmented mixed mode multilinear CZ law is shown in Fig. 2.9a. An arbitrary line segment of the multilinear CZ law is shown in Fig. 2.9b representing any of the (n-1) line segment of the softening part of the n line segmented CZ law.

Every line segment has a similar description and is completely defined by the coordinates of its end points. The line, ℓ , shown in Fig. 2.9b contains three points: $(\bar{\delta}^{(A)}; \bar{\sigma}^{(A)})$, $(\lambda; K(1-d)\lambda)$ and $(\bar{\delta}^{(B)}; \bar{\sigma}^{(B)})$. Using this notation, a general formula for the damage evolution along an arbitrary line segment of a mixed mode multilinear CZ law is derived.

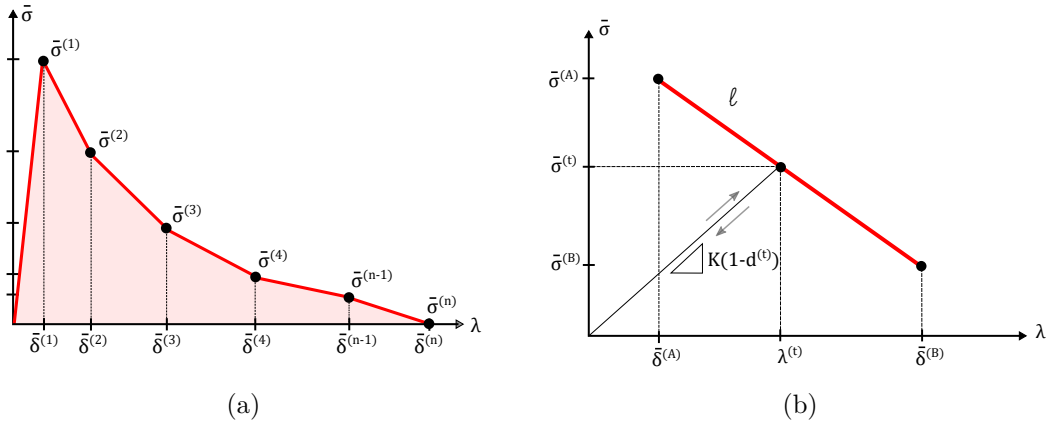


Figure 2.9: (a) A one-dimensional equivalent CZ law for a given mode mixity. (b) Line segment containing three points in separation-traction space.

Recalling the expression for determining the damage parameter of some mixed mode CZ law in Eq. (2.3.17), as repeated here for convenience, which applies in cases where the traction separation point lies on the mixed mode CZ law:

$$d(\lambda) = 1 - \frac{\bar{\sigma}(\lambda)}{K^{(eq)}\lambda} \quad (2.4.18)$$

To finalize the expression for d , the work conjugate traction norm must be determined as a function of the separation norm $\bar{\sigma}(\lambda)$. This is done by finding the parameters m and b describing the equation for the arbitrary line segment in Fig. 2.9b:

$$\bar{\sigma}(\lambda) = m\lambda + b$$

The parameters describing the line segment is readily found by using Fig. 2.9b and equations

for the slope of a line segment. Every intermediate step in the derivation is included.

$$\begin{aligned}
 m &= \frac{\bar{\sigma}^{(B)} - \bar{\sigma}^{(A)}}{\bar{\delta}^{(B)} - \bar{\delta}^{(A)}} \\
 \bar{\sigma}^{(B)} &= m\bar{\delta}^{(B)} + b \Leftrightarrow \\
 b &= \bar{\sigma}^{(B)} - m\bar{\delta}^{(B)} = \bar{\sigma}^{(B)} - \frac{\bar{\sigma}^{(B)} - \bar{\sigma}^{(A)}}{\bar{\delta}^{(B)} - \bar{\delta}^{(A)}}\bar{\delta}^{(B)} \Leftrightarrow \\
 b &= \frac{\bar{\sigma}^{(B)}(\bar{\delta}^{(B)} - \bar{\delta}^{(A)})}{\bar{\delta}^{(B)} - \bar{\delta}^{(A)}} - \frac{(\bar{\sigma}^{(B)} - \bar{\sigma}^{(A)})\bar{\delta}^{(B)}}{\bar{\delta}^{(B)} - \bar{\delta}^{(A)}} \Leftrightarrow \\
 b &= \frac{\bar{\sigma}^{(A)}\bar{\delta}^{(B)} - \bar{\sigma}^{(B)}\bar{\delta}^{(A)}}{\bar{\delta}^{(B)} - \bar{\delta}^{(A)}}
 \end{aligned}$$

Combining the expressions for m and b , the work conjugate traction norm is determined as function of the separation norm $\bar{\sigma}(\lambda)$:

$$\begin{aligned}
 \bar{\sigma}(\lambda) &= \left(\frac{\bar{\sigma}^{(B)} - \bar{\sigma}^{(A)}}{\bar{\delta}^{(B)} - \bar{\delta}^{(A)}} \right) \lambda + \left(\frac{\bar{\sigma}^{(A)}\bar{\delta}^{(B)} - \bar{\sigma}^{(B)}\bar{\delta}^{(A)}}{\bar{\delta}^{(B)} - \bar{\delta}^{(A)}} \right) \Leftrightarrow \\
 \bar{\sigma}(\lambda) &= \frac{\bar{\sigma}^{(B)}(\lambda - \bar{\delta}^{(A)}) + \bar{\sigma}^{(A)}(\bar{\delta}^{(B)} - \lambda)}{\bar{\delta}^{(B)} - \bar{\delta}^{(A)}} \tag{2.4.19}
 \end{aligned}$$

The expression for $\bar{\sigma}(\lambda)$ is substituted in Eq. (2.4.18) to have a final expression for the damage parameter:

$$\begin{aligned}
 d(\lambda) &= 1 - \frac{\bar{\sigma}(\lambda)}{K^{(eq)}\lambda} \Leftrightarrow \\
 d(\lambda) &= 1 - \frac{\bar{\sigma}^{(B)}(\lambda - \bar{\delta}^{(A)}) + \bar{\sigma}^{(A)}(\bar{\delta}^{(B)} - \lambda)}{K^{(eq)}\lambda(\bar{\delta}^{(B)} - \bar{\delta}^{(A)})} \Leftrightarrow \tag{2.4.20}
 \end{aligned}$$

The expression is rewritten and super indicies are introduced to represent the pseudo solution time. Additionally, it is highlighted that the damage parameter is confined to the range $[0;1]$.

$$d^{(t)}(\lambda) = 1 + \frac{\bar{\sigma}^{(B)}(\bar{\delta}^{(A)} - \lambda^{(t)}) + \bar{\sigma}^{(A)}(\lambda^{(t)} - \bar{\delta}^{(B)})}{K^{(eq)}\lambda^{(t)}(\bar{\delta}^{(B)} - \bar{\delta}^{(A)})}, \quad d \in [0;1] \tag{2.4.21}$$

It is highlighted that the expression only applies within the range: $\bar{\delta}^{(A)} \leq \lambda \leq \bar{\delta}^{(B)}$. Consequently when implementing the damage evolution law in an interface element for use in finite element analysis, appropriate book keeping should be done to control which line segment of the multilinear law is currently operating.

Having determined $d(\lambda)$, the definition of a damage threshold value is considered next. In order to track and ensure irreversible damage development, the element damage values are stored at each converged pseudo time increment (t). Thus, at any time instant, (t), the damage parameter at the previously converged time step ($t-1$) is known $d^{(t-1)}$. The damage parameter will only develop if the current value of λ is larger than a damage threshold value, r . The damage threshold value is defined in terms of the equivalent displacement jump norm and calculated from $d^{(t-1)}$. The damage parameter in Eq. (2.4.21) is given as function of λ , such that $d(\lambda)$. In order to calculate the threshold value, r , the inverse relation is needed $r^{(t)} = \lambda(d)|_{d=d^{(t-1)}}$.

$$r^{(t)} = \frac{\bar{\sigma}^{(A)}\bar{\delta}^{(B)} - \bar{\sigma}^{(B)}\bar{\delta}^{(A)}}{\bar{\sigma}^{(A)} - \bar{\sigma}^{(B)} + K^{(eq)}(1 - d^{Old})(\bar{\delta}^{(B)} - \bar{\delta}^{(A)})} \tag{2.4.22}$$

If $\lambda \leq r$ no damage will develop, meaning that $\dot{d} = 0$, hence D_{ij}^{tan} is defined in different expressions depending on the size of λ in relation to r . The damage parameter and threshold value are both internal state variables, they are further explored when the constitutive relation and the damage model are implemented in a the finite element code of the interface element.

2.5 Cont'd Constitutive Tangent Stiffness Tensor

In order to finalize the expression for the constitutive tangent stiffness tensor in Eq. (2.2.5) of Sec. 2.2.1, the time derivative of the damage parameter \dot{d} is needed. According to Eq. (2.4.21) d is a function of multiple variables: $d(\lambda, \bar{\sigma}^{(A)}, \bar{\sigma}^{(B)}, \bar{\delta}^{(A)}, \bar{\delta}^{(B)})$. In the general case, these variables depend on the mode mixity ratio which can be time dependent during the deformation process. Time derivatives of all these intermediate variables should be evaluated. However, it is assumed that the dependency on the mode mixity can be neglected during the incremental loading. This is also done in other references working with a bilinear CZ law, e.g. [Overgaard et al., 2010] and [Turon et al., 2006], which states that for real applications the rate of change of the mode mixity is sufficiently small to be neglected considering the pseudo time increment taken during the deformation process. The time derivative is then approximated by neglecting terms other than $\dot{\lambda}$.

$$\dot{d} = \frac{\partial d}{\partial \lambda} \frac{\partial \lambda}{\partial t} + \frac{\partial d}{\partial \bar{\sigma}^{(A)}} \frac{\partial \bar{\sigma}^{(A)}}{\partial t} + \frac{\partial d}{\partial \bar{\sigma}^{(B)}} \frac{\partial \bar{\sigma}^{(B)}}{\partial t} + \frac{\partial d}{\partial \bar{\delta}^{(A)}} \frac{\partial \bar{\delta}^{(A)}}{\partial t} + \frac{\partial d}{\partial \bar{\delta}^{(B)}} \frac{\partial \bar{\delta}^{(B)}}{\partial t} \approx \frac{\partial d}{\partial \lambda} \dot{\lambda} \quad (2.5.1)$$

Differentiating d in Eq. (2.4.21) wrt. λ the following is obtained³:

$$\begin{aligned} \frac{\partial d}{\partial \lambda} &= \frac{(\bar{\sigma}^{(A)} - \bar{\sigma}^{(B)})K^{(eq)}\lambda(\bar{\delta}^{(B)} - \bar{\delta}^{(A)}) - [\bar{\sigma}^{(A)}(\lambda - \bar{\delta}^{(A)}) + \bar{\sigma}^{(B)}(\bar{\delta}^{(A)} - \lambda)]K^{(eq)}(\bar{\delta}^{(B)} - \bar{\delta}^{(A)})}{[K^{(eq)}\lambda(\bar{\delta}^{(B)} - \bar{\delta}^{(A)})]^2} \Leftrightarrow \\ \frac{\partial d}{\partial \lambda} &= K^{(eq)}(\bar{\delta}^{(B)} - \bar{\delta}^{(A)}) \frac{(\bar{\delta}^{(A)} - \bar{\sigma}^{(B)})\lambda - [\bar{\sigma}^{(A)}(\lambda - \bar{\delta}^{(B)}) + \bar{\sigma}^{(B)}(\bar{\delta}^{(A)} - \lambda)]}{(K^{(eq)})^2 \lambda^2 (\bar{\delta}^{(B)} - \bar{\delta}^{(A)})^2} \Leftrightarrow \\ \frac{\partial d}{\partial \lambda} &= \frac{(\bar{\sigma}^{(A)} - \bar{\sigma}^{(B)})\lambda - [\bar{\sigma}^{(A)}\lambda - \bar{\sigma}^{(A)}\bar{\delta}^{(B)} + \bar{\sigma}^{(B)}\bar{\delta}^{(A)} - \bar{\sigma}^{(B)}\lambda]}{K^{(eq)}(\bar{\delta}^{(B)} - \bar{\delta}^{(A)})\lambda^2} \Leftrightarrow \\ \frac{\partial d}{\partial \lambda} &= \frac{(\bar{\sigma}^{(A)} - \bar{\sigma}^{(B)})\lambda - [(\bar{\sigma}^{(A)} - \bar{\sigma}^{(B)})\lambda - \bar{\sigma}^{(A)}\bar{\delta}^{(B)} + \bar{\sigma}^{(B)}\bar{\delta}^{(A)}]}{K^{(eq)}(\bar{\delta}^{(B)} - \bar{\delta}^{(A)})\lambda^2} \Leftrightarrow \end{aligned}$$

This expression reduces to the final expression for the derivative of the damage parameter with respect to the equivalent displacement jump norm λ :

$$\frac{\partial d}{\partial \lambda} = \frac{\bar{\sigma}^{(A)}\bar{\delta}^{(B)} - \bar{\sigma}^{(B)}\bar{\delta}^{(A)}}{K^{(eq)}(\bar{\delta}^{(B)} - \bar{\delta}^{(A)})\lambda^2} \quad (2.5.2)$$

To finalize the expression for \dot{d} an expression for $\dot{\lambda}$ should also be obtained. Note that there is the following relation between the separations defined as δ and as Δ : $\lambda = \sqrt{\delta_s^2 + \delta_3^2} = \sqrt{\Delta_1^2 + \Delta_2^2 + \langle \Delta_3 \rangle^2}$. This is done by using the chain rule and thus differentiating λ wrt. Δ_k from Eq. (2.3.4).

$$\begin{aligned} \dot{\lambda} &= \frac{\partial \lambda}{\partial \Delta_k} \dot{\Delta}_k \Leftrightarrow \\ \dot{\lambda} &= \frac{\Delta_k}{\lambda} \left[1 + \delta_{3k} \frac{\langle -\Delta_k \rangle}{\Delta_k} \right] \dot{\Delta}_k \end{aligned}$$

Please note that if the symbol δ includes two subindexes, as in the equation above δ_{3k} , it refers to the Kronecker's delta tensor. Combining the expressions for $\dot{\lambda}$ and $\partial d / \partial \lambda$ yields a final expression for the time derivative of the damage parameter:

$$\begin{aligned} \dot{d} &= \frac{\bar{\sigma}^{(A)}\bar{\delta}^{(B)} - \bar{\sigma}^{(B)}\bar{\delta}^{(A)}}{K^{(eq)}(\bar{\delta}^{(B)} - \bar{\delta}^{(A)})\lambda^3} \left[1 + \delta_{3k} \frac{\langle -\Delta_k \rangle}{\Delta_k} \right] \Delta_k \dot{\Delta}_k \Leftrightarrow \\ \dot{d} &= H^{(AB)} \left[1 + \delta_{3k} \frac{\langle -\Delta_k \rangle}{\Delta_k} \right] \Delta_k \dot{\Delta}_k \quad (2.5.3) \end{aligned}$$

³Derivative of a fraction: $(f/g)' = (f'g - fg')/g^2$

Wherein H is a scalar function of λ , given as follows:

$$H^{(AB)} = \frac{\bar{\sigma}^{(A)}\bar{\delta}^{(B)} - \bar{\sigma}^{(B)}\bar{\delta}^{(A)}}{K^{(eq)}(\bar{\delta}^{(B)} - \bar{\delta}^{(A)})\lambda^3} \quad \text{for } \bar{\delta}^{(A)} \leq \lambda \leq \bar{\delta}^{(B)} \quad (2.5.4)$$

Returning then to Eq. (2.2.5) which relates the rate of change of tractions $\partial\tau_i/\partial t$ to the rate of change of the separations $\partial\Delta_j/\partial t$, and is repeated here for convenience:

$$\dot{\tau}_i = \delta_{ij}K^{(eq)} \left[1 - d \left(1 + \delta_{3j} \frac{\langle -\Delta_j \rangle}{\Delta_j} \right) \right] \dot{\Delta}_j - \delta_{ij}K^{(eq)} \left[1 + \delta_{3j} \frac{\langle -\Delta_j \rangle}{\Delta_j} \right] \Delta_j \dot{d}$$

Substituting the expression for the time derivative of the damage parameter into this equation, a final expression that explicitly relates $\dot{\tau}_i$ and $\dot{\Delta}_j$ is obtained. Note that some subindexes are changed to make sure that the Newton's notation is consistent. The tangent stiffness tensor is identified such that: $\dot{\tau}_i = D_{ij}^{tan} \dot{\Delta}_j$.

$$D_{ij}^{tan} = \begin{cases} \delta_{ij}K^{(eq)} \left[1 - d \left(1 + \delta_{3j} \frac{\langle -\Delta_j \rangle}{\Delta_j} \right) \right] - K^{(eq)} \left[1 + \delta_{3i} \frac{\langle -\Delta_i \rangle}{\Delta_i} \right] \left[1 + \delta_{3j} \frac{\langle -\Delta_j \rangle}{\Delta_j} \right] H^{(AB)} \Delta_i \Delta_j & \text{for } \bar{\Delta}^A \leq \lambda \leq \bar{\Delta}^B \quad \text{and } \lambda > r \\ \delta_{ij}K^{(eq)} \left[1 - d \left(1 + \delta_{3j} \frac{\langle -\Delta_j \rangle}{\Delta_j} \right) \right] & \text{for } \lambda \leq r \end{cases} \quad (2.5.5)$$

The situation dependent behaviour of the tangent stiffness tensor is illustrated in Fig. 2.10. In case of $\lambda < r$, unloading or reloading occurs, and the tangent stiffness tensor is given by the second line of Eq. (2.5.5), which is illustrated as $D_{33}^{tan(2)}$ in Fig. 2.10. In case of damage development $\lambda > r$, the tangent stiffness tensor is given by the first line of Eq. (2.5.5), and is illustrated in the figure by $D_{ij}^{tan(1)}$.

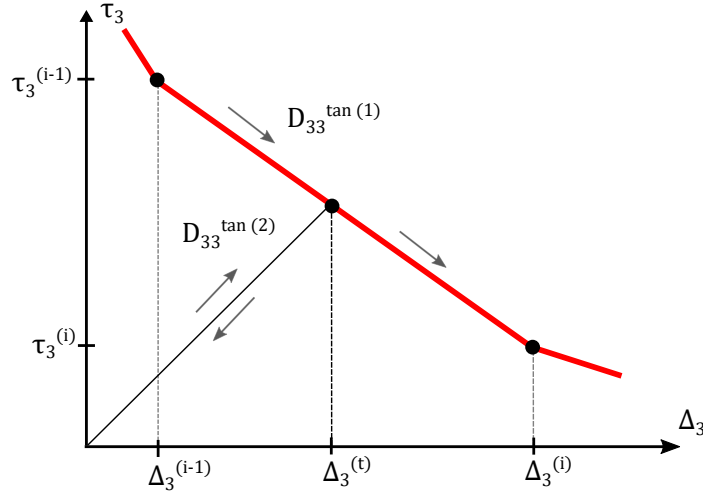


Figure 2.10: Illustration of the situation dependence of the tangent stiffness tensor. Here the tangent stiffness tensor is shown in mode I space, that is the third traction and separation components are considered.

Interface Element Formulation

3.1 Interface Element Formulation

Having introduced the boundary value problem and defined the interface kinematics together with a complete description of the interfacial constitutive law, the formulation of an interface finite element is examined in more detail. The interface element applied in this report, is an 8-noded, 3D, bilinear isoparametric solid element of zero thickness in the undeformed state. The interface element is shown in Fig. 3.1, in its undeformed and deformed configuration. The mechanics of the interface element is referred to its element midsurface \bar{S}^e .

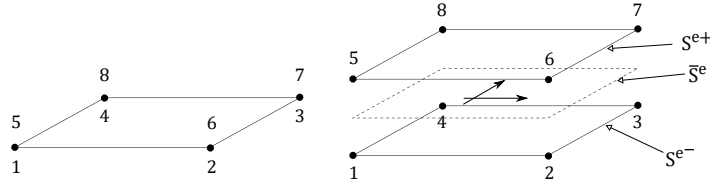


Figure 3.1: 8-noded, brick, isoparametric interface solid element.

The isoparametric formulation implies the introduction of an element natural coordinate system $(\xi; \eta)$, which maps the physical element into a reference element, that mathematically is a perfect square. With this definition, the element nodes are located at $(\xi; \eta) = (\pm 1; \pm 1)$. Additionally, per definition the element nodal coordinates, X_i , and nodal displacements, d_k , are interpolated using the same interpolation function matrix, denoted as $[N]$ [Cook et al., 2002]. Not to be confused with the multilinear CZ law to be implemented in the interface element, the isoparametric element is bilinear, meaning that the displacement field is interpolated bilinearly within the element from nodal displacements, as seen from the entries of the shape function matrix in Eq. (3.1.7).

$$N_1 = \frac{1}{4}(1 - \xi)(1 - \eta) \quad (3.1.1)$$

$$N_2 = \frac{1}{4}(1 + \xi)(1 - \eta) \quad (3.1.2)$$

$$N_3 = \frac{1}{4}(1 + \xi)(1 + \eta) \quad (3.1.3)$$

$$N_4 = \frac{1}{4}(1 - \xi)(1 + \eta) \quad (3.1.4)$$

$$[N]^+ = \begin{bmatrix} N_1 & 0 & 0 & \dots & N_4 & 0 & 0 \\ 0 & N_1 & 0 & \dots & 0 & N_4 & 0 \\ 0 & 0 & N_1 & \dots & 0 & 0 & N_4 \end{bmatrix} \quad (3.1.5)$$

$$[N]^- = -[N]^+ \quad (3.1.6)$$

$$[N] = [[N]^-, [N]^+] \quad (3.1.7)$$

The separation of the element surfaces S^{e+} and S^{e-} represents the opening of a crack, and is described by Eq. (3.1.8).

$$\vec{u}^+ - \vec{u}^- = [N]\vec{d} \quad (3.1.8)$$

Using the rotation tensor $[\Theta]$ from Eq. (2.1.18), the local displacement jump vector can be calculated as:

$$\vec{\Delta} = [\Theta][N]\vec{d} \quad (3.1.9)$$

3.1.1 Internal Force Vector and Element Stiffness Matrix

In order to derive an expression for the internal force vector and the element stiffness matrix, the principle of virtual work, as stated in Eq. (2.1.21), is reconsidered (switching the notation to matrix-vector notation, to be consistent with the current section). The internal virtual work associated with a single interface element, δW^{CZ_e} , is calculated as shown below, wherein \bar{S}^e represents the midsurface area of a single interface element in its deformed configuration.

$$\delta W^{CZ_e} = \int_{\bar{S}^e} \delta(\vec{u}^+ - \vec{u}^-)^T [\Theta]^T \vec{\tau} d\bar{S} \quad (3.1.10)$$

Insertion of the element kinematic relations of Eq. (3.1.8), the interfacial element internal virtual work becomes:

$$\delta W^{CZ_e} = \int_{\bar{S}^e} \delta \vec{d}^T [N]^T [\Theta]^T \vec{\tau} d\bar{S} \quad (3.1.11)$$

The variation of the nodal displacements is unaffected by the integration and can be taken outside the integral signs. From here, the internal force vector, \vec{r}^{int} , is identified, as the vector relating the virtual nodal displacement to the virtual internal work: $\delta W = \delta \vec{d}^T \vec{r}^{int}$. Performing these steps, the internal force vector for the interface element becomes:

$$\vec{r}^{int} = \int_{\bar{S}^e} [N]^T [\Theta]^T \vec{\tau} d\bar{S} \quad (3.1.12)$$

The integral is transformed to the natural coordinate system due to the isoparametric formulation of the interface element. This is done using the Jacobian matrix $[J]$, whose entries contain derivatives of the shape functions wrt. the natural coordinates, e.g. $N_{i,\xi}$. The specific expression for the Jacobian matrix is not of importance here, but can be found in references [Goyal, 2003] or [Overgaard et al., 2010]. The determinant of the Jacobian matrix is denoted, J , and represents an area scale factor relating a deformed midsurface infinitesimal area element, $d\bar{S}^e$, to an infinitesimal area element in the natural coordinate system $d\xi d\epsilon$. The transformation is given below:

$$\vec{r}^{int} = \int_{\bar{S}^e} [N]^T [\Theta]^T \vec{\tau} d\bar{S} = \int_{\xi} \int_{\eta} [N]^T [\Theta]^T \vec{\tau} J d\eta d\xi \quad (3.1.13)$$

In order to calculate the element tangent stiffness matrix $[k_T]$, the following relation needs to be established:

$$\delta \vec{r}^{int} = [k_T] \delta \vec{d} \quad (3.1.14)$$

Before establishing such a relation, it is highlighted, that displacement-controlled Newton-Raphson procedures are used for numerically solving the nonlinear FE analysis. In Newton-Raphson like methods, the internal force vector needs to be computed accurately, and the tangent stiffness matrix may be computed approximately. Keeping this in mind, the derivation of $[k_T]$ is continued.

Taking the first variation of the internal force vector yields the following:

$$\delta \vec{r}^{int} = \int_{\xi} \int_{\eta} ([N]^T [\Theta]^T \delta \vec{\tau} J + [N]^T \delta [\Theta]^T \vec{\tau} J + [N]^T [\Theta]^T \vec{\tau} \delta J) d\xi d\eta \quad (3.1.15)$$

Since the numerical integration of the element tangent stiffness matrix and the subsequential assembly of the global tangent stiffness matrix is computationally time consuming, only the first term in the first variation of the internal force vector is considered for approximating the element tangent stiffness matrix [Overgaard et al., 2010]. Consequently, changes in the rotation matrix, $\delta[\Theta]$, and changes in the deformed interface area, δJ , with respect to displacements are all omitted. However, the potential error due to changes in the interface area is regarded negligible, since the FE model uses an Updated Lagrangian formulation to account for geometrical nonlinearity, wherein the reference geometry is updated in each iteration of the substep in the Newton-Raphson solver used [Bak et al., 2014].

$$[k_T] \delta \vec{d} \approx \int_{\xi} \int_{\eta} [N]^T [\Theta]^T \delta \vec{\tau} J d\xi d\eta \quad (3.1.16)$$

Recalling the constitutive tangent stiffness $[D^{tan}]$, which relates variations in the CZ traction vector to variations in the local displacement jump vector: $\delta \vec{\tau} = [D^{tan}] \delta \vec{\Delta}$. This is substituted into the approximation of the element tangent stiffness tensor, and thereafter the kinematic relation in Eq. (3.1.9) is utilized:

$$\begin{aligned} [k_T] \delta \vec{d} &\approx \int_{\xi} \int_{\eta} [N]^T [\Theta]^T [D^{tan}] \delta \vec{\Delta} J d\xi d\eta \quad \Leftrightarrow \\ [k_T] \delta \vec{d} &\approx \int_{\xi} \int_{\eta} [N]^T [\Theta]^T [D^{tan}] [\Theta] [N] \delta \vec{d} J d\xi d\eta \quad \Leftrightarrow \\ [k_T] \delta \vec{d} &\approx \delta \vec{d} \int_{\xi} \int_{\eta} [N]^T [\Theta]^T [D^{tan}] [\Theta] [N] J d\xi d\eta \quad \Leftrightarrow \\ [k_T] &\approx \int_{\xi} \int_{\eta} [N]^T [\Theta]^T [D^{tan}] [\Theta] [N] J d\xi d\eta \quad (3.1.17) \end{aligned}$$

Having arrived at a result for the element tangent stiffness tensor, and element internal force vector for an interface element, the nonlinear FE analysis can readily be solved using Newton-Raphson solvers.

3.2 Programming of Interface Element Constitutive Relation

The programming and implementation of the constitutive relation and damage model for the interface finite element is presented in form of algorithms written in pseudo code. The algorithms are part of an element subroutine called `UserElem.f`. This is a user-defined element subroutine available through the commercial finite element program ANSYS MAPDL (v. 17.2). A complete user-defined interface element supporting a bilinear CZ law and capable of modelling mixed mode loading has been developed by the Department of Mechanical Engineering at Aalborg University, and has been available for the authors of this report since the beginning of the semester. `UserElem.f` includes a kinematic description, a constitutive relation, a damage model, element damage-dependent adaptive numerical integration schemes, formulation of an element stiffness matrix and internal force vector, and subroutines for post processing. Since the scope of this report is to formulate and implement a mixed mode multilinear CZ law, only the constitutive relations are considered here.

Fig. 3.2a through 3.2d are commonly referred to through the description. A multilinear CZ law is shown in Fig. 3.2a. The CZ law is discontinuous in terms of slopes and $\bar{\sigma}(\lambda)$ cannot be described by a single function, but a series of piecewise linear functions. Each line segment has a similar description and is completely defined by its two end points $(\bar{\delta}_{(i)} ; \bar{\sigma}_{(i)})$ and $(\bar{\delta}_{(i+1)} ; \bar{\sigma}_{(i+1)})$. The derivations of the constitutive tangent stiffness tensor and the damage parameter are kept in a general sense, making the expressions applicable for any line segment. The basic idea of the following implementation is to keep the formulae general for any line segment, as illustrated in Fig. 3.2c, and use counters (e.g. *intvalOld* and *intvalNew*) to identify the currently operating line segment function $\bar{\sigma}(\lambda)$.

Supporting Comments

Extra comments to the pseudo codes are given to guide the reader. Due to lack of space within a single page, the pseudo code is split into four algorithms: (1/4), (2/4), (3/4) and (4/4).

- The code is formulated such that the CZ law is defined in cases, controlled by a parameter n . n gives the total number of line segments involved in the multilinear CZ law. E.g. $n=2$ and $n=3$ represents a bilinear CZ law and trilinear CZ law, respectively. In case of $n=2$, the original bilinear CZ law is activated with no modifications done. However, the case of $n=3\dots 15$ are new, and describes a n -segmented multilinear CZ law.
- The subroutine is called `intMatDamage` as shown in the caption of the pseudo codes; its inputs are shown in round brackets $()$ and outputs as shown in the square brackets $[]$. The inputs to the subroutine are the damage parameter from the previously converged substep d^{Old} , the local displacement jump vector $\vec{\Delta}$, and an array *MatData* containing real constants defining the multilinear CZ law. The outputs of the subroutine are the damage parameter for the current substep d , a tangent and a secant stiffness matrix D_{tan} and D_{sec} respectively, critical energy dissipation G_c , the energy left to be dissipated before full damage G_{left} , and the normal-shear opening mode mixity ratio β .
- Algorithm (1/4) lines 2-8. From the separation vector $\vec{\Delta}$ are the combined shear norm δ_s , the equivalent separation norm λ and the mode mixity ratio β defined, for use in the damage model.

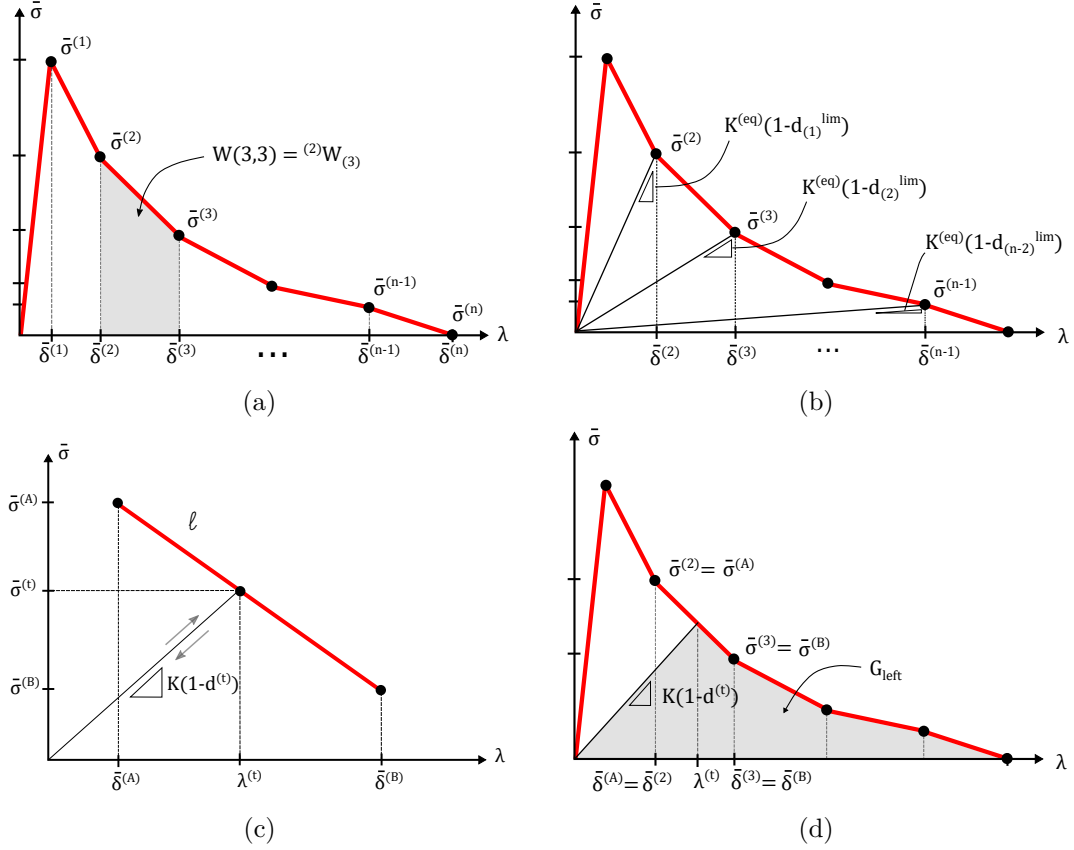


Figure 3.2: (a) n -degree multi linear cohesive law. (b) Illustrate concept of d_i^{lim} parameter. (c) Arbitrary line segment of multi linear law for a given separation range. (d) The fracture energy left for a given separation.

- Algorithm (2/4) lines 12-25. CZ laws for pure mode I and pure shear mode s are stored in the `MatData()` array. The pure mode separation $\delta_{3,s}^{(i)}$ and traction $\sigma_{3,s}^{(i)}$ values are assembled into arrays `delta()` and `sigma()`, respectively. An array `W` of the fracture energy associated with each interval of two consecutive separation points is also defined.

`W` has dimensions $(n \times 3)$; one row for each trapezium of the multilinear and a column for mode I, mode s and the equivalent mixed mode CZ law. Fig. 3.2a illustrates the equivalent mixed mode CZ law, hence the fracture energy of each interval is written in the third column of `W`. The energy associated with the specific interval $[\bar{\delta}^{(2)}; \bar{\delta}^{(3)}]$ is denoted ${}^{(2)}W_{(3)}$ and is stored in the third row of `W`. Thus, the grey trapezium illustrated in Fig. 3.2a represents $W(3,3)$.

These division of the total fracture energy into separate intervals is a necessity due to the interpolation functions chosen and to conveniently calculate G_{left} as will be seen.

- Algorithm (1/4) lines 27-37. The equivalent mixed mode CZ law is established using the interpolation formulae given in Sec. 2.4.2. The discrete separation and traction points of the mixed mode CZ law are stored in `deltaBar` and `sigmaBar`, respectively.
- Algorithm (2/4) lines 6-24. To take the irreversibility of the damage parameter into account, the damage values are stored at the element integration points at each converged substep. The damage parameter at the previously converged substep is denoted: d^{Old} . Based on d^{Old} , a damage threshold value, r , is calculated according to Eq. (2.4.22). Only if $\lambda > r$, damage development will occur. At a given substep, the location on

the multilinear CZ law is yet unknown. In order to calculate r , the line segment corresponding to d^{Old} must be identified, such that (A) and (B) parameters in Eq. (2.4.22) can be determined. The line segment corresponding to d^{Old} is identified by comparing relative sizes of d^{Old} and a parameter denoted $d_{(i)}^{\text{lim}}$. Damage limiting values $d_{(i)}^{\text{lim}}$ are formulated from values in `deltaBar()` and `sigmaBar()`, and are shown in Fig. 3.2b. E.g. $\bar{\sigma}^{(2)} = K^{(eq)}(1 - d_1^{\text{lim}})\bar{\delta}^{(2)} \Leftrightarrow d_1^{\text{lim}} = 1 - \bar{\sigma}^{(2)}/K^{(eq)}\bar{\delta}^{(2)}$. Note, the first damage limiting value $d_{(1)}^{\text{lim}}$ is associated with the second traction/separation values ($\bar{\delta}^{(2)}$; $\bar{\sigma}^{(2)}$). A scalar `intvalOld` is used to locate the line segment corresponding to d^{Old} .

- Algorithm (3/4). If λ is greater than the damage threshold value, $\lambda > r$, damage will develop, and the damage parameter d should be updated. Now, the line segment corresponding to the current value of λ should be identified. This is done by comparing relative sizes of λ with the discrete separation points, of the multilinear CZ law, stored in `deltaBar()`. Based on the comparison, a scalar `intvalNew` is defined such that (A) and (B) parameters, as illustrated in Fig. 3.2c, for the corresponding line segment can be determined. The damage parameter is calculated according to Eq. (2.4.21). Eventually, a H scalar is calculated for use in the expression for the tangent stiffness tensor D_{ij}^{tan} which is denoted as K_{tan} in the pseudo code. If the current value of λ is less than the threshold value, the damage parameter $d = d^{\text{Old}}$.

- Algorithm (3/4) lines 24-36. The procedure to calculate the energy left to be dissipated G_{left} is illustrated in Fig. 3.2d. At a given time instant, $\lambda^{(t)}$ is located between $\bar{\delta}^{(2)}$ and $\bar{\delta}^{(3)}$ as shown in the figure. G_{left} is shown as grey and is split into multiple separate geometries; a triangle $(0 ; 0)$, $(\lambda^t ; K(1 - d^t)\lambda^t)$, $(\lambda^t ; 0)$, a trapezium $(\lambda^t ; 0)$, $(\lambda^t ; K(1 - d^t)\lambda^t)$, $(\bar{\Delta}^{(3)} ; \bar{\tau}^{(3)})$ and $(\bar{\Delta}^{(3)} ; 0)$, and the usual trapeziums stored in the third column of W . Area formulae for these geometries are then used to obtain G_{left} . The fracture energies associated with the remaining trapeziums are calculated by summing appropriate entries in W :

$$G_{\text{left}} = \frac{1}{2}K^{(eq)}(1 - d)\lambda^2 + \frac{1}{2}[K^{(eq)}(1 - d)\lambda + \bar{\sigma}^{(B)}][\bar{\delta}^{(B)} - \lambda] + \sum_{i=\text{intvalNew}+2}^n W(i, 3)$$

A special case is set up when λ is located in the range $\bar{\delta}^{(n-1)}$; $\bar{\delta}^{(n)}$, such that `intvalNew` = $n - 1$, in which case there are no remaining trapeziums to be summed.

- Algorithm (4/4). Secant and tangent element stiffness matrices are calculated.

(1/4) subroutine [d, D_{\tan} , D_{\sec} , $K^{(eq)}$, G_c , G_{left} , β] = intMatDamage(d^{Old} , $\vec{\Delta}$, MatData)

1: **select case(n)**
 2: **Damage Kinematic Relations**
 3: Norms δ_s and λ are calculated according to Eq. (2.3.3) and Eq. (2.3.4) respectively:
 4: $\delta_s = \sqrt{\Delta_1^2 + \Delta_2^2}$
 5: $\lambda = \sqrt{\delta_s^2 + \langle \Delta_3 \rangle^2}$
 6: The normal-shear opening mode mixity ratio β is calculated according to Eq. (2.3.5), and the $B(\beta)$ parameter is calculated according to Eq. (2.4.9):
 7: $\beta = \frac{\delta_s}{\delta_s + \langle \Delta_3 \rangle}$
 8: $B(\beta) = \frac{\beta^2}{1 + 2\beta^2 - 2\beta}$
 9: **case(2)**
 10: ...
 11: **case(3, 4, 5, 6, 7, 8, 9, 10, 11, 12, 13, 14, 15)**
 12: **Pure Mode Material Data**
 13: Pure mode I and shear mode s CZ laws are described by traction and separation arrays delta() and sigma() respectively, which are defined from real constants stored in an array called MatData().
 14: delta(:)=zeros(n,2); sigma(:)=zeros(n,2)
 15:
$$\text{delta} = \begin{bmatrix} \delta_3^{(1)} & \delta_3^{(2)} & \dots & \delta_3^{(n-1)} & \delta_3^{(n)} \\ \delta_s^{(1)} & \delta_s^{(2)} & \dots & \delta_s^{(n-1)} & \delta_s^{(n)} \end{bmatrix}^T \quad \text{sigma} = \begin{bmatrix} \sigma_3^{(1)} & \sigma_3^{(2)} & \dots & \sigma_3^{(n-1)} & \sigma_3^{(n)} \\ \sigma_s^{(1)} & \sigma_s^{(2)} & \dots & \sigma_s^{(n-1)} & \sigma_s^{(n)} \end{bmatrix}^T$$

 16: The fracture energies for an interval of two consecutive separation points [$\delta^{(j-1)}$; $\delta^{(j)}$] are calculated for mode I ${}^{(j-1)}W_j^I$, shear mode ${}^{(j-1)}W_j^s$, and the equivalent mixed mode ${}^{(j-1)}\bar{W}_j$. This is calculated for every n-interval and stored in an array $W()$, whose first, second, and third column are associated with mode I, mode s, and the equivalent mixed mode CZ law, respectively. Thus, the j'th row of $W()$ becomes $W(j, :) = [{}^{(j-1)}W_j^I \quad {}^{(j-1)}W_j^s \quad {}^{(j-1)}\bar{W}_j]$.
 17: $W(:)=zeros(n,3)$; $\text{sigmaBar}(:) = zeros(n,1)$; $\text{deltaBar}(:) = zeros(n,1)$
 18: **for jj=1:n do**
 19: **for kk=1:2 do**
 20: **if jj=1 then**
 21: $W(\text{jj},\text{kk})=0.5 * \text{sigma}(\text{jj},\text{kk}) * \text{delta}(\text{jj},\text{kk})$
 22: **else**
 23: $W(\text{jj},\text{kk})=0.5 * (\text{sigma}(\text{jj}-1,\text{kk}) + \text{sigma}(\text{jj},\text{kk})) * (\text{delta}(\text{jj},\text{kk}) - \text{delta}(\text{jj}-1,\text{kk}))$
 24: **end if**
 25: **end for**
 26:
 27: **Equivalent Mixed Mode CZ Law**
 28: A mixed mode equivalent CZ law is calculated. Each component $\bar{\delta}^{(i)}$ and $\bar{\sigma}^{(i)}$ are calculated according to Eq. (2.4.17) and Eq. (2.4.12) and stored in arrays deltaBar(i) and sigmaBar(i) respectively.
 29: $\text{sigmaBar}(\text{jj}) = \sqrt{\text{sigma}(\text{jj},1)^2 + (\text{sigma}(\text{jj},2)^2 - \text{sigma}(\text{jj},1)^2) * B(\beta)^\xi}$
 30: **if jj=1 then**
 31: $\text{deltaBar}(\text{jj}) = \frac{2(W(\text{jj},1)+W(\text{jj},2)-W(\text{jj},1))*B(\beta)^\xi}{\text{sigmaBar}(\text{jj})}$
 32: $W(\text{jj},3) = 0.5 * \text{sigmaBar}(\text{jj}) * \text{deltaBar}(\text{jj})$
 33: **else**
 34: $\text{deltaBar}(\text{jj}) = \text{deltaBar}(\text{jj}-1) + \frac{2(W(\text{jj},1)+W(\text{jj},2)-W(\text{jj},1))*B(\beta)^\xi}{\text{sigmaBar}(\text{jj})+\text{sigmaBar}(\text{jj}-1)}$
 35: $W(\text{jj},3) = 0.5 * (\text{sigmaBar}(\text{jj}) + \text{sigmaBar}(\text{jj}-1)) * (\text{deltaBar}(\text{jj}) - \text{deltaBar}(\text{jj}-1))$
 36: **end if**
 37: **end for**

(2/4) subroutine [d, D_{\tan} , D_{\sec} , $K^{(eq)}$, G_c , G_{left} , β] = intMatDamage(d^{Old} , $\vec{\Delta}$, MatData)

1: The elastic penalty stiffness parameter is calculated as:

2: $K^{(eq)} = \frac{\text{sigmaBar}(1)}{\text{deltaBar}(1)}$

3: The total energy dissipation G_c of the equivalent mixed mode CZ law is calculated as the sum of all components of the third column of W.

4: $G_c = \sum_{jj=1}^n W(jj, 3)$

5:

6: **Damage Threshold Value**

7: Consider Fig. 3.2b, the d_i^{lim} expressions can be derived directly from values in arrays deltaBar() and sigmaBar(). E.g. $\bar{\sigma}^{(2)} = K^{(eq)}(1 - d_1^{\text{lim}})\bar{\delta}^{(2)} \Leftrightarrow d_1^{\text{lim}} = 1 - \bar{\sigma}^{(2)}/K^{(eq)}\bar{\delta}^{(2)}$. The scalar *intvalOld* identifies the linesegment of the multilinear CZ law which corresponds to d^{Old} .

8: *intvalOld* = 0

9: $d^{\text{lim}}(:) = \text{zeros}(n-2, 1)$

10: **for** jj=1:n-2 **do**

11: $d^{\text{lim}}(jj) = 1 - \frac{\text{sigmaBar}(jj+1)}{K\text{deltaBar}(jj+1)}$

12: **if** $d^{\text{Old}} > d^{\text{lim}}(jj)$ **then**

13: *intvalOld* = jj

14: **else**

15: **exit** for loop

16: **end if**

17: **end for**

18:

19: A damage threshold value, r, is calculated based on d^{Old} according to Eq. (2.4.22). The (A), (B) parameters are shown in Fig. 3.2c and identified using *intvalOld*.

20: $\bar{\delta}^{(A)} = \text{deltaBar}(\text{intvalOld} + 1)$

21: $\bar{\delta}^{(B)} = \text{deltaBar}(\text{intvalOld} + 2)$

22: $\bar{\sigma}^{(A)} = \text{sigmaBar}(\text{intvalOld} + 1)$

23: $\bar{\sigma}^{(B)} = \text{sigmaBar}(\text{intvalOld} + 2)$

24: $r = \frac{\bar{\sigma}^{(A)}\bar{\delta}^{(B)} - \bar{\sigma}^{(B)}\bar{\delta}^{(A)}}{\bar{\sigma}^{(A)} - \bar{\sigma}^{(B)} + K^{(eq)}(1 - d^{\text{Old}})(\bar{\delta}^{(B)} - \bar{\delta}^{(A)})}$

(3/4) subroutine $[d, D_{\tan}, D_{\sec}, K^{(eq)}, G_c, G_{\text{left}}, \beta] = \text{intMatDamage}(d^{\text{Old}}, \vec{\Delta}, \text{MatData})$

- 1: **Determine d, H, Gleft**
- 2: **if** $\lambda > r$ **then**
- 3: Damage develops. The current range for λ is determined using *intvalNew* and parameters for the corresponding line segment are identified.
- 4: *intvalNew* = 0
- 5: **for** $jj=1:n-1$ **do**
- 6: **if** $\lambda > \text{deltaBar}(jj)$ **then**
- 7: *intvalNew* = jj
- 8: **else**
- 9: **exit** for loop
- 10: **end if**
- 11: **end for**
- 12: The $\bar{\sigma}^{(A)}$, $\bar{\sigma}^{(B)}$, $\bar{\delta}^{(A)}$ and $\bar{\delta}^{(B)}$ parameters are updated and the damage parameter is calculated. Note since this update only happens if $\lambda > r$, the scalar *intvalNew* will always be greater than zero (since initially $r = \bar{\delta}^{(1)}$).
- 13: $\bar{\delta}^{(A)} = \text{deltaBar}(\text{intvalNew})$
- 14: $\bar{\delta}^{(B)} = \text{deltaBar}(\text{intvalNew} + 1)$
- 15: $\bar{\sigma}^{(A)} = \text{sigmaBar}(\text{intvalNew})$
- 16: $\bar{\sigma}^{(B)} = \text{sigmaBar}(\text{intvalNew} + 1)$
- 17: Using Eq. (2.4.21) to calculate damage parameter:
- 18:
$$d = 1 + \frac{\bar{\sigma}^{(A)}(\lambda - \bar{\delta}^{(B)}) + \bar{\sigma}^{(B)}(\bar{\delta}^{(A)} - \lambda)}{K^{(eq)}\lambda(\bar{\delta}^{(B)} - \bar{\delta}^{(A)})}$$
- 19: **if** $d > 1$ **then**
- 20: $d = 1$
- 21: **end if**
- 22:
- 23: The energy left to be dissipated is calculated. See the supporting comments for further information.
- 24: $G_{\text{left}} = \frac{1}{2}K^{(eq)}(1 - d)\lambda^2 + \frac{1}{2}(K^{(eq)}(1 - d)\lambda + \bar{\sigma}^{(B)})(\bar{\delta}^{(B)} - \lambda)$
- 25: **if** (*intvalNew* < $n-1$) **then**
- 26: $G_{\text{left}} = G_{\text{left}} + \sum_{jj=\text{intvalNew}+2}^n W(jj, 3)$
- 27: **end if**
- 28: **else**
- 29: No damage development occurs and the parameters: $\bar{\sigma}^{(A)}$, $\bar{\sigma}^{(B)}$, $\bar{\delta}^{(A)}$ and $\bar{\delta}^{(B)}$ determined in lines 20-23 (2/4) are reused.
- 30: $d = d^{\text{Old}}$
- 31: $G_{\text{left}} = \frac{1}{2}K^{(eq)}(1 - d)r^2 + \frac{1}{2}(K(1 - d)r + \bar{\sigma}^{(B)})(\bar{\delta}^{(B)} - r)$
- 32: **if** *intvalOld* < $n-2$ **then**
- 33: $G_{\text{left}} = G_{\text{left}} + \sum_{jj=\text{intvalOld}+3}^n W(jj, 3)$
- 34: **end if**
- 35: **end if**
- 36:
- 37: Calculating the H scalar according to Eq. (2.5.4):
- 38:
$$H = \frac{\bar{\sigma}^{(A)}\bar{\delta}^{(B)} - \bar{\sigma}^{(B)}\bar{\delta}^{(A)}}{K^{(eq)}(\bar{\delta}^{(B)} - \bar{\delta}^{(A)})\lambda^3}$$
- 39:
- 40: **end select**

(4/4) subroutine $[d, D_{\text{tan}}, D_{\text{sec}}, K^{(eq)}, G_c, G_{\text{left}}, \beta] = \text{intMatDamage}(d^{\text{Old}}, \vec{\Delta}, \text{MatData})$

1: $[D_{\text{sec}}] = K^{(eq)}(1 - d)[I]$
2: This if statement includes the effect of the MacAuley bracket implemented in Eq. (2.5.5).

3: **if** $\Delta_3 < 0$ **then**
4: $D_{\text{sec}}(3, 3) = D_{\text{sec}}(3, 3) + dK^{(eq)}$
5: **end if**
6: $[D_{\text{tan}}] = [D_{\text{sec}}]$
7: **if ... then**
8: A statement for determining curve-location in the $(\bar{\delta}, \bar{\sigma})$ -space. The location is specified in the 'stiffChoice' variable. Note in case stiffChoice = 0, the scalar H is unused.
9: stiffChoice = 1: Associated with damage development
10: stiffChoice = 0: Associated with unloading
11: **end if**
12: The expressions for the constitutive tangent stiffness matrix are obtained from Eq. (2.5.5)

13: **if** stiffChoice = 1 **then**
14: $D_{\text{tan}}(1, 1) = D_{\text{tan}}(1, 1) - K^{(eq)}H\Delta_1\Delta_1$
15: $D_{\text{tan}}(1, 2) = D_{\text{tan}}(1, 2) - K^{(eq)}H\Delta_1\Delta_2$
16: $D_{\text{tan}}(2, 1) = D_{\text{tan}}(2, 1) - K^{(eq)}H\Delta_2\Delta_1$
17: $D_{\text{tan}}(2, 2) = D_{\text{tan}}(2, 2) - K^{(eq)}H\Delta_2\Delta_2$
18: **if** $\Delta_3 > 0$ **then**
19: $D_{\text{tan}}(1, 3) = D_{\text{tan}}(1, 3) - K^{(eq)}H\Delta_1\Delta_3$
20: $D_{\text{tan}}(3, 1) = D_{\text{tan}}(3, 1) - K^{(eq)}H\Delta_3\Delta_1$
21: $D_{\text{tan}}(2, 3) = D_{\text{tan}}(2, 3) - K^{(eq)}H\Delta_2\Delta_3$
22: $D_{\text{tan}}(3, 2) = D_{\text{tan}}(3, 2) - K^{(eq)}H\Delta_3\Delta_2$
23: $D_{\text{tan}}(3, 3) = D_{\text{tan}}(3, 3) - K^{(eq)}H\Delta_3\Delta_3$
24: **end if**
25: **end if**
26: **return**

3.3 Verifying Implementation

In order to validate the implementation of the constitutive relations and the damage model, a finite element model consisting of a single interface element has been built. The interface element is given a set of prescribed displacements UX , UY , UZ which directly corresponds to local separations Δ_i of the interface element. The resulting stress-displacement curves should give an exact replica of the intended CZ law for the element subroutine to be implemented correctly.

An illustration of the finite element model is shown in Fig. 3.3a. In the undeformed configuration, the interface element has zero thickness. The bottom surface has all d.o.f. prescribed as zero, i.e. $UX=UY=UZ=0$, while the top surface is displaced by an amount δ . Keeping displacement components $UX=UZ=0$ and varying UY corresponds to pure mode I opening of the interface element. Verification of mixed mode loading is considered in Sec. 3.3.2.

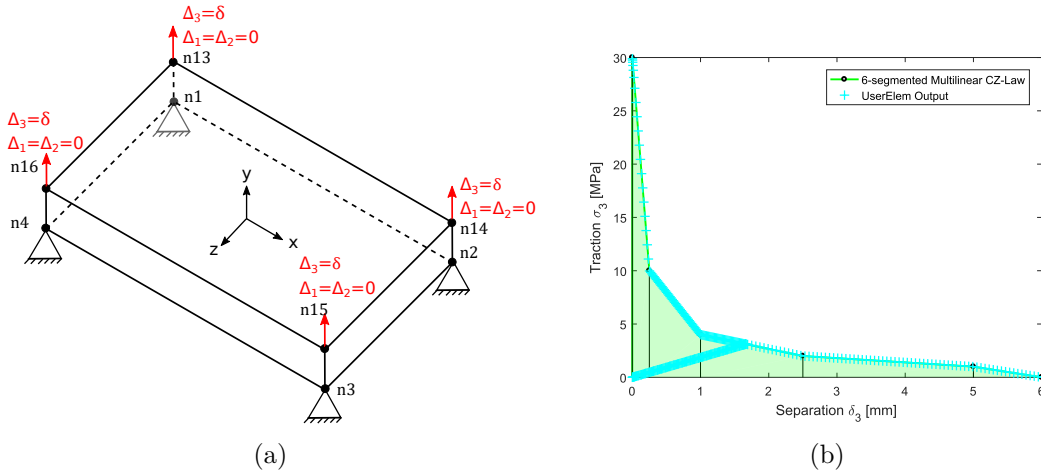


Figure 3.3: (a) FE model for verification test. (b) Pure mode I loading - reloading sequence.

The material type is not of importance for this verification example, hence a hypothetical CZ law is utilized, as shown by the green curve of Fig. 3.3b. Nodal separations Δ_i and tractions τ_i for the user-defined interface element are stored in stress/strain post-processing fields according to Tab. 3.1 as described in [Christensen et al., 2013]. The Y-component of stress S,Y and elastic strain $EPEL,Y$ corresponds to the cohesive traction-separation curve for mode I crack opening. Monitoring these parameters and plotting S,Y versus $EPEL,Y$ should result in a curve following the intended CZ-law for the implementation to be correct. In Fig. 3.3b the results from a pure mode I test for loading/unloading/reloading is shown by the light blue crosses “+”. The prescribed displacement δ is loaded from $UY=0$ mm to $UY=1.67$ mm, then unloaded from $UY=1.67$ mm to $UY=0$ mm, and at last reloaded from $UY=0$ mm to $UY=6.0$ mm (being equal to the final separation in the CZ law). The multilinear CZ law implementation works as intended, since the output of the UserElem subroutine lies on top of the CZ law. The linear unloading/reloading and damage threshold implementation also work properly, as seen by the data points following a line of secant stiffness, $K(1 - d)$, when unloading/reloading between $UY=1.67$ mm and $UY=0$ mm.

3.3.1 Sensitivity Study

Considering the same FE model, the same loading/unloading/reloading sequence, but different shapes of the multilinear CZ law. Three different CZ law shapes are examined in more detail as shown in Fig. 3.4a through 3.4c.

UserElem Quantity	ANSYS	APDL Command
Δ_3	Elastic strain in y-direction	NSOL,EPEL,Y
Δ_1	Elastic strain in xy-direction	NSOL,EPEL,XY
Δ_2	Elastic strain in yz-direction	NSOL,EPEL,YZ
τ_3	Stress in y-direction	NSOL,S,Y
τ_1	Stress in xy-direction	NSOL,S,XY
τ_2	Stress in yz-direction	NSOL,S,YZ

Table 3.1: Relations between UserElem outputs and APDL commands.

In Fig. 3.4a and 3.4b, it is seen that there is no problem in handling horizontal and vertical line segments, nor a problem in handling line segments of positive slope, as long as the changes in slope happens gradually.

However, in case of sudden changes, as shown in Fig. 3.4c, problems may arise. The problem in Fig. 3.4c is explained in greater detail in Fig. 3.4d, and arises in the case of unloading/reloading. At the time instant when unloading starts, $\delta_3 = 1.67\text{mm}$, some energy has been dissipated. However, during the unloading, the load path follows arrows shown, resulting in restoration of dissipated energy, which is indeed thermodynamically inconsistent. Nevertheless, in the following, the CZ law is assumed to be monotonically decreasing, hence no problems as shown in Fig. 3.4c will ever occur.

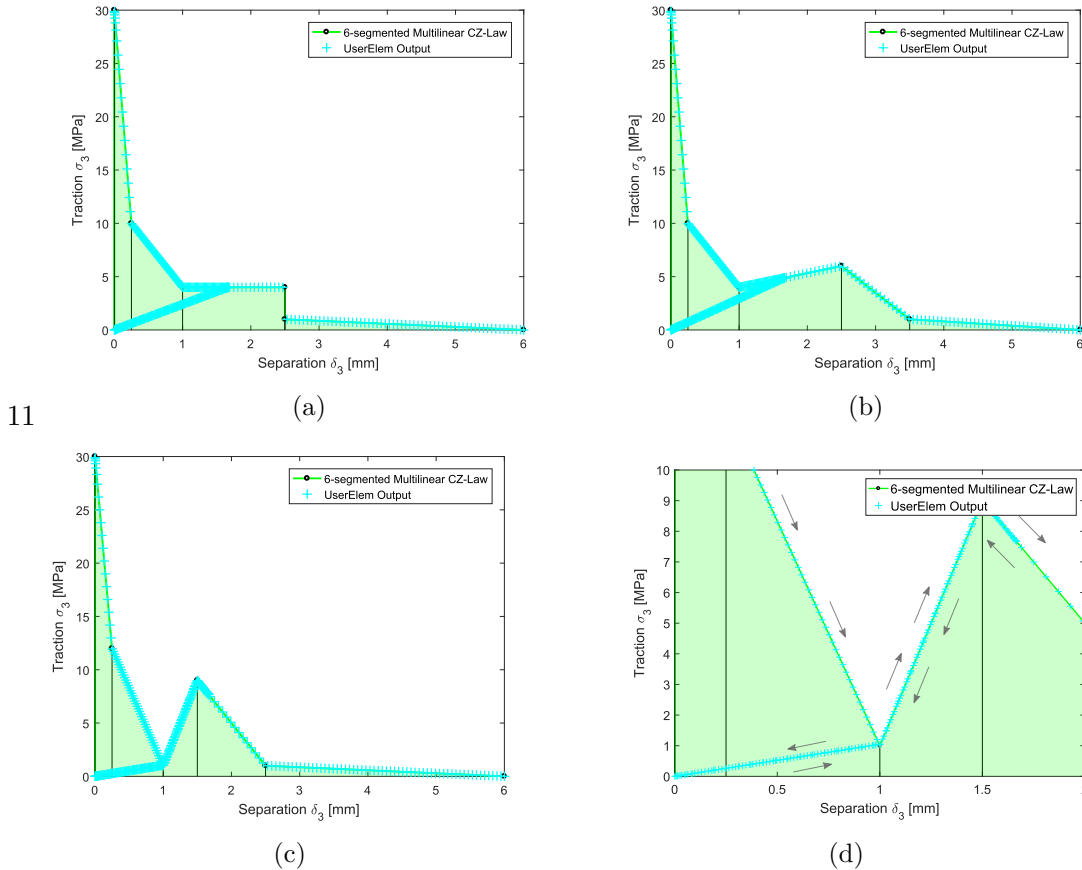


Figure 3.4: (a) Works well. (b) Works well. (c) Problem: Restoration of cohesive state. (d) Ideal loading/unloading of CZ law in fig. (c).

3.3.2 Mixed Mode Crack Opening

Having verified loading/unloading/reloading sequences for an arbitrary multilinear CZ law for pure mode I crack opening, mixed mode loading is considered next. For this purpose, the same FE model is considered as shown in Fig. 3.3a.

Three verification tests are performed for three different normal-shear opening mode mixity ratios β . The interface element is loaded quasi statically, by subjecting its nodes to prescribed displacements. Depending on the value of β , the prescribed displacements UX, UY, and UZ are set differently. Three values of β are tested: $\beta = [0.00, 0.41, 1.00]$. Values of $\beta = 0.00$ and $\beta = 1.00$ corresponds to pure mode I and pure mode S crack opening, respectively. The prescribed displacements for the different mode mixity ratios appears from Tab. 3.2. The separate mixed mode traction and separation points are calculated according to Eq. (2.4.12) and Eq. (2.4.17) respectively, under the assumption of $\eta = \xi = 1.40$.

Mode mixity ratio, β	UX	UY	UZ
0.00	0.00	8.00	0.00
0.41	3.89	5.66	0.00
1.00	5.00	0.00	0.00

Table 3.2: Prescribed displacements for three tests of different mode mixity ratio.

In Fig. 3.5 the solid lines represent the intended CZ law for the interface element, whereas the light blue crosses again represent outputs from the FE model. Appropriate nodal separations and tractions are extracted from the FE model according to Tab. 3.1, and plotted as shown in Fig. 3.5. In specific, EPEL,Y and EPEL,YZ are plotted along the first and second axes δ_3 and δ_s respectively. The work conjugate traction norm $\bar{\sigma}$ is calculated from the nodal stresses S,Y and S,YZ as:

$$\bar{\sigma} = \sqrt{(S,Y)^2 + (S,YZ)^2} \quad (3.3.1)$$

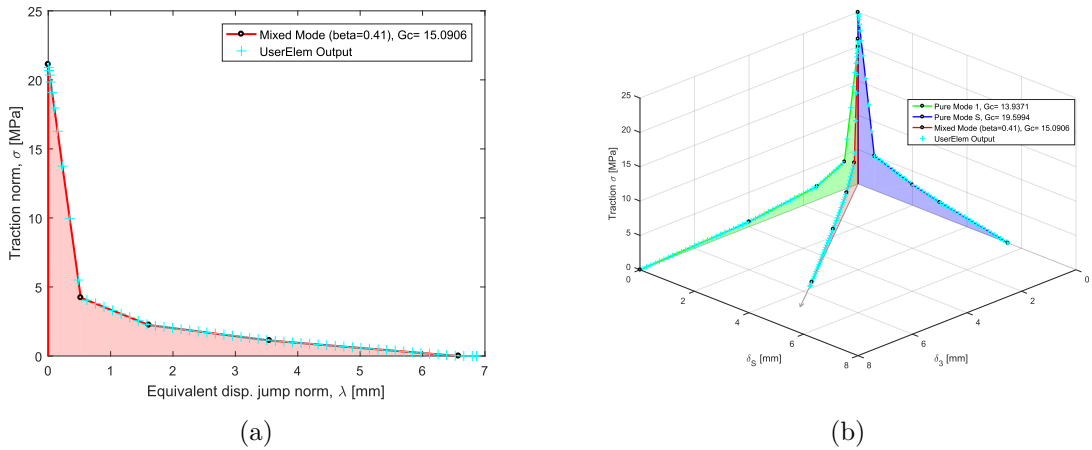


Figure 3.5: Verification example for 3 mode mixity ratios β .

The output from the FE model falls on top of the predefined CZ law, the material law for mixed mode loading is then considered verified. The mixed mode CZ law is defined such that it is energy consistent with the BK-criterion. This is double-checked below for the CZ law shown in Fig. 3.5b. Note, the critical energy dissipations appears in the legend of the figure.

$$G_c^{(BK)} = G_c^I + (G_c^{II} - G_c^I)B^\eta \Leftrightarrow \quad (3.3.2)$$

$$G_c^{(BK)} = 13.9371 + (19.5994 - 13.9371) \left(\frac{0.4074^2}{1 + 2 * 0.4074^2 - 2 * 0.4074} \right)^{1.40} = 15.0904 \quad (3.3.3)$$

Extra decimals of $\beta = 0.4074$ has been included to arrive at the same result as shown in the legend of Fig. 3.5b. The energy dissipation calculated using the BK criterion agrees with G_c in the legend of Fig. 3.5b for the mixed mode CZ law.

Inverse Parameter Identification Tool for CZ Laws

4.1 Introduction

A program called Inverse Parameter Identification Tool for Cohesive Zone Laws (IPIT-CZL) capable of determining CZ law parameters from experimental data is presented. In brief, the program receives experimental data from a delamination test, where the data includes a global structural response as e.g. applied moment versus angle of rotation. In the other hand, a numerical simulation using the FEM in combination with CZ modelling is meant to represent the real experiment. However, the simulation requires the definition of a CZ law to model the behavior of the material at the interface. As the parameters defining the CZ law are unknown beforehand, those will constitute the design variables, \vec{x} , of an optimization problem, that aims to minimize the difference between the global structural response of the experiment and that of the numerical simulation by making changes in \vec{x} .

An initial version of the tool was created by the authors of this work in [Jensen and Martos, 2016] and it is further developed and improved by:

- Defining the objective function as a least squares formulation in order to use the Jacobian to calculate the gradient and the Hessian.
- Benchmarking different optimization algorithms.
- Scaling the design variables to avoid an ill-conditioned problem.
- Using an approach for determining an appropriate perturbation size.
- Consistently use the same the equilibrium points of the numerical simulation in the formulation of the objective function.

In order to get an overview of the program, one can see the flowchart in Fig. 4.1. IPIT-CZL is formed by a group of MATLAB scripts which defines and solves the optimization problem, controls the calls to the numerical simulation and supplies it with the design variables. Following the flowchart from the top, an initial guess for the design variables, \vec{x}_0 , is provided to the numerical model which is generated and analyzed with ANSYS. The FE model output is compared to the experimental data and a residual vector, $\vec{r}(\vec{x})$, is established. It describes the difference in responses at discrete data points. Then, the residual vector is transformed into a scalar objective function, $f(\vec{x})$, using a least squares formulation. Lastly, the optimization algorithm seeks the minimum point of the objective function by iteratively changing the

design variables until a certain stopping criterion is met. Note that the stopping criteria are adjusted such that appropriate CZ parameters are found once a converged solution is obtained within a reasonable time.

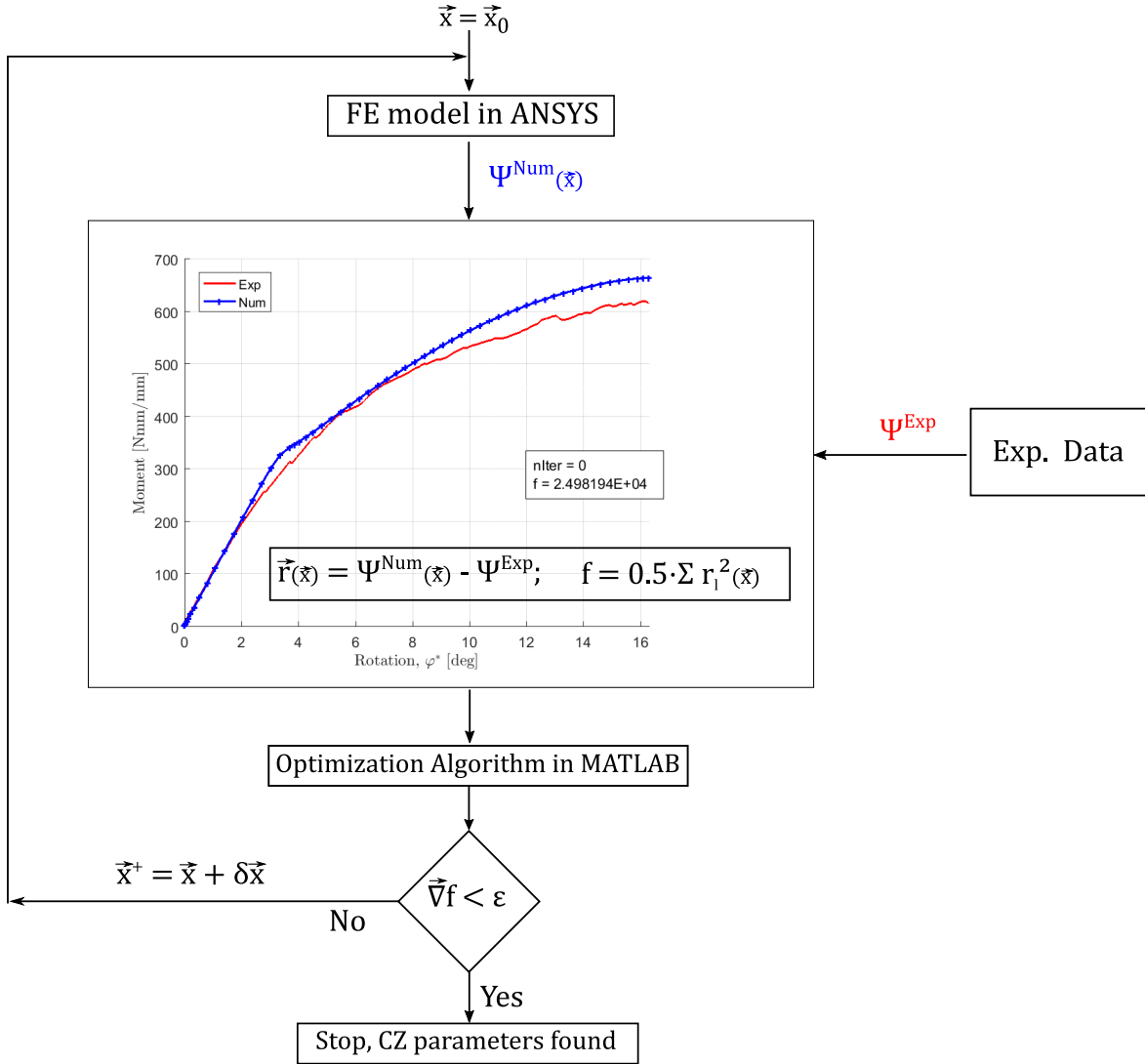


Figure 4.1: IPIT-CZL flowchart

The following sections of the chapter present in more details the optimization formulation, algorithm and settings, how the FE model is built, and experimental set-up used. Please note that the notation related to optimization is independent from the rest of the sections in this thesis, e.g. d , here, refers to the search direction whilst, elsewhere, it refers to the damage parameter. In addition, here the arrow $\vec{\bullet}$ is used to identify non physical vectors, namely arrays, e.g. \vec{x} which is a n-dimension vector including the design variables of the optimization problem. Thereby, the units of x_1 could be MPa while for x_2 could be kJ/m^2 . However, elsewhere in this thesis $\vec{\bullet}$ identify a physical vector e.g. the separation vector $\vec{\delta}$ formed by the two separation components δ_s and δ_3 which are the displacement jumps in shear and mode I, respectively.

4.2 Optimization

The present section contains an overall definition of the optimization problem dealt with in this work. A more thorough description of the algorithms can be found in [MathWorks, 2016, pp. 6.21-6.40], [Nocedal and Wright, 2006], [Waltz et al., 2006] and [Byrd et al., 1988]. The present application intends to establish the CZ parameters for a given specimen based on the minimum difference between two global structural responses, one measured in the laboratory and another simulated using the FEM. For the sake of clarity and simplicity, the global optimization settings and the algorithm selection are presented for an end-loaded DCB specimen in mode I modeled with a bilinear CZ law, where the critical energy release rate G_{Ic} and the onset traction $\sigma_3^{(1)}$ are the only two design variables involved. Additionally, in order to fine tune the optimizer and benchmark the different optimization methods available, it is very convenient to know a priori the value of the sought minimum. For that purpose, later in this section, the experimental curve $\vec{\Psi}^{Exp}$ introduced in Fig. 4.1 is replaced by the structural response of a numerical simulation with known CZ law.

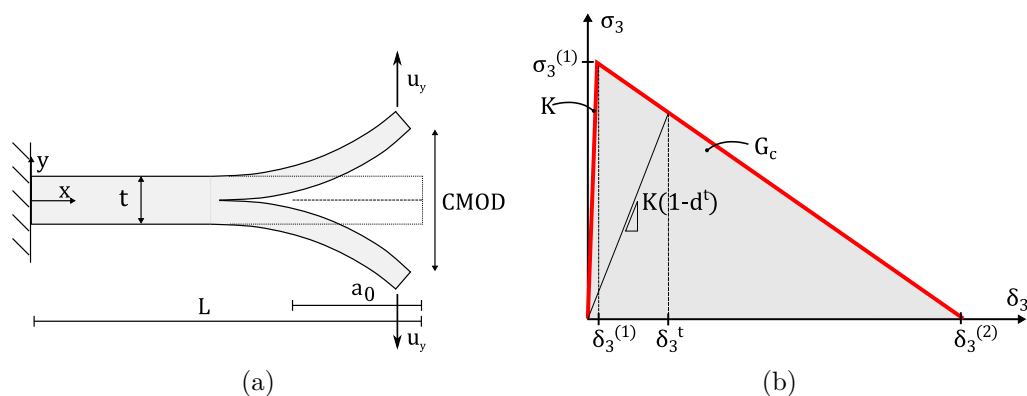


Figure 4.2: (a) End-loaded DCB specimen (b) Bilinear constitutive law.

Fig. 4.2a shows the analyzed specimen which has a pre-crack $a_0 = 25 \text{ mm}$ and whose length is $L = 100 \text{ mm}$, width is $b = 1 \text{ mm}$ and thickness is $t = 5 \text{ mm}$. Concerning the boundary conditions, the specimen is fixed in one end and displaced at the crack mouth an amount $CMOD = 5 \text{ mm}$ in the y -direction (mode I). The FE model shown in Fig. 4.3 has 1200 linear solid elements SOLID185 with enhanced strain option activated to avoid parasitic shear¹ [ANSYS, 2016] and 225 interface elements along the predefined fracture path. The formulation of the interface elements corresponds to the UserElem subroutine presented in Sec. 3.2. The element size in the length direction is 0.33 mm, 1 mm in the width and 1.25 mm in the thickness.

4.2.1 Nonlinear Optimization and Algorithm Selection

Nonlinear optimization implies that the objective function and/or constraints are nonlinear. It can be classified into direct search methods and gradient-based search methods. In direct methods, the search direction is based on 0th-order information, i.e. it is purely based on the objective function history. Whilst gradient-based methods uses 1st- and, when applicable, 2nd-order information, i.e. first and second order derivatives of the objective function $f(\vec{x})$ with respect to the design variables \vec{x} . The usage of the gradients and Hessians improves the convergence rate, nonetheless constricts the problem to continuous and twice differentiable

¹Enhance strain option adds some internal degree of freedom to the linear element in order to avoid parasitic shear to develop in bending dominated scenarios.

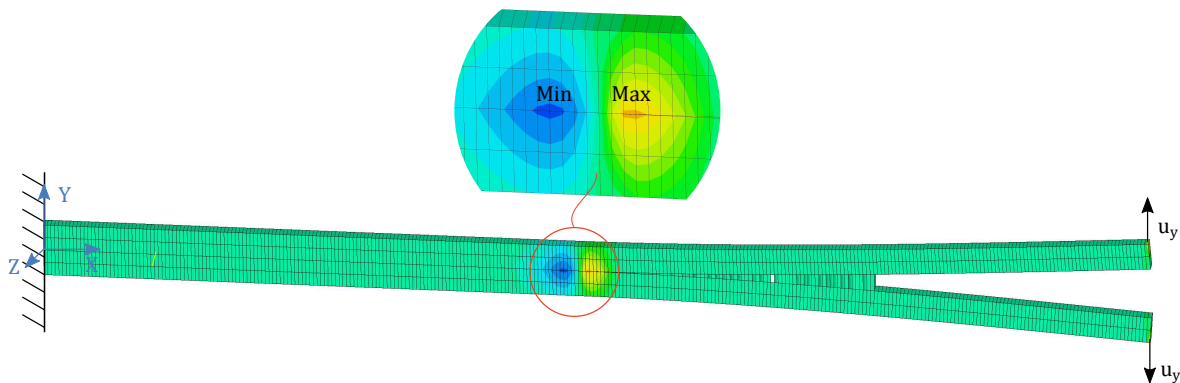


Figure 4.3: FE model of the end-loaded DCB specimen, σ_y is shown.

objective functions [Arora, 2012, p.412]. Hence, here it is assumed that the objective function is continuous and twice differentiable.

Minimizing the difference between two structural responses using a least squares formulation involves nonlinear optimization since the objective function is nonlinear. Secondly, the design variables are bounded avoiding unfeasible scenarios e.g. having $\sigma_3^{(i)} < 0$ or, for a multilinear CZ law, having $\sigma_3^{(i)} > \sigma_3^{(1)}$, thereby, the optimization is nonlinear and constrained. Furthermore, a gradient-based search method is used as fast convergence is crucial due to the computational demand of a function evaluation. Note that a function evaluation requires solving the nonlinear FE problem for the current design variables.

The algorithm selection is confined to the available options in MATLAB, wherein *fmincon* is the best suited function for IPIT-CZL as it allows more freedom in the definition of the objective function, gradient and Hessian compared to other functions. The subroutine *fmincon* includes three types of optimization algorithms: interior-point, trust-region-reflective and sequential quadratic programming (SQP). The use of a least squares formulation has the advantage of providing a more accurate approximation of the gradient and Hessian of $f(\vec{x})$ with respect to other formulations of the objective function. Therefore, the last option is disregarded since the SQP algorithm implemented in MATLAB is unable to import the Hessian, which it is aimed to be supplied but instead the algorithm calculates it internally by forward finite difference of the gradients.

The interior-point algorithm included in *fmincon* is presented in [Waltz et al., 2006]. It is a line search Newton's/quasi-Newton's method that approximates the original inequality constrained optimization by a sequence of equality constrained subproblems, which are easier to solve. The search direction is calculated by solving the Karush-Kuhn-Tucker (KKT) necessary conditions using direct linear algebra, and the size of the step along the search direction is calculated via line search. The step size varies between 0 and 1, where 1 corresponds to a full Newton step. This implementation of the interior-point algorithm is able to switch over to a trust region scheme that uses a conjugate gradient step whenever local nonconvexity or, Hessian² or Jacobian³ rank deficiency is met. In those situations, a pure line search interior algorithm is not able to compute the next design point because, the line search requires the approximate problem to be locally convex near the current iteration to calculate the step size (see [Arora, 2012, pp. 418,419]), whereas for rank deficiency or near deficiency, the search

²It is referred to the Hessian of the Lagrangian function $H(\vec{x})$ to be later introduced.

³It is referred to the Jacobian of the constraints J_h and J_g to be later introduced.

direction cannot be determined by direct linear algebra since a singular or near singular matrix has to be factorized [Waltz et al., 2006] [Nocedal and Wright, 2006, p. 23].

The trust-region-reflective algorithm, presented in [Byrd et al., 1988], is a trust region Newton's/quasi-Newton's method that approximate the original objective function with a simpler function which is minimized in the neighborhood of the current point, which in turn represents the region of trust. If the candidate point is not reducing the original objective function, then the size of the trust region is shortened and a new candidate point is sought. The step used is always limited to be smaller or equal than the size of trust region. When the Hessian is positive definite, a fraction of the (or a full) Newton step is taken, so that the superlinear convergence from the Newton steps can be reached [Nocedal and Wright, 2006, p. 73]. In case that the Hessian or the Jacobian is indefinite, or that the current iterate is in a local nonconvex region, a step closer to a Cauchy step is taken. This is a step along the steepest descent direction which in turn ensures progress toward feasibility and optimality [Waltz et al., 2006] [Nocedal and Wright, 2006, pp. 38-41,71].

Comparing both algorithms, the following pros and cons for each method are found:

- Situations with indefinite Hessian or Jacobian, or local nonconvexity are better addressed in trust region algorithms [Waltz et al., 2006].
- It could result difficult finding a smooth transition between the line search and the trust region steps in the interior point algorithm [Waltz et al., 2006].
- Linear inequality constraints are available in the interior point algorithm, but not in the trust region algorithm implemented in MATLAB.

As discuss in a later section, it is intended to enforce CZ law to be a softening law. This is done by including linear inequality constraints to the design variables, therefore, only the interior-point algorithm incorporates all the desired features and thence it is implemented in IPIT-CZL.

4.2.2 Problem Formulation for the Interior-point Algorithm

This subsection presents a generic definition of the interior-point or barrier method that uses Newton and conjugate gradient steps. Here, the focus will lie on the understanding of the overall solution process and the specific algorithm implementation, which MATLAB did not made available and may slightly differ from the present one as seen for e.g. in the primal-dual system in Eq. (4.2.12), is out of the scope of this thesis.

A least squares formulation is considered in this work, where the objective function, $f(\vec{x})$, in Eq. (4.2.1) is to be minimized.

$$\begin{aligned} \min_{\vec{x}} f(\vec{x}) &= \frac{1}{2} \|\vec{r}(\vec{x})\|^2 = \frac{1}{2} \sum_{l=1}^m r_l^2(\vec{x}) & (4.2.1) \\ \text{subjected to } & h_i(\vec{x}) = 0, \quad i = 1 \dots a \\ & g_j(\vec{x}) \leq 0, \quad j = 1 \dots b \end{aligned}$$

where $f(\vec{x})$ is a scalar function, $\|\vec{r}(\vec{x})\|$ is the Euclidean norm of the residual vector, \vec{x} is a vector containing the n^* design variables, m is the number of residual entries, $h(\vec{x})$ are the linear equality constraints and $g(\vec{x})$ are the linear inequality constraints. The residual vector

is defined as shown in Eq. (4.2.2).

$$\vec{r}(\vec{x}) = \begin{bmatrix} \Psi_1^{Num}(\vec{x}) - \Psi_1^{Exp} \\ \Psi_2^{Num}(\vec{x}) - \Psi_2^{Exp} \\ \vdots \\ \Psi_m^{Num}(\vec{x}) - \Psi_m^{Exp} \end{bmatrix} \quad (4.2.2)$$

wherein $\Psi^{Num}(\vec{x})$ is a numerical global structural response obtained through a FE simulation and Ψ^{Exp} is an experimental global structural response measured in the laboratory. Thereby, the difference between the curves $\Psi^{Num}(\vec{x})$ and Ψ^{Exp} is minimized.

The interior-point algorithm approximates the original problem in Eq. (4.2.1) by a sequence of equality constraints subproblems, called barrier subproblems, shown in Eq. (4.2.3). With this transformation, the inequality constraints have been converted into equality constraints, and the objective function include an extra logarithmic term, called barrier function, in charge of penalizing the objective function, whenever a inequality constraint is violated⁴.

$$\begin{aligned} \min_{\vec{x}, \vec{s}} f_\mu(\vec{x}, \vec{s}) &= f(\vec{x}) - \mu \sum_{j=1}^b \ln s_j \\ \text{subjected to } h_i(\vec{x}) &= 0, \quad i = 1 \dots a \\ g_j(\vec{x}) + s_j &= 0, \quad j = 1 \dots b \end{aligned} \quad (4.2.3)$$

wherein μ is the barrier parameter which is a small positive scalar controlling the contribution the barrier function in f_μ [Jensen and Bard, 2003] and the convergence of Eq. (4.2.3) to Eq. (4.2.1) as μ tends towards zero [Robere, 2012], and \vec{s} is vector containing the slack variables. Eq. (4.2.3) is in turn transformed into an unconstrained optimization problem using the Lagrangian function:

$$\mathcal{L}(\vec{x}, \vec{v}, \vec{u}, \vec{s}) = f_\mu(\vec{x}, \vec{s}) + \vec{v}^T h(\vec{x}) + \vec{u}^T (g(\vec{x}) + \vec{s}) \quad (4.2.4)$$

wherein \vec{v} and \vec{u} are the a- and b-dimensional Lagrange multiplier vectors. The KKT optimality conditions for Eq. (4.2.4) are formed by the gradient conditions in Eq. (4.2.5) to (4.2.7), feasibility check for inequalities in Eq. (4.2.9), switching conditions in Eq. (4.2.8) and non-negativity of Lagrange multiplier \vec{u} in Eq. (4.2.10):

$$\frac{\partial \mathcal{L}(\vec{x}, \vec{v}, \vec{u}, \vec{s})}{\partial \vec{x}} = 0 \Leftrightarrow \vec{\nabla} f(\vec{x}) + J_h(\vec{x})^T \vec{v} + J_g(\vec{x})^T \vec{u} = 0 \quad (4.2.5)$$

$$\frac{\partial \mathcal{L}(\vec{x}, \vec{v}, \vec{u}, \vec{s})}{\partial \vec{v}} = 0 \Leftrightarrow h(\vec{x}) = 0 \quad (4.2.6)$$

$$\frac{\partial \mathcal{L}(\vec{x}, \vec{v}, \vec{u}, \vec{s})}{\partial \vec{u}} = 0 \Leftrightarrow g(\vec{x}) + \vec{s} = 0 \quad (4.2.7)$$

$$\frac{\partial \mathcal{L}(\vec{x}, \vec{v}, \vec{u}, \vec{s})}{\partial \vec{s}} = 0 \Leftrightarrow S\Lambda_g - \mu \vec{e} = 0 \quad (4.2.8)$$

$$\text{feasibility check : } s_j \geq 0 \quad j = 1 \dots b \quad (4.2.9)$$

$$\text{non-negativity of } \vec{u} : u_j \geq 0 \quad j = 1 \dots b \quad (4.2.10)$$

where $\vec{\nabla} f(\vec{x})$ is the gradient of the objective function, $J_h(\vec{x})$ and $J_g(\vec{x})$ are the Jacobian matrices of the equality and inequality constraints, S and Λ_g are diagonal matrices containing the terms in the vectors \vec{s} and \vec{u} , respectively, and \vec{e} is a b-dimensional vector containing ones.

⁴As a slack variable tends towards zero, the corresponding logarithmic term tends to negative infinity.

The Jacobian matrix of a q-vector function $\vec{t}(\vec{x})$ is described as the matrix containing the first order partial derivatives of the function with respect to \vec{x} :

$$J_t(\vec{x}) = \frac{\partial t_i}{\partial x_j} \equiv \begin{bmatrix} \frac{\partial t_1}{\partial x_1} & \cdots & \frac{\partial t_1}{\partial x_n} \\ \vdots & \ddots & \vdots \\ \frac{\partial t_q}{\partial x_1} & \cdots & \frac{\partial t_q}{\partial x_n} \end{bmatrix} \quad (4.2.11)$$

Solving Eq. (4.2.5) through (4.2.10), using the Newton's method, yields Eq. (4.2.12), known as the primal-dual system, which in turn is solved for \vec{d}_x , \vec{d}_s , \vec{d}_v and \vec{d}_u using a LDL factorization. This last step is relevant as it represents the most demanding computation, regardless an objective function evaluation, and is used to determine the type of step performed: a direct step when $H(\vec{x}) > 0$ or else a conjugate gradient step.

$$\begin{bmatrix} H & 0 & J_h^T & J_g^T \\ 0 & \Lambda_g & 0 & S \\ J_h & 0 & 0 & 0 \\ J_g & S & 0 & 0 \end{bmatrix} \begin{bmatrix} \vec{d}_x \\ \vec{d}_s \\ \vec{d}_v \\ \vec{d}_u \end{bmatrix} = - \begin{bmatrix} \vec{\nabla} f + J_h^T \vec{v} + J_g^T \vec{u} \\ S\Lambda_g - \mu\vec{e} \\ h \\ g + \vec{s} \end{bmatrix} \quad (4.2.12)$$

where \vec{d}_x , \vec{d}_s , \vec{d}_u , \vec{d}_v are the search direction for the design variables, slack variables and Lagrange multipliers respectively, and $H \equiv H(\vec{x})$ is the Hessian matrix of the Lagrangian function $\mathcal{L}(\vec{x}, \vec{s}, \vec{v}, \vec{u})$ shown in Eq. (4.2.13). For simplicity, the formula above do not include the parenthesis (\vec{x}) .

$$H(\vec{x}) = \nabla^2 f(\vec{x}) + \sum_{i=1}^b v_i \nabla^2 h_i(\vec{x}) + \sum_{j=1}^a u_j \nabla^2 g_j(\vec{x}) \quad (4.2.13)$$

Having found the search direction, the candidate point, the new slack variables and the new Lagrange multipliers for the next iteration are calculated as:

$$\vec{x}^+ = \vec{x} + \alpha_x \vec{d}_x \quad (4.2.14)$$

$$\vec{s}^+ = \vec{s} + \alpha_s \vec{d}_s \quad (4.2.15)$$

$$\vec{u}^+ = \vec{u} + \alpha_u \vec{d}_u \quad (4.2.16)$$

$$\vec{v}^+ = \vec{v} + \alpha_v \vec{d}_v \quad (4.2.17)$$

where α_x , α_s , α_u , α_v are the stepsizes which have been calculated by a line search approach. The candidate point to be accepted as the point for the next iteration needs to generate a sufficient reduction to a merit function (shown in Eq. (4.2.18)), yet another linearization of the objective function which is easier to evaluate than Eq. (4.2.3). Thus, it is possible that an accepted candidate point would not decrease the original objective function, being more probable to occur for problems with large number of design variables, as well as, for highly non-linear problems. The points not fulfilling the aforementioned requirement are refused and a new candidate is sought.

$$f_\mu(\vec{x}, \vec{s}) + \nu \left\| \begin{Bmatrix} h(\vec{x}) \\ g(\vec{x}) + \vec{s} \end{Bmatrix} \right\| \quad (4.2.18)$$

The Newton or direct step obtained by solving Eq. (4.2.12) is the first choice, however it is not always possible to find a solution for such a system. In situations when the Hessian is not positive definite or the problem is locally non-convex, the algorithm switches over to a Trust region method that calculates a conjugate gradient step instead. As the primal-dual system is unsolvable, the alternative is to simplify even further the approximate problem in

Eq. (4.2.3) by a quadratic function with linearized constraints, shown in Eq. (4.2.19), that represents the problem in a close region.

$$\begin{aligned} \min_{\vec{d}_x, \vec{d}_s} \quad & \vec{\nabla} f(\vec{x})^T \vec{d}_x + \frac{1}{2} \vec{d}_x^T \nabla^2 \mathcal{L} \vec{d}_x + \mu \vec{e}^T S^{-1} \vec{d}_s + \frac{1}{2} \vec{d}_s^T S^{-1} \Lambda \vec{d}_s \\ \text{subjected to:} \quad & h(\vec{x}) + J_h(\vec{x}) \vec{d}_x = 0 \\ & g(\vec{x}) + J_g(\vec{x}) \vec{d}_x + \vec{d}_s = 0 \end{aligned} \quad (4.2.19)$$

The conjugate gradient step is calculated by solving Eq. (4.2.19), where the Lagrange multipliers are obtained from Eq. (4.2.5), and keeping $\vec{u} > 0$ and $\vec{s} > 0$.

4.2.3 Quasi-Newton approximation. Calculation of 1st and 2nd Order Sensitivities

The previous subsection is defined for a pure Newton method, for the problem at hand derivatives of $f(\vec{x})$, which are a necessity for the pure Newton method, are not available. Here, it is described how a quasi-Newton approximation of the problem can be obtained by using forward finite difference (FFD) in a least squares formulation. The least squares formulation is widely used for curve fitting and inverse parameter identification. Its main advantage is that a good estimate of first and second order information are available by only applying FFD to one common quantity, the Jacobian of $\vec{r}(\vec{x})$. The existence of this common quantity can be seen by application of the chain rule of differentiation for the gradient and the product rule of differentiation for the Hessian.

As mention before, the entries of this m-by-n Jacobian matrix are calculated by FFD of the residual function, i.e. the change in the residual vector for a given perturbation $\delta \vec{x}$ in the design variables over the perturbation:

$$J_r(\vec{x})[i, j] \approx \frac{r_i(\delta \vec{x}_j + \vec{x}_j) - r_i(\vec{x}_j)}{\delta \vec{x}_j} \quad (4.2.20)$$

The size of the perturbation is key to obtain a good approximation of the derivative, the error of this approximation increases as the perturbation size increases, although too small perturbation size yields to imperceptible change in the residual vector. Thus, it is necessary to perform a sensitivity study in order to find an adequate perturbation size. For the bilinear problem shown in Fig. 4.2, the perturbations are varied within the range [1e-1 ; 1e-12]. Note that while δx_1 is under analysis, δx_2 is fixed to 1e-6, and vice versa. Furthermore, note that as mention in the introduction of this section, the optimization problem is simplified by substituting the experimental response by a numerical response where $x_1 \equiv G_{Ic} = 0.6132 \text{ kJ/m}^2$ and $x_2 \equiv \sigma_3^{(1)} = 12 \text{ MPa}$ in Sec. 4.2.3 - 4.2.6. This substitution leads to a smoother and more convex objective function as the experimental noise is removed, and ensures the existence of at least one local minimum of known value and for which $f(\vec{x}) = 0$. Hence, it is easier to determine which algorithms and parameters perform best as the right solution is known beforehand. The results of the sensitivity study can be seen in Tab. 4.1, Fig. 4.4a and Fig. 4.4b.

$\delta \vec{x}$	1e-1	1e-2	1e-3	1e-4	1e-5	1e-6	1e-7	1e-8	1e-9	1e-10	1e-11	1e-12
$\vec{\nabla} f(x_1)$	-630.77	-669.33	-625.18	-616.58	-607.18	-604.35	-604.48	-605.27	-618.65	-700.86	-623.84	0
$\vec{\nabla} f(x_2)$	0.080531	0.038034	0.30479	0.081923	0.080836	0.080384	0.085095	-0.022602	0	0	0	0

Table 4.1: Sensitivity study to find an appropriate perturbation size for $x_1 = G_{Ic}$ and $x_2 = \sigma_3^{(1)}$.

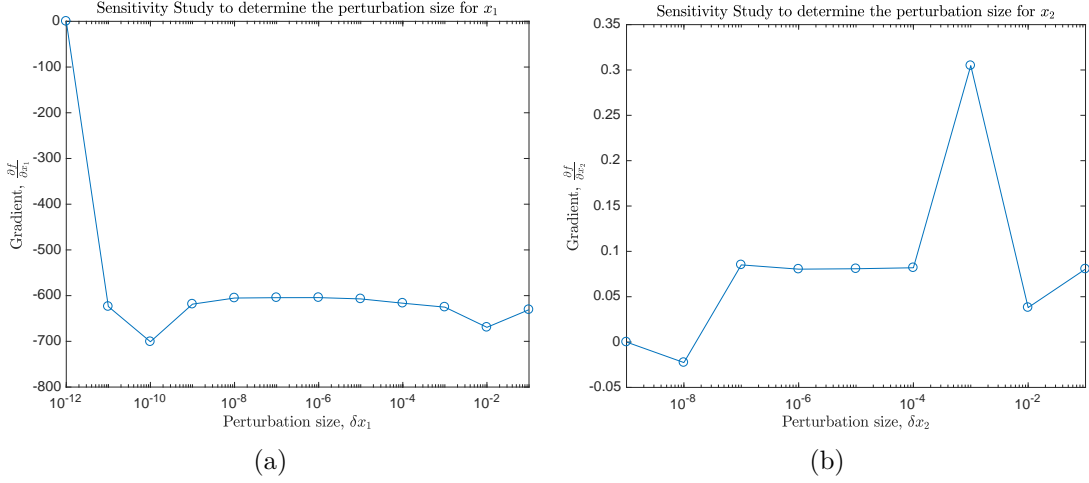


Figure 4.4: Sensitivity study to find an appropriate perturbation size for (a) $x_1 = G_{Ic}$ and (b) $x_2 = \sigma_3^{(1)}$.

As seen in the tables and figures above, similar gradients are reached in the range $[1e-5 \text{ } 1e-8]$ for x_1 while for x_2 is $[1e-4 \text{ } 1e-7]$. As a rule of thumb, an intermedium value in the observed stable range is normally chosen, i.e. not too large nor too small perturbation. Thus, the perturbation sizes for G_{Ic} and $\sigma_3^{(1)}$ are set to $1e-7$ and $1e-6$, respectively.

Having obtained $J_r(\vec{x})$, the gradient and the Hessian can be calculated according to Eq. (4.2.21) and Eq. (4.2.22), respectively.

$$\vec{\nabla} f(\vec{x}) = J_r(\vec{x})^T \vec{r}(\vec{x}) \quad (4.2.21)$$

$$H(\vec{x}) = J_r(\vec{x})^T J_r(\vec{x}) + \sum_{l=1}^m r_l(\vec{x}) Q_l(\vec{x}) \quad (4.2.22)$$

where $Q_l(\vec{x})$ are second-order derivatives of each $r_l(\vec{x})$. In lack of an analytic expression for $\vec{r}(\vec{x})$ those derivatives cannot be obtained, hence the Hessian is estimated only using the first term in Eq. (4.2.22):

$$H(\vec{x}) \approx J_r(\vec{x})^T J_r(\vec{x}) \quad (4.2.23)$$

4.2.4 Design Space

In order to picture the degree of convexity of the problem at hand, it is decided to explore the design space. For the simple bilinear case, a contour and a surface plot are generated, Fig. 4.5a and Fig. 4.5b, respectively. The grid is made of 99×39 equidistant points in the design space. Furthermore, a second contour and surface plot are generated, in the range $G_{Ic} \in [0.1 \text{ to } 1]$ and $\sigma_3^{(1)} \in [1 \text{ to } 20]$, to take a closer look in the convex zone, Fig. 4.5c and Fig 4.5d, respectively. In this case, the grid includes 101×51 points. In Fig. 4.5d, the points where the objective function is within 0 (dark blue) and $1e-2$ (light blue) are colored, the remaining points are left in white.

In the aforementioned figures, the problem appears to be notably convex, however it is important to remark that this design space corresponds to the ideal case where the experimental data has been replaced by a numerical simulation and that there are only two design variables. Thus, it is expected that IPIT-CZL will deal with problems of higher degree of non-convexity in real applications, wherein the experimental curve is not simulated and smooth, and more design variables are used.

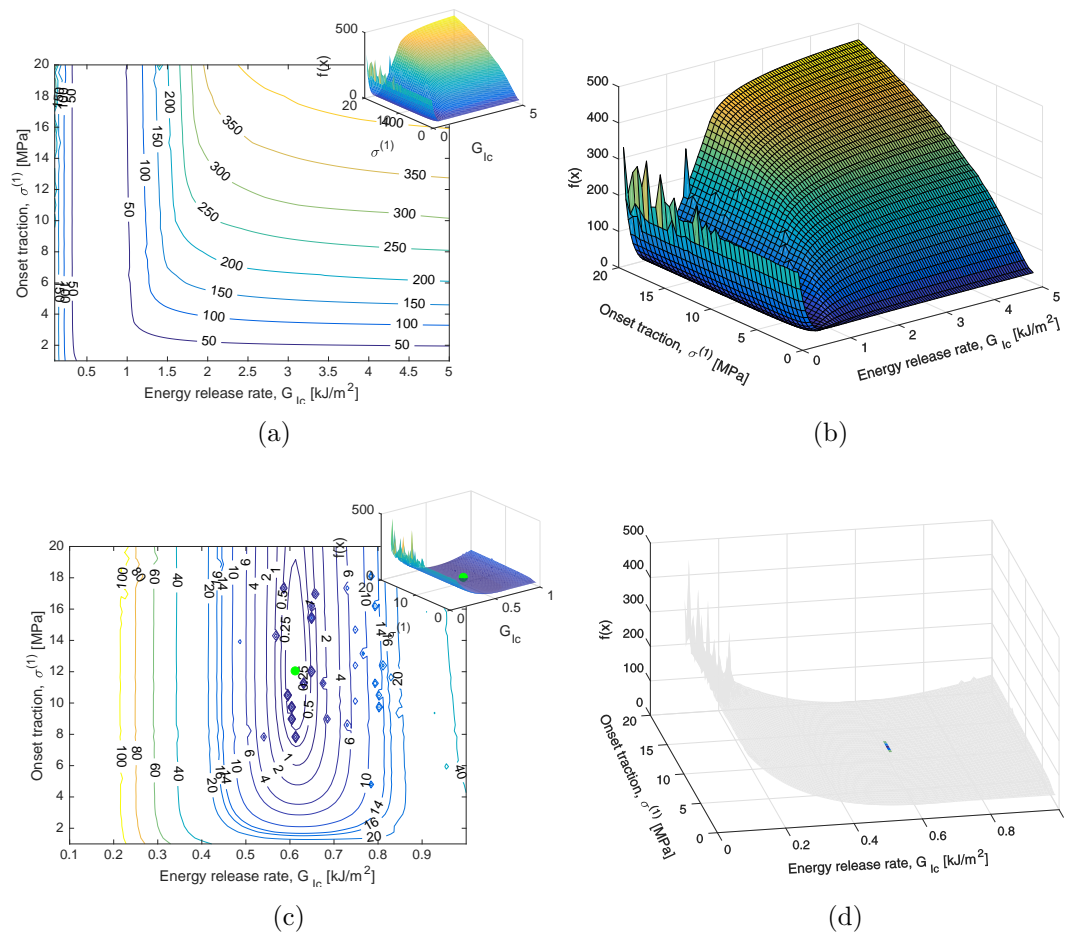


Figure 4.5: (a) Contour plot and (b) Surface plot of the design space. (c) Contour plot (optimum displayed as a green dot) and (d) Surface plot of the convex area.

4.2.5 Scaling of the Problem

In a well-conditioned optimization problem there is no domination of some design variables over others. The associated contour plot would show circular contours and the eigenvalues of the associated Hessian matrix would be of the same order of magnitude. Looking at Fig. 4.5, and specially Fig. 4.5c, elliptical contours are observed. Moreover, examining the eigenvalues of the Hessian, the difference between the highest and lowest eigenvalues is from 2 to 7 orders of magnitudes. As an example, the Hessian matrix and its eigenvalues for the second iteration in one of the solutions presented in the next section are included:

$$H(\vec{x}) = \begin{bmatrix} 2885.4 & 0.45121 \\ 0.45121 & 0.001471 \end{bmatrix} \Rightarrow \text{eigenvalues}(H(\vec{x})) = \left\{ \begin{array}{l} 2885.4 \\ 0.0014004 \end{array} \right\}$$

These facts point out an ill-conditioned optimization problem where G_{Ic} is the dominating variable. In this case, and as seen in [Jensen and Martos, 2016, pp.41-42], the algorithm find first a closer estimate of G_{Ic} and then starts modifying $\sigma_3^{(1)}$ due to this issue. To overcome this situation, some sort of scaling needs to be implemented. Different options are available, e.g. weighting the residual points, $r_l(\vec{x})$, differently providing more relevance to meaningful points; doing a change of variables such that the resulting problem is well-conditioned; or making use of the optimizers built-in preconditioners. In the present work, it is decided to use the built-in preconditioners.

4.2.6 Benchmark Test

For sake of comparison and even though the most appropriate algorithm has already been chosen, the interior-point, the trust region and the former algorithm implemented in IPIT-CZL, presented in [Jensen and Martos, 2016]⁵, are benchmarked. The test corresponds to the bilinear problem in Fig. 4.2. The results from the benchmark test are included in Tab. 4.2. The starting points have been chosen based on the observed design space and the stopping tolerances for the minimum allowable change in the step size and in the objective function, from iteration to iteration, are both set to 1e-20.

Algorithm	Starting Point	Number of Iterations	Number of f. evals.	Time (h m s)	Converged Point	$f(\vec{x})$
Trust-region-reflective	[0.2 ; 8]	10	34	0 h 15' 51.12"	[0.6132 ; 12]	3e-18
	[5 ; 20]	10	34	0 h 14' 52.58"	[0.6132 ; 12]	1.0635e-15
	[5 ; 1]	17	55	0 h 27' 47.67"	[0.6132 ; 12]	0
	[3 ; 10]	11	37	0 h 18' 35.07"	[0.6132 ; 12]	1.5e-18
	[0.7 ; 1]	12	40	0 h 20' 48.42"	[0.6132 ; 12]	2.5e-18
	[0.5 ; 20]	7	25	0 h 13' 17.51"	[0.6132 ; 12]	2e-18
Interior-point	[0.2 ; 8]	12	40	0 h 18' 56.92"	[0.6132 ; 12]	3.4e-17
	[5 ; 20]	16	52	0 h 27' 6.65"	[0.6132 ; 12]	4.7675e-15
	[5 ; 1]	19	61	0 h 32' 48.74"	[0.6132 ; 12]	9.107e-15
	[3 ; 10]	18	58	0 h 30' 15.43"	[0.6132 ; 12]	5.768e-15
	[0.7 ; 1]	11	37	0 h 19' 21.67"	[0.6132 ; 12]	1.95e-17
	[0.5 ; 20]	18	43	0 h 30' 15.43"	[0.6132 ; 12]	8.29e-15
SQP (former IPIT-CZL version)	[0.2 ; 8]	17	78	0 h 47' 16.12"	[0.6132 ; 12]	1e-17
	[5 ; 20]	38	197	1 h 42' 54.83"	[0.6132 ; 12]	5.9648e-14
	[5 ; 1]	26	133	1 h 6' 5.23"	[0.6132 ; 12]	1.8e-17
	[3 ; 10]	31	152	1 h 13' 44.62"	[0.6132 ; 12]	3.4256e-14
	[0.7 ; 1]	23	110	0 h 55' 32.31"	[0.6132 ; 12]	3.7721e-13
	[0.5 ; 20]	18	88	0 h 44' 51.22"	[0.6132 ; 12]	0

Table 4.2: Benchmark test results for different optimization algorithms.

⁵Using a least squares formulation as well, for a reader coming from [Jensen and Martos, 2016] that is $p = q = 2$.

The two proposed algorithms performs substantially better than the previously used SQP, which in the former IPIT-CZL version did not have the built-in preconditioners activated. The improvement is partially due to the preconditioners but mostly due to better estimates on the second order information. Concerning the best performance, trust-region-reflective is the fastest in five out of six cases. Moreover, summing up all results, its total computation time is 1 h 51' 12.37" whilst the interior-point takes 2 h 38' 44.84", i.e. 47' 32.47" difference. Nonetheless, the inability of the trust region algorithm to include inequality constraints restrict to the use of the interior-point algorithm. Based on the present results, and if MATLAB includes (in a near future) a new implementation of the trust region algorithm with inequality constraints, then it is recommended to repeat this benchmark to see whether the new trust region algorithm still performs better than the interior-point.

4.3 IPIT-CZL Subroutines

Having introduced the overall idea of IPIT-CZL and the optimization problem involved, this section aims to provide the reader a better understanding of the subroutines included in IPIT-CZL and the macro files used to create the numerical model. The software used for the FEA is ANSYS v.17.2 Mechanical APDL. There are four macro files written in Mechanical APDL language, that can be found in the enclosed compressed folder. A file called FileName.DAT includes the pre-processing commands i.e. geometry, material, element type, mesh, BCs and solver settings. It also inputs the CZ parameters stored in a file called FileName.DesVar, the interface element definition included in UserElemIPIT.DAT, the load steps saved in a file called FileName.LSfile and the post-processing contained in PlotMomentDisp.MAC. Regarding the MATLAB files, a total of 11 subroutines are used which are shortly described in the following bullet points.

- **Mainprogram.m:** This function serves as IPIT-CZL's main program and thus by executing it IPIT-CZL starts. Global variables and optimization settings including number of design variables, algorithm selection, constraints and perturbation sizes are defined here. Another important task of this function is to create a batch file for invoking the FEA in ANSYS.
- **InitialguessAndBounds.m:** Initial guess and bounds for the design variables \vec{x} are declared in this subroutine.
- **CZparameters.m:** This file inputs the design variables \vec{x} and computes the remaining dependent variables to fully describe a CZ law. The dependent variables are output. Moreover, it plots a figure containing the CZ law at the current iteration.
- **WriteDesVar.m:** Reads the design variables and the dependent variables generated in the previous subroutine in order to generate a FileName.DesVar file with a complete description of the CZ law. This file is written in Mechanical APDL language such that it can be directly imported in ANSYS.
- **LoadStepFiles.m:** This function generates a FileName.LSfile file with the load steps used in the FEA. Those load steps correspond to the equilibrium points used in the comparison with experimental data. The main macro file FileName.DAT inputs the FileName.LSfile file.
- **HessianInterior.m:** The interior-point algorithm in MATLAB requires the Hessian matrix to be provided as output of a separate function, handled by *fmincon*. This is because there is a contribution from the equality and inequality constraints to the

Hessian. The contribution, which can be seen in Eq. (4.2.13), depends on the Lagrange multipliers \vec{v} and \vec{u} which are internally computed during the optimization process, and hence they will be provided together in a vector $\psi = \begin{Bmatrix} \vec{v} \\ \vec{u} \end{Bmatrix}$ by *fmincon* every time it calls *HessianInterior.m*. Nevertheless, this work deals with inequality constraints which are 1st order polynomials, therefore only the second order derivatives of the objective function are used to compute the Hessian. As the inputs for *HessianInterior.m* cannot be changed, to calculate the Hessian, the Jacobian is made available by declaring it as global variable.

- **ReadMonitor.m:** In order to detect whether convergence issues arise, this file read the monitoring file called *FileName.mntr*, a file that ANSYS generates during the analysis. The output from this file is a flag which is set to 1 for non-convergence solution otherwise is set to 0.
- **ReadOutputs.m:** It opens a given text file and extract the global structural response. It is used for both experimental and numerical responses.
- **PlotResponse.m:** As its name indicates, this subroutine generates a plot of the output from the current numerical simulation and the experimental curve. Both global structural responses are included in the same figure in this manner it is easy to visualize the progress of the optimization.
- **MyANSYSCall.m:** Executes the ANSYS batch file and calculates the objective function.
- **MyANSYSCall_ObjAndGrad.m:** This file provides *fmincon* with the objective function and the gradient. The objective function is obtained by invoking *MyANSYSCall.m* whilst the gradient is calculated with the Jacobian matrix which is approximated by FFD as shown in Eq. (4.2.20).

4.3.1 Description of IPIT-CLZ

Having presented the idea behind IPIT-CLZ and the subroutines that shapes it, this part of the section deepens in the program skeleton. Elaborating on *Mainprogram.m*, *MyANSYSCall_ObjAndGrad.m*, *HessianInterior.m* and *MyANSYSCall.m* is enough to conceive the program. An interested reader can find all the subroutines in the enclosed compressed folder.

Algorithm 1 Mainprogram.m

- 1: The following global variables are declared: *FileName* defining the current job name; *nDesVar* including the number of design variables; $\delta\vec{x}$ a vector containing the perturbation sizes and $J_r(\vec{x})$ the Jacobian matrix of $\vec{r}(\vec{x})$.
 - 2: $[\vec{x}_0, LowBnd, UppBnd] = \mathbf{Call}$ InitialguessAndBounds(*nDesVar*). This function call generates the initial guess for the design variables \vec{x}_0 and sets the lower and upper bounds of the design space.
 - 3: Define the linear inequality constraints $g_j(\vec{x}) \leq 0$ in matrix form as $A\vec{x} \leq \vec{b}$ in order to ensure that the CZ law is a softening law by making the consecutive traction smaller than or equal to the previous value. E.g. $\sigma_3^{(3)} \leq \sigma_3^{(2)}$.
 - 4: Create the ANSYS batch file used to execute the FEA program in MyAnsysCall.m.
 - 5: Assign perturbation size to each design variable, e.g $\delta x_1 = 1e-6$ corresponds to the perturbation size for the first design variable x_1 . The perturbation is used to approximate the Jacobian matrix by FFD.
 - 6: Set the design variable equals to the initial guess: $\vec{x} = \vec{x}_0$.
 - 7: Select the optimization algorithm options: choose algorithm and termination tolerances. Call the nonlinear optimization function *fmincon*: $[\vec{x}, f(\vec{x})] = \mathbf{Call}$ *fmincon*(@MyANSYSCall_ObjAndGrad, \vec{x}_0 , A , \vec{b} , [], [], *LowBnd*, *UppBnd*, [], *options*). Wherein the first entry is a call to the subroutine MyANSYSCall_ObjAndGrad.m which provides the objective function and the gradient for the given \vec{x} .
 - 8: The optimization program *fmincon* starts.
 - 9: IPIT-CZL finishes the execution when *fmincon* provides a minimum.
-

Algorithm 2 [$f(\vec{x})$, $\vec{\nabla}f(\vec{x})$] = MyANSYSCall_ObjAndGrad(\vec{x})

- 1: [$f(\vec{x})$, $\vec{r}(\vec{x})$] = **Call** MyANSYSCall(\vec{x}). Invoke the subroutine MyANSYSCall.m to compute the objective function and the residual vector for the current CZ parameters stored in FileName.DesVar file.
 - 2: $J_r(\vec{x}) = []$. Clear the Jacobian matrix.
 - 3: Calculation of the sensitivities, first order information is obtained. Firstly the Jacobian is computed by FFD with the perturbations defined in the vector $\delta\vec{x}$ and then gradient is calculated.
 - for:** DVNo = 1:nDesVar
 - 4: $\vec{x}(\text{DVNo}) = \vec{x}(\text{DVNo}) + \delta\vec{x}(\text{DVNo})$
 - 5: [$-$, $\vec{r}^{NEW}(\vec{x})$] = **Call** MyANSYSCall(\vec{x})
 - 6: $J(\vec{x})(: , \text{DVNo}) = (\vec{r}^{NEW}(\vec{x}) - \vec{r}(\vec{x}))/\delta\vec{x}(\text{DVNo})$
 - 7: $\vec{x}(\text{DVNo}) = \vec{x}(\text{DVNo}) - \delta\vec{x}(\text{DVNo})$
 - end**
 - 8: $\vec{\nabla}f(\vec{x}) = J_r(\vec{x})^T \vec{r}(\vec{x})$. Gradient is calculated.
 - 9: $f(\vec{x})$ and $\vec{\nabla}f(\vec{x})$ are read, return to *fmincon*.
-

Algorithm 3 [$H(\vec{x})$] = HessianInterior(\vec{x} , ψ)

- 1: Global $J_r(\vec{x})$. This function, as the previous one, is handled by *fmincon* thus inputs and outputs are predefined and cannot be changed. Ideally, the Hessian matrix should be calculated in the previous subroutine where the sensitivities are computed however, *fmincon* for the interior point algorithm is not design like that. Therefore, the Jacobian matrix is made accessible in this function by declaring it as a global variable.
 - 2: $H(\vec{x}) = J_r(\vec{x})^T J_r(\vec{x})$. Hessian is calculated.
 - 3: $H(\vec{x})$ is read, return to *fmincon*.
-

Algorithm 4 $[f(\vec{x}), \vec{r}(\vec{x})] = \text{MyANSYSCall}(\vec{x})$

- 1: The dependent parameters to fully describe the CZ law are calculated by calling the CZparameters.m subroutine: $[nn, K, Delta, Tau] = \mathbf{Call} \text{ CZparameters}(\vec{x}_0)$. Wherein nn is the number of line segments used in the CZ law, K is the penalty stiffness for the onset traction, $Delta$ and Tau are vectors containing the separations $\delta_3^{(i)}$ and tractions $\sigma_3^{(i)}$ defining the CZ law for $i = 1$ to nn .
 - 2: **Call** WriteDesVar(*FileName*, nn , K , $Delta$, Tau). The ANSYS file *FileName.DesVar* storing the design variables and dependent parameters is created by invoking WriteDesVar.m. *FileName.DesVar* is imported by the main ANSYS macro file *FileName.DAT*.
 - 3: **Call** LoadStepFiles(*FileName*). This function generates the load steps used in the FEA, which correspond to the equilibrium points used in the comparison with experimental data.
 - 4: Perform the FEA by executing the ANSYS batch file.
 - 5: $[flg] = \mathbf{Call} \text{ ReadMonitor}(\text{FileName.mntr})$. Scan the monitoring file *FileName.mntr* and active the flag flg if the analysis fails to converge.
 - 6: **if** $flg = 1$, **then** an error message is shown to the screen and IPIT-CZL stops.
 - 7: $[\Psi^{Num}(\vec{x})] = \mathbf{Call} \text{ ReadOutputs}(\text{'ResultFile.txt'})$. The results from the FEA are stored in a file called *ResultFile.txt*. ReadOutputs.m extracts the numerical response and saves it in two columns of the matrix $\Psi^{Num}(\vec{x})$. E.g. for a DCB under pure rotation the first column corresponds to the end-beam rotation and the second to the moment.
 - 8: $[\Psi^{Exp}] = \mathbf{Call} \text{ ReadOutputs}(\text{'ResultFileExp.txt'})$. Idem for the experimental data.
 - 9: As the global responses come in discrete points, the numerical and experimental curves need to be compared at the same locations. To do so, the experimental data is linearly interpolated. The interpolated values are stored in the matrix Ψ_{Int}^{Exp} .
 - 10: $\vec{r}(\vec{x}) = \Psi^{Num}(\vec{x})[:, 2] - \Psi_{Int}^{Exp}[:, 2]$. The discrepancy between the numerical and the experimental responses is stored in the residual vector $\vec{r}(\vec{x})$.
 - 11: $f(\vec{x}) = \frac{1}{2} \sum_{l=1}^m r_l^2(\vec{x})$. IPIT-CZL uses a least squares formulation of the objective function.
 - 12: **Call** PlotResponse(\vec{x} , $f(\vec{x})$). A graph is created in order to visualize the current discrepancy between the global responses.
-

Assessment of Delamination

5.1 Experimental Setup

A test rig is developed at Aalborg University for performing delamination experiments on coupon test specimens. The description of this experimental setup is already given in a previous report [Jensen and Martos, 2016] by the same authors as this report, but is included here also for completeness and guidance for new readers. Tests are performed on DCB specimens subjected to pure moment loading. An illustration of the test specimen is shown in Fig. 5.1a. In the current experiment, pure mode I crack opening is considered, meaning that the moment ratio $M_1/M_2 = -1$. The specimens are UD glass fiber-epoxy laminates with a pre-crack of length a_0 introduced during the lay-up process. Length, width and thickness dimensions of the test specimen are gathered in Tab. 5.1. Young's modulus in the x-direction (specimen longitudinal direction) is measured from a three-point bending test. The remaining material properties are found in material data books, and is given later on. For now, only E_{xx} is considered.

Specimen No.	Length L [mm]	Width b [mm]	Thickness 2t [mm]	Initial crack length [mm]	E_{xx} [MPa]
0deg - 1	273.0	24.8	9.0	66.0	21.4×10^3
0deg - 2	273.0	24.9	9.0	66.0	21.4×10^3
0deg - 3	273.0	24.9	9.0	66.0	21.4×10^3
0deg - 5	273.0	24.6	9.0	66.0	21.4×10^3

Table 5.1: Geometric and material properties for the test series.

The test rig is driven by a tensile testing machine Zwick Z100/TL3S at a constant speed of 5 mm per minute. The rig consists of a pulley-system with a single string that goes around the whole system twice. The system is illustrated in Fig. 5.1c. The force is transmitted from the Zwick machine into four strings which travels through the system and reach the moment arms, as also seen in Fig. 5.1b. Four strings with two roller-pairs reach each moment arm, hence the force couple M applied to the DCB specimen arms are given in Eq. (5.1.1):

$$M = \frac{1}{2} F_{Zwick} d \cos(\varphi) \quad (5.1.1)$$

Where the parameters d and φ are shown in Fig. 5.1d, which shows the geometry and the resulting couple at each moment arm. The parameter d is the distance between the edges of the roller-pairs and is measured to be $d = 121\text{mm}$. The parameter φ is the angle of a moment

arm. It is noted that F_{Zwick} always acts vertically, hence the cosine is needed when calculating the resulting couple, as only the projection of F_{Zwick} onto the perpendicular direction of the moment arm contributes to M . The angle(s) (φ for each moment arm) are measured by inclinometers in absolute value.

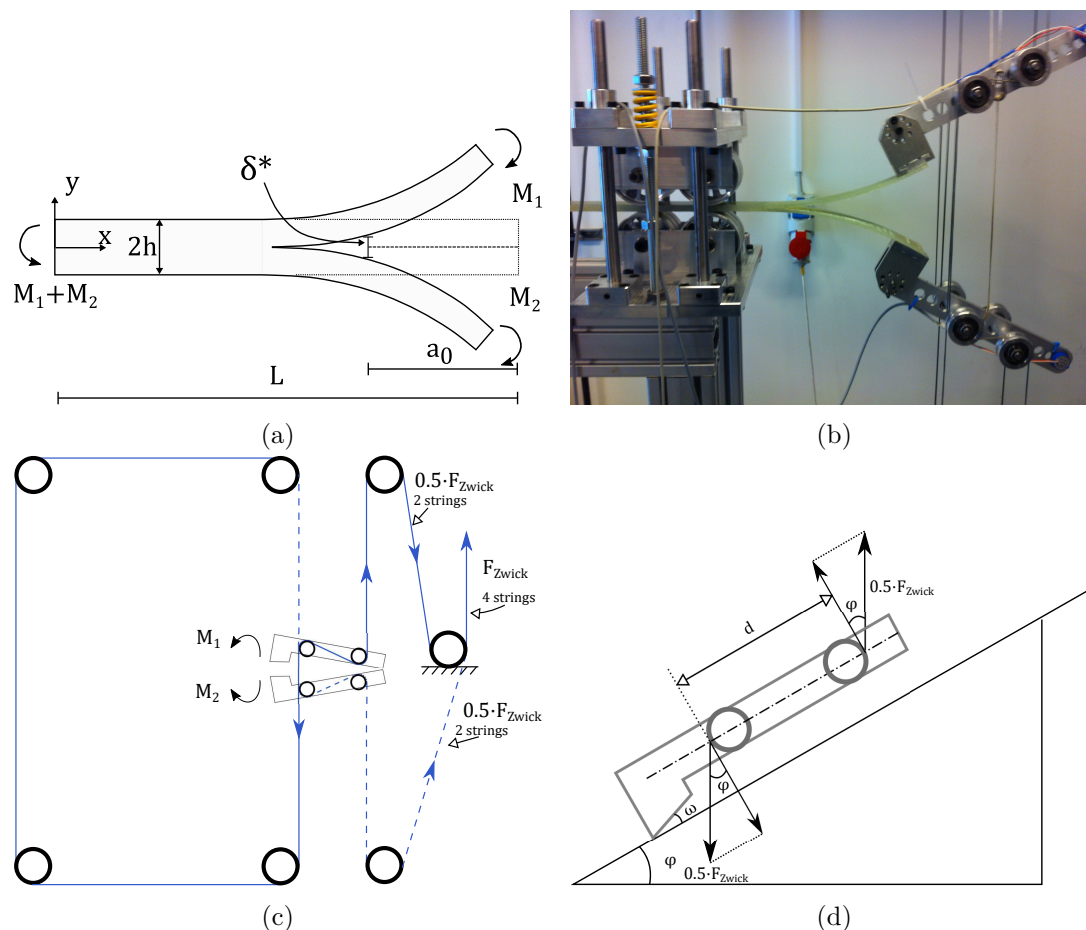


Figure 5.1: (a) Illustration of DCB specimen under pure moment loading (b) Real experimental set up of the DCB specimen and moment arms (c) Pulley system and connection to Zwick tensile testing machine (d) A single moment arm, its orientation and the resulting force couple.

The weight of the moment arms are counter balanced by weights to ensure no shear forces are introduced to the DCB specimen. Low friction roller bearings support the specimen, which should be aligned with respect to the moment arms. Any misalignment would disturb the measurement by introducing unexpected mode mixity. The moment arms are tightly fixed to the surface of the specimen through a screw/drilled thread connection as shown in Fig. 5.2a. The crosshead displacement of the tensile testing machine and the applied force F_{Zwick} are monitored together with the angles φ during the experiment. Additionally, a clip gauge is attached to two pins located at the initial crack tip as shown in Fig. 5.2b. The clip gauge provides a local measure being directly related to the interfacial separations. This clip gauge monitors the separation at the initial crack tip which is denoted the end opening separation δ^* as illustrated in Fig. 5.1a.



Figure 5.2: (a) Moment arms grips. (b) Clip gauge mounted in the test set up.

5.1.1 Experimental Results

The experimental data shown here has been provided by the supervisors of this project. The output from the experiment is the end opening separation, two force and two angle measurements - one associated with each moment arm. The force couple M is calculated from Eq. (5.1.1). The resulting force couple and angle for the upper and lower moment arm should ideally be equal. The data for the upper moment arm is considered in the following. Fig. 5.3a and 5.3b shows graphs of moment per width versus end opening separation and angle of rotation, respectively, for the test specimens presented in Tab. 5.1.

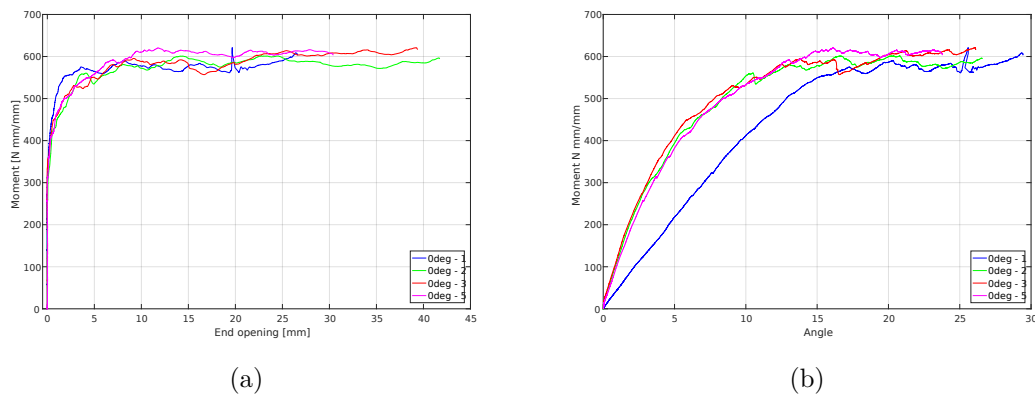


Figure 5.3: Global structural responses: (a) Applied moment versus end opening separation δ^* (b) Applied moment versus angle of rotation

Note that the data for the 0deg - 1 specimen is considerably different from the other tests, hence this is not chosen as the data set for testing IPIT-CZL. Among these curves, the data for the 0deg - 5 test is utilized and is considered a reliable data series, since similar responses for two other test specimens are observed.

5.2 Finite Element Model

IPIT-CZL is based on comparing outputs from a physical experimental and a simulated experiment. The experiment is simulated numerically by using the FEM. The FE model is crucial to IPIT-CZL since the methodology relies on minimizing a residual in structural response between the numerical model and the physical experiment. Consequently the quality of the FE model directly reflects the final characterization of the CZ parameters. This section describes the FE model with main focus on the elements utilized, the construction of a proper mesh, load introduction, and model mismatches between the physical experiment and numerical model.

The software used is ANSYS v. 17.2 MAPDL. The numerical model is written in MAPDL language and consists of two macro files: A *.DAT file which defines the preprocessing steps and sets up the solution settings. Specifically, the *.DAT file defines the model geometry, specimen material, boundary conditions, element technology, mesh and specifies settings for the Newton-Raphson solver. The CZ parameters are read from the *.DESVAR file. The second macro file is a *.MAC file which performs the post processing steps and writes model outputs to text files which are later used as input for IPIT-CZL.

The DCB specimen is UD glass fiber epoxy laminate, and is modelled as an orthotropic material with elastic constants as given in Tab. 5.2. It is noted that only the stiffness constant E_{xx} is measured experimentally from a three-point bending test, while the remaining properties are taken from an exercise session for a PhD course at Aalborg University using the same materials.

E_{xx}	E_{yy}	E_{zz}	ν_{xy}	ν_{yz}	ν_{xz}	G_{xy}	G_{yz}	G_{xz}
[GPa]	[GPa]	[GPa]	[-]	[-]	[-]	[GPa]	[GPa]	[GPa]
21.4	10	10	0.3	0.07	0.3	4	2.5	4

Table 5.2: Material properties used in the FE model presented in this section.

In the physical experiment a DCB specimen is loaded by pure moments resulting in a pure mode I crack opening, while end-opening separation, rotations of DCB arms, crosshead displacement and the applied force couple are monitored. The numerical model is displacement-controlled and the loading is introduced by prescribing equally and opposite rotations at the end of the two DCB arms. There is a mismatch in the specimen geometry between the numerical model and the physical experiment. This is attributed to the way the load is introduced in the experiment. The difference is illustrated in Fig. 5.4a and 5.4b. The real dimensions of the DCB specimen is given in Tab. 5.1. However, some geometric modifications are done when modelling the DCB specimen in a numerical environment for several reasons. Firstly, the specimen is initially modelled as a unit width (1.0mm) specimen which obviously is different from the real 24.6 mm. This is due to the computational cost of having a model of full width when every function evaluation in IPIT-CZL requires running a FE simulation. Eventhough symmetry can be taken into account, it is still computationally costly. The influence of the unit width assumption is elaborated on after the CZ parameters has been characterized using IPIT-CZL based on a unit width model.

Secondly, the effective length of the DCB arms must be reduced a distance a_0^* in the numerical model since the moments are not applied at the real DCB arm ends. The parameter a_0^* is measured to be $a_0^* = 47$ mm with a tolerance of approximately ± 5 mm since there is no clear indication of where the DCB arm starts deflecting and is unaffected by the presence of the moment arm grippers. The effective length of the specimen in the numerical model

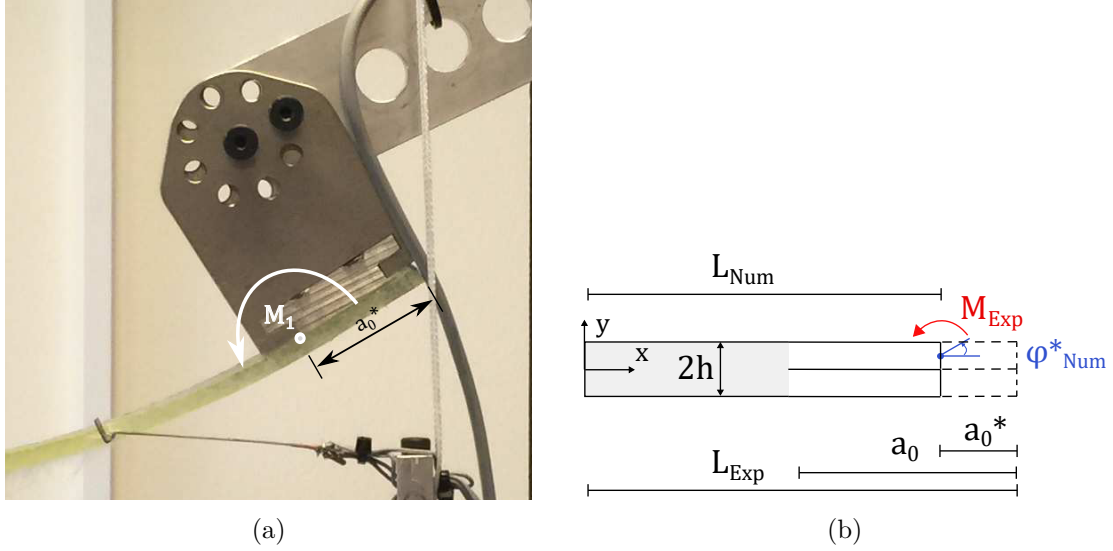


Figure 5.4: Geometric differences between the experiment and the numerical simulations, due to the moment introduction in the specimen.

is then calculated as $L_{Num} = L_{Exp} - a_0^*$. Similarly, the initial crack length of the numerical model should be adjusted as: $a_0^{Num} = a_0 - a_0^*$. The compliance of the DCB specimen depends on the initial crack length, the compliance increases with increasing a_0 . Note, however, that the specimen compliance decreases with increasing a_0^* . Hence, the a_0^* parameter is important to be able to make the numerical and experimental structural responses agree. The a_0^* parameter is adjusted by comparing the initial linear elastic response, before any opening at the initial crack tip, of the numerical model and the physical experiment. The final value is determined to be $a_0^* = 42.0\text{mm}$, hence $a_0^{Num} = 66.0\text{mm} - 42.0\text{mm} = 24.0\text{mm}$, and $L_{Num} = 273.0\text{mm} - 42.0\text{mm} = 231.0\text{mm}$.

The FE model contains two element types: One type for modelling the DCB specimen bulk material, and one type for modelling the potential crack path along the DCB arm interface. The element type for modelling the DCB specimen is the 3D 8-noded linear SOLID185 element with the enhanced assumed strain (EAS) option, being computationally less expensive than the quadratic elements. The EAS option is a necessity to avoid parasitic shear which else would develop when using linear elements in a bending dominated deformation. A predefined crack path is built along the interface between the DCB arms. This interface is modelled using the user-defined interface elements.

The CZ parameters are controlled by MATLAB. The stiffness of the interface elements before the interfacial separations exceeds its critical point and material softening starts, are given by the penalty stiffness parameter $K^{(eq)}$, which is chosen to be equal for all three directions. The penalty stiffness $K^{(eq)}$ should be large enough to provide reasonable pre-crack stiffness, hence it should not add too much artificial compliance for pre-crack situations. But at the same time, it should be small enough to avoid numerical problems such as spurious traction oscillations in the FE analysis. The value is set to $K^{(eq)} = 10^5 \text{ N/mm}^3$ as recommended in [Bak et al., 2014].

The mesh density is non-uniform throughout the FE model. The mesh is categorized as being either coarse or fine depending on whether crack growth is expected in the region or not. The mesh of the FE model is shown in Fig. 5.5. A potential fracture process zone is identified and has a fine mesh with element sizes of $0.25\text{mm} // 0.5\text{mm} // 2.25\text{mm}$ in the

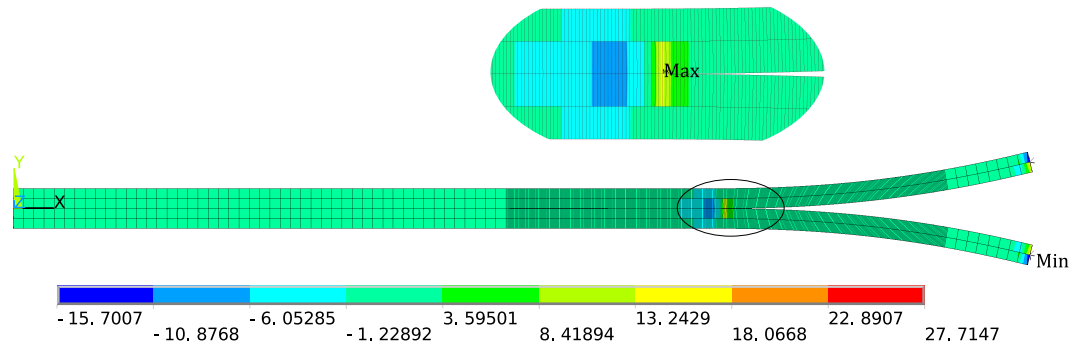


Figure 5.5: DCB model under pure bending, nodal solution, σ_y , corresponding to the last substep ($\varphi = 16.3^\circ$). The end at the left hand side is fixed.

length // width // height directions respectively. In the regions of a coarse mesh no crack growth is expected to take place, and here the element dimensions are 2.26mm // 0.5mm // 2.25 mm. The mesh in the potential fracture process zone is refined sufficiently such that no convergence problems for the FE model will arise, and the solution quality is independent of the mesh. It has been reported in [Hansen et al., 2009], that the crack tip region of the cohesive should be discretized by at least three elements, which is ensured in this FE model.

The loading is introduced by prescribing rotations at the DCB arm ends as illustrated in Fig. 5.4b. Since the FE model is constructed using linear solid elements, having no rotational degrees of freedom, it is necessary to use multi-point constraint techniques to apply the rotational loading. The loading is applied quasi statically with a final rotation of each DCB arm of 16.3° in absolute value. In the FE model, the specimen is fixed at its left end even though this is not the real support according to the experiment. However, in case of pure mode I crack opening, $M_1 = -M_2$, so no boundary conditions are in theory needed since the applied moments self-equilibrate each other. Nevertheless the left end is simply fixed, since else the FE model complains about insufficient boundary conditions and possible rigid body motion. Postprocessing of FE results show that reaction loads at the fixed end are negligible anyway.

5.3 Design Problem Formulation for Multilinear CZ Law

Having presented the structure of IPIT-CZL and preliminary studies of its performance for the simple case of a bilinear CZ law, a multilinear CZ law is now considered. Recalling Sec. 4.2 the objective function is defined as shown in Eq. (5.3.1):

$$\min_{\vec{x}} f(\vec{x}) = \frac{1}{2} |\vec{r}(\vec{x})|^2 = \frac{1}{2} \sum_{l=1}^m r_l^2(\vec{x}) \quad (5.3.1)$$

Being a least squares formulation of the residual vector \vec{r} . The residual describes the discrepancy in global structural response obtained from a finite element model and a physical experiment. These data of moment versus angle of rotation, as discussed in Sec. 5.2. The design variables \vec{x} are CZ parameters. As illustrated in the introductory example with a bilinear CZ law, various parameters for determining the CZ parameters are available. Previously the critical energy release rate and the onset traction were chosen as design variables which completely defined the shape of the CZ law.

For the current problem a multilinear CZ law, as shown in Fig. 5.6, is used to model delamination in a pure moment loaded DCB specimen under pure mode I crack opening. It is chosen to fix the discrete separation points $\delta_3^{(i)}$ and have tractions $\sigma_3^{(i)}$ as design variables. The onset traction is fixed at 30 MPa, which corresponds to 80% of the out of plane strength of the epoxy matrix material which is considered to be a reasonable estimate of the onset of interfacial damage as a rule of thumb. The last traction is naturally set to zero $\sigma_3^{(n)} = 0$ MPa. The number of line segments included in the multilinear CZ law is directly related to the number of design variables. For a n -order multilinear law there will be a total of $n - 2$ design variables, as shown in \vec{x} :

$$\vec{x} = [\sigma_3^{(2)} \ \sigma_3^{(3)} \ \dots \ \sigma_3^{(n-1)}]^T \quad (5.3.2)$$

The objective of IPIT-CZL is to determine the shape of the CZ law. However, the constitutive model is restricted to be piecewise linear which imposes artificial constraints on the shape of the CZ law. Nevertheless, these constraints are less restrictive than alternative CZ law shapes e.g. bilinear, trilinear, trapezoidal, exponential ect. proposed by [Turon et al., 2006], [Hansen and Lund, 2009], [Tvergaard and Hutchinson, 1992], and [Goyal-Singhal et al., 2004] respectively.

Usually more line segments are needed in the crack tip region of the CZ law compared to the bridging region. The idea is similar to creating a refined mesh in regions of high stress gradients in a structural finite element context and having a more coarse mesh in regions of low stress gradients. The proper placement of the fixed separation points δ_i requires physical insight to the problem at hand, but can often be guided by elaborating on the experimental data available. Nevertheless, they are to some extent subjectively chosen. This is discussed further in the next section.

The subjectively selected placement of the separations $\delta_3^{(i)}$ should be reconsidered when a solution has been obtained, one should consider if the final shape of the CZ law is realistic, and how well the structural response is represented by the numerical model. Additionally, a post optimality sensitivity study of the placement of the discrete separation points could be performed. The CZ parameters for the problem at hand is shown in Tab. 5.3.

The design space is bounded by upper and lower limits, ensuring that no design variable is less than zero nor greater than the onset traction of $\sigma^{(1)} = 30$ MPa respectively. Initial

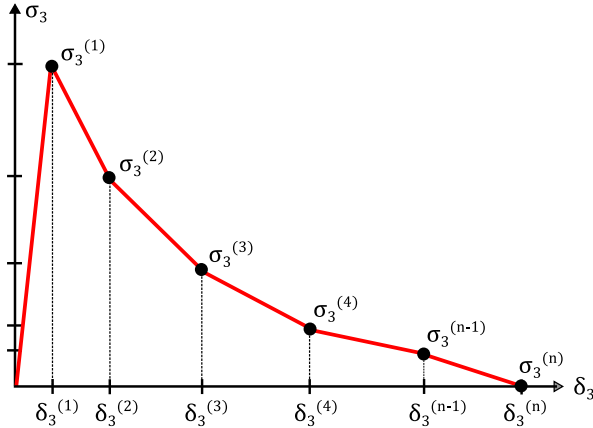


Figure 5.6: Multilinear CZ law for pure mode I crack opening

Pnt. Nr i:	$\delta_3^{(i)}$ [mm]	$\sigma_3^{(i)}$ [MPa]
(1)	3.0E-04	30
(2)	0.0100	x_1
(3)	0.0200	x_2
(4)	0.0300	x_3
(5)	0.0400	x_4
(6)	0.0500	x_5
(7)	0.0600	x_6
(8)	0.0800	x_7
(9)	0.1000	x_8
(10)	0.2000	x_9
(11)	0.5000	x_{10}
(12)	1.0000	x_{11}
(13)	3.0000	x_{12}
(14)	5.0000	x_{13}
(15)	9.0000	0

Table 5.3: Parameters and DV for 15'th order multilinear CZ law

studies of IPIT-CZL with a multilinear CZ law suggests putting up constraints on the design variables to make sure that the CZ law is monotonically decreasing, that is, ensuring the CZ law is always a material softening law. This is convenient since small and non-physical oscillations in the CZ law has been observed in some of the initial tests. The constraints are implemented as linear inequality constraints through A and \vec{b} , defined such that e.g. $A\vec{x} \leq \vec{b}$, and:

$$x_1 \leq x_2 \leq x_3, \quad x_2 \leq x_3 \leq x_4 \quad \dots \quad (5.3.3)$$

One should be cautious in imposing such constraints without any physical insight to the problem at hand. During delamination, various failure mechanisms coexists in the fracture process zone, and can be of different length scales too. Failure mechanisms in the crack tip region are usually governed by plasticity, viscoelastic deformation and matrix micro cracking, while fiber-bridging will occur in the wake of the crack tip.

Two different fiber-bridging mechanisms are commonly encountered in composite materials: Crack bridging by frictionally restrained long fibers oriented perpendicular to the crack plane and crack bridging by fibers oriented parallel to the crack plane, denoted as cross-over fiber-bridging [Sørensen and Kirkegaard, 2006]. In case of frictionally restrained fiber-bridging, the normal components of interfacial tractions and separations are related through $\sigma_3 \propto \sqrt{\delta_3}$ [Sørensen and Kirkegaard, 2006]. However, micro-mechanical models in [Spearing and Evans, 1992] suggests an inverse proportional relation between normal components of interfacial tractions and separations in case of cross-over fiber bridging: $\sigma_3 \propto 1/\sqrt{\delta_3}$. Therefore, the constraints on the design variables should only be imposed if no potential failure mechanisms are omitted by erroneous constraints. The fiber-bridging occurring in test specimens under consideration in this report are solely of the cross-over bridging type. Consequently the inequality constraints in Eq. (5.3.3) can be implemented and still adequately model fiber bridging.

Stopping tolerances for the optimization algorithm are yet to be determined. They constitute an optimality tolerance and a step tolerance. The former is a termination tolerance for the gradients and is set equal to its default value of 1e-6. The latter is a termination tolerance on the step size.

The step tolerance is of primary importance for the current optimization problem. A lot of tests have been conducted in order to determine appropriate the step tolerances. It is found to be convenient to have two values of the step tolerance; a rough value of $\epsilon_R = 1e - 4$ and a fine value of $\epsilon_F = 1e - 5$. The idea of using two stopping tolerances is to use ϵ_R as an initial stopping tolerance to find a converged solution in the neighbourhood of an optimum, and subsequently restart the optimizer from this point using a finer stopping tolerance ϵ_F to obtain a better optimum point.

It is noted, that the step tolerance seems small compared to the expected accuracy of the CZ law to be characterized. However, these are chosen from a lot of tests and seems as a fine compromise. Larger values makes the optimizer stop prematurely, while smaller values makes the optimizer search for a minimum for too many iterations.

5.3.1 Setting Up CZ Parameters for IPIT-CZL

In this section, further it is elaborated further on proper placement of $\delta_3^{(i)}$ in the multilinear CZ law for use in IPIT-CZL. The experimental data are used as guidance, together with a brief discussion of the J-integral. For a DCB specimen loaded by pure moments M_1 and M_2 as shown in Fig. 5.1a, the path independent J-integral can be calculated with the following equation under plane stress conditions [Sørensen and Kirkegaard, 2006]:

$$J = \frac{21(M_1^2 + M_2^2) - 6M_1M_2}{4b^2t^3E} \quad (5.3.4)$$

For this to be applicable, it is further assumed that the distances from the beam ends to the fracture process zone are greater than few times the beam height, such that the stress states at the beam ends are unaffected by the stress field around the fracture process zone; leaving the beam in a state of pure bending [Sørensen and Kirkegaard, 2006]. This is the case with the current specimen geometry since $2t = 9.0\text{mm}$ and $a_0 = 66.0\text{mm}$. Additionally, it is assumed that the specimen is made of a homogeneous and isotropic material. In case of pure mode I crack opening, $M_1 = -M_2 = M$, the expression above reduces to the following:

$$J = \frac{12M^2}{b^2t^3E} = CM^2 \quad (5.3.5)$$

Where C is a compliance constant. Hence the J-integral is directly proportional to the applied moment squared: $J \propto M^2$. This means, that the curves of moment versus end opening separation in Fig. 5.3a actually also suggests the shape of the R-curve, that is the fracture resistance J as function of the end opening separation δ_3^* . A zoom-in of the end opening versus moment curve is shown in Fig. 5.7.

Another important and widely used relation for plane problems is derived in [Sørensen and Kirkegaard, 2006], and is shown here in case of pure mode I crack opening, under the assumption that J is a potential function, i.e. independent of the path opening history:

$$\sigma_3(\delta_3^*) = \frac{\partial J(\delta_3^*)}{\partial \delta_3^*} \quad \text{Or equivalently} \quad J = \int_0^{\delta_3^*} \sigma(\delta_3) d\delta_3 \quad (5.3.6)$$

Even though its application is restricted to several assumptions, it gives a guidance of an underlying and convenient relation between CZ parameters and global structural responses. This can be used for guidance when formulating the design problem. A straight forward utilization of this relation is to place the final separation value $\delta_3^{(n)}$ where $\sigma_3 = 0.0$. This occurs when the J-curve attains its steady state - hence the final separation point $\delta_3^{(n)}$ can be estimated as the end opening separation where the plateau begins in Fig. 5.3a. For this

reason $\delta_3^{(15)} = 9.0\text{mm}$ in the Tab. 5.2.

Additionally, more line segments are needed in regions where a linear representation of the CZ law is insufficient. This could be elegantly formulated in terms of higher order derivatives of the $J(\delta_3^*)$ curve, provided that a smooth curve fit of the data is available. However, such an involved procedure is not necessary here. Recalling the integral relation of Eq. (5.3.6) and considering the R-curve related behaviour in Fig. 5.7, an integrated effect from $0.0 < \delta_3 \leq 1.0\text{mm}$ makes the moment curve shape change significantly in this region. Hence more line segments are added in this separation range, as also seen from the table in Tab. 5.2.

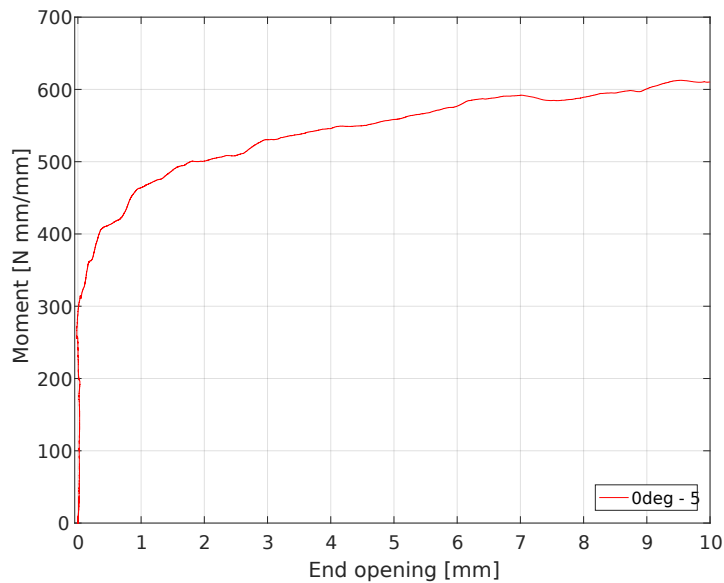


Figure 5.7: Zoom in: End opening separation versus moment per width for test specimen 0deg - 5.

5.4 Assessment of Delamination with IPIT-CZL

This section includes the results obtained for the test specimen 0deg - 5. As mention in Sec. 5.3, 13 out of 15 tractions are the design variables included in \vec{x} .

Initial testing of IPIT-CZL revealed a reasonable solution, which is used as a reference CZ law in this section. The reference CZ law is shown in Fig. 5.8 and Fig. 5.9. The separation axis δ_3 is split into two parts for illustration purposes: A near crack tip (NCT) region ranging from [0.0; 0.1]mm and a far bridging (FB) region in the range of [0.2; 9.0]mm.

It is decided to run IPIT-CZL with four initial guesses, which have been chosen based on the reference CZ law. The initial guesses are shown together with the reference CZ law in Fig. 5.8 and Fig. 5.9. The first initial guess, IG1, is a CZ law whose crack-tip and bridging energy¹ are larger than those from the reference. IG2 has the crack-tip energy larger but bridging energy smaller, IG3 has smaller crack tip energy but larger bridging energy and IG4 both crack-tip and bridging energy are smaller than the reference CZ law. It is noted, that these comparisons of crack tip and bridging energy are only approximate, since there is no clear border between the crack tip and bridging zone. With these initial guesses, it is aimed to observe the behaviour of the numerical simulations and the optimization progress towards the optimum point. The global structural responses corresponding to the reference and initial guess CZ laws are depicted in Fig. 5.9. The initial guess CZ laws and their corresponding critical energy release rate, are also gathered in Tab. 5.4.

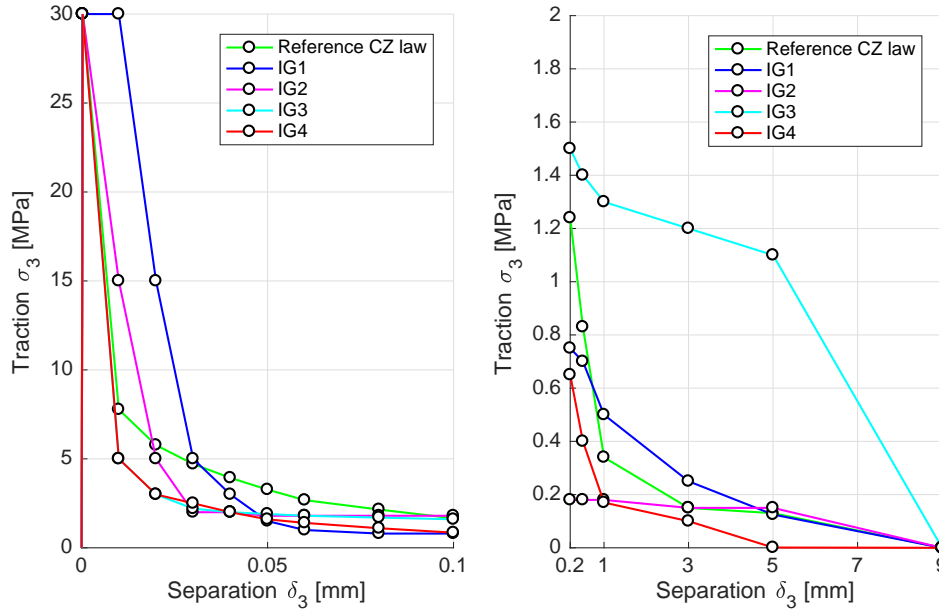


Figure 5.8: CZ laws of the reference set and all the initial guesses IG1-4. Left: NCT region. Right: FB region.

To exemplify the performance of IPIT-CZL, initial guess IG3 is considered in more detail. IPIT-CZL is started with a step tolerance of ϵ_R , and converges to an optimum point after 78 iterations. Thereafter, IPIT-CZL is restarted from the optimum point with a step tolerance of ϵ_F and after another 33 iterations, IPIT-CZL arrives at a final CZ law for IG3.

The evolution of the optimization process is presented in Fig. 5.10 and Fig. 5.11. Major changes occur within the first 6 iterations and after 12 iterations the global structural response can be considered well represented. Until the 78th iteration, minor reductions in the

¹Recall from previous sections, that the fracture energy is directly related to areas under the traction-separation curve.

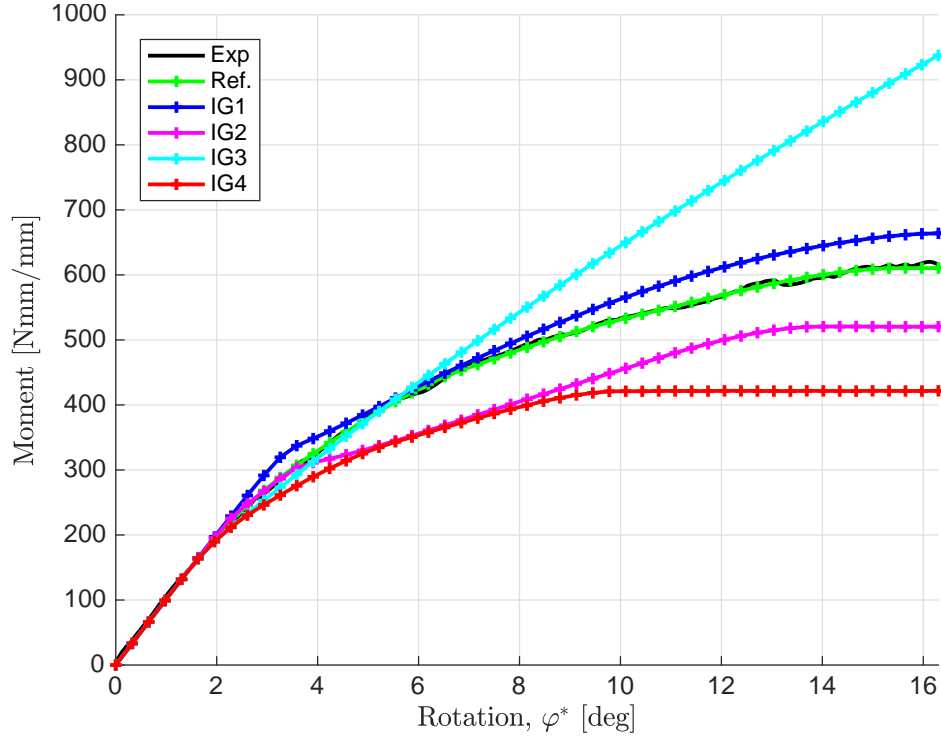


Figure 5.9: Global structural responses of the reference CZ law and all the initial guesses.

objective function and minor changes in the CZ law is observed. Thus, one could suggest increasing the stopping tolerances to obtain a reasonable solution in less iterations, specially if the uncertainties related to the experimental data are considered (e.g. the fiber misalignment, the dimensions of the specimen, the location/modeling of the force introduction, etc.) Nonetheless, that will make IPIT-CZL stop prematurely in some cases, as it has been experienced.

ID n.	Initial guess, \vec{x}_0													G_c [$\frac{kJ}{m^2}$]
	[MPa]													
IG1	[30.000	15.000	5.000	3.000	1.500	1.000	0.800	0.800	0.750	0.700	0.500	0.250	0.125]	2.700
IG2	[15.000	5.000	2.000	2.000	1.800	1.800	1.800	1.800	0.180	0.180	0.180	0.150	0.150]	1.526
IG3	[5.000	3.000	2.200	2.000	1.900	1.800	1.700	1.600	1.500	1.400	1.300	1.200	1.100]	8.632
IG4	[5.000	3.000	2.500	2.000	1.600	1.400	1.100	0.850	0.650	0.400	0.170	0.100	0.001]	1.090

Table 5.4: The four initial guesses used.

The results obtained for all initial guesses IG1-4 are collected in two tables, the information regarding the performance of the optimization algorithm is included in Tab. 5.5 and the converged solutions are gathered in Tab. 5.6. An identification code (ID n.) is used to distinguish the solutions, e.g. for the initial guess 1: IG1 is the initial CZ law, CIG1 is the converged CZ law based on the rough step tolerance ϵ_R , and CIG1R is the converged CZ law after restarting IPIT-CZL from the previously obtained optimum point using a fine step tolerance ϵ_F . In the solutions provided by the ϵ_R , there is a good agreement in the critical energy release rate as shown in Tab. 5.6. However, there are some clear differences between the obtained CZ laws and global structural responses as depicted in Fig. 5.13a and Fig. 5.12a, respectively.

The principal discrepancies in the CZ laws are seen in the NCT region Fig. 5.12a, whilst, the CZ laws in the FB region have similar shape. Regarding the structural response in Fig. 5.13, there is a good agreement of all solutions with the experimental data, except in the

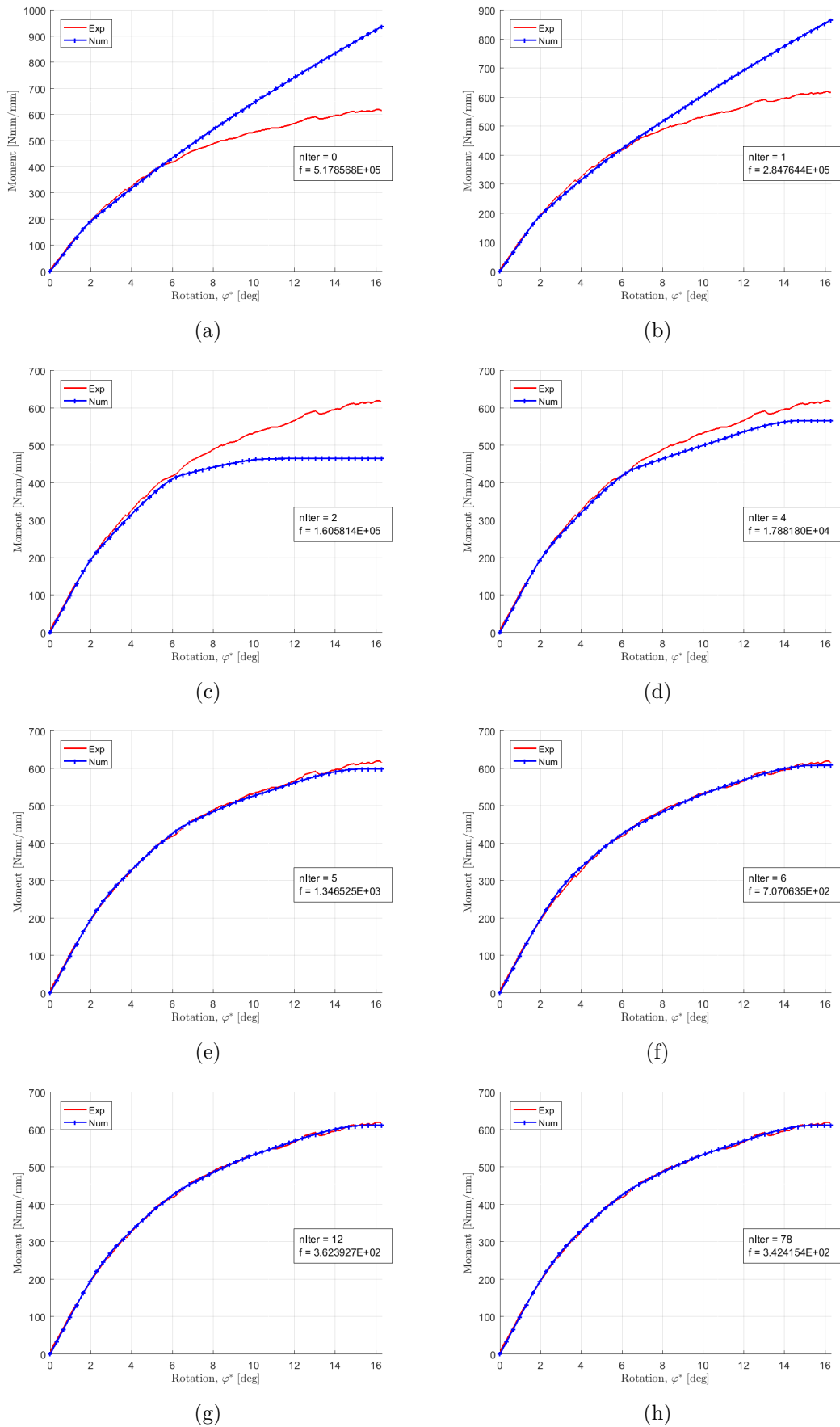
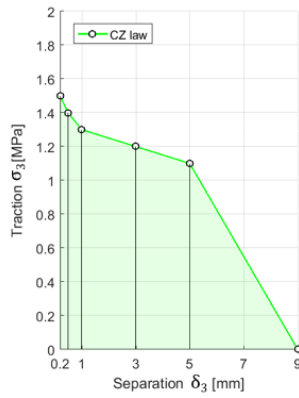
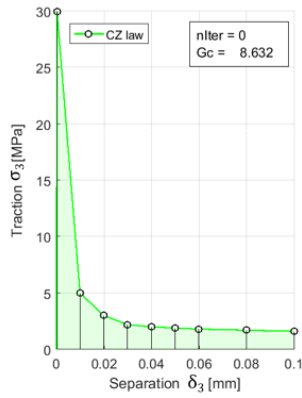
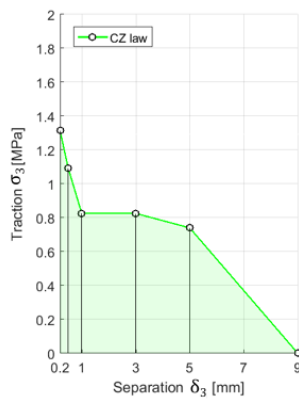
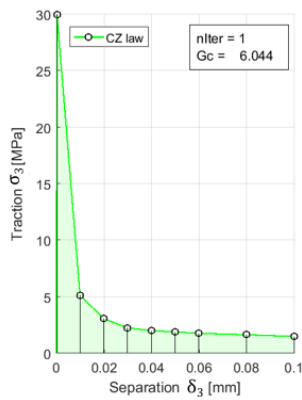


Figure 5.10: Evolution of the global structural response for the execution IG3. (a) Initial guess (b) through (g) 1'st to 6'th iteration (h) converged solution.



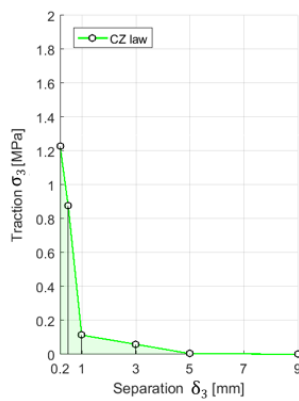
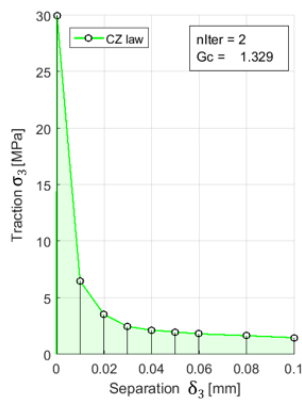
	Separation	Traction
Pnt. Nr. 1	3.0000e-04	30
Pnt. Nr. 2	0.0100	5
Pnt. Nr. 3	0.0200	3
Pnt. Nr. 4	0.0300	2.2000
Pnt. Nr. 5	0.0400	2
Pnt. Nr. 6	0.0500	1.9000
Pnt. Nr. 7	0.0600	1.8000
Pnt. Nr. 8	0.0800	1.7000
Pnt. Nr. 9	0.1000	1.6000
Pnt. Nr. 10	0.2000	1.5000
Pnt. Nr. 11	0.5000	1.4000
Pnt. Nr. 12	1	1.3000
Pnt. Nr. 13	3	1.2000
Pnt. Nr. 14	5	1.1000
Pnt. Nr. 15	9	0

(a)



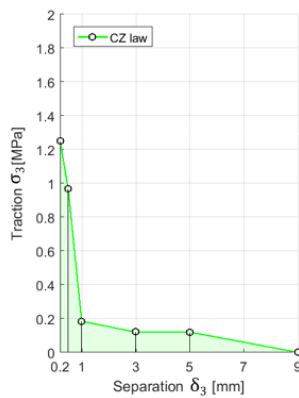
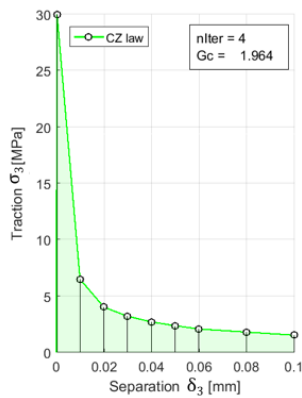
	Separation	Traction
Pnt. Nr. 1	3.0000e-04	30
Pnt. Nr. 2	0.0100	5.1350
Pnt. Nr. 3	0.0200	3.0656
Pnt. Nr. 4	0.0300	2.2380
Pnt. Nr. 5	0.0400	2.0093
Pnt. Nr. 6	0.0500	1.8889
Pnt. Nr. 7	0.0600	1.7663
Pnt. Nr. 8	0.0800	1.6367
Pnt. Nr. 9	0.1000	1.4906
Pnt. Nr. 10	0.2000	1.3133
Pnt. Nr. 11	0.5000	1.0930
Pnt. Nr. 12	1	0.8258
Pnt. Nr. 13	3	0.8253
Pnt. Nr. 14	5	0.7400
Pnt. Nr. 15	9	0

(b)



	Separation	Traction
Pnt. Nr. 1	3.0000e-04	30
Pnt. Nr. 2	0.0100	6.5000
Pnt. Nr. 3	0.0200	3.5388
Pnt. Nr. 4	0.0300	2.4541
Pnt. Nr. 5	0.0400	2.1435
Pnt. Nr. 6	0.0500	1.9713
Pnt. Nr. 7	0.0600	1.8085
Pnt. Nr. 8	0.0800	1.6452
Pnt. Nr. 9	0.1000	1.4649
Pnt. Nr. 10	0.2000	1.2282
Pnt. Nr. 11	0.5000	0.8768
Pnt. Nr. 12	1	0.1129
Pnt. Nr. 13	3	0.0588
Pnt. Nr. 14	5	0.0037
Pnt. Nr. 15	9	0

(c)



	Separation	Traction
Pnt. Nr. 1	3.0000e-04	30
Pnt. Nr. 2	0.0100	6.4968
Pnt. Nr. 3	0.0200	4.0208
Pnt. Nr. 4	0.0300	3.2048
Pnt. Nr. 5	0.0400	2.7027
Pnt. Nr. 6	0.0500	2.3683
Pnt. Nr. 7	0.0600	2.0741
Pnt. Nr. 8	0.0800	1.8005
Pnt. Nr. 9	0.1000	1.5270
Pnt. Nr. 10	0.2000	1.2495
Pnt. Nr. 11	0.5000	0.9687
Pnt. Nr. 12	1	0.1838
Pnt. Nr. 13	3	0.1205
Pnt. Nr. 14	5	0.1201
Pnt. Nr. 15	9	0

(d)

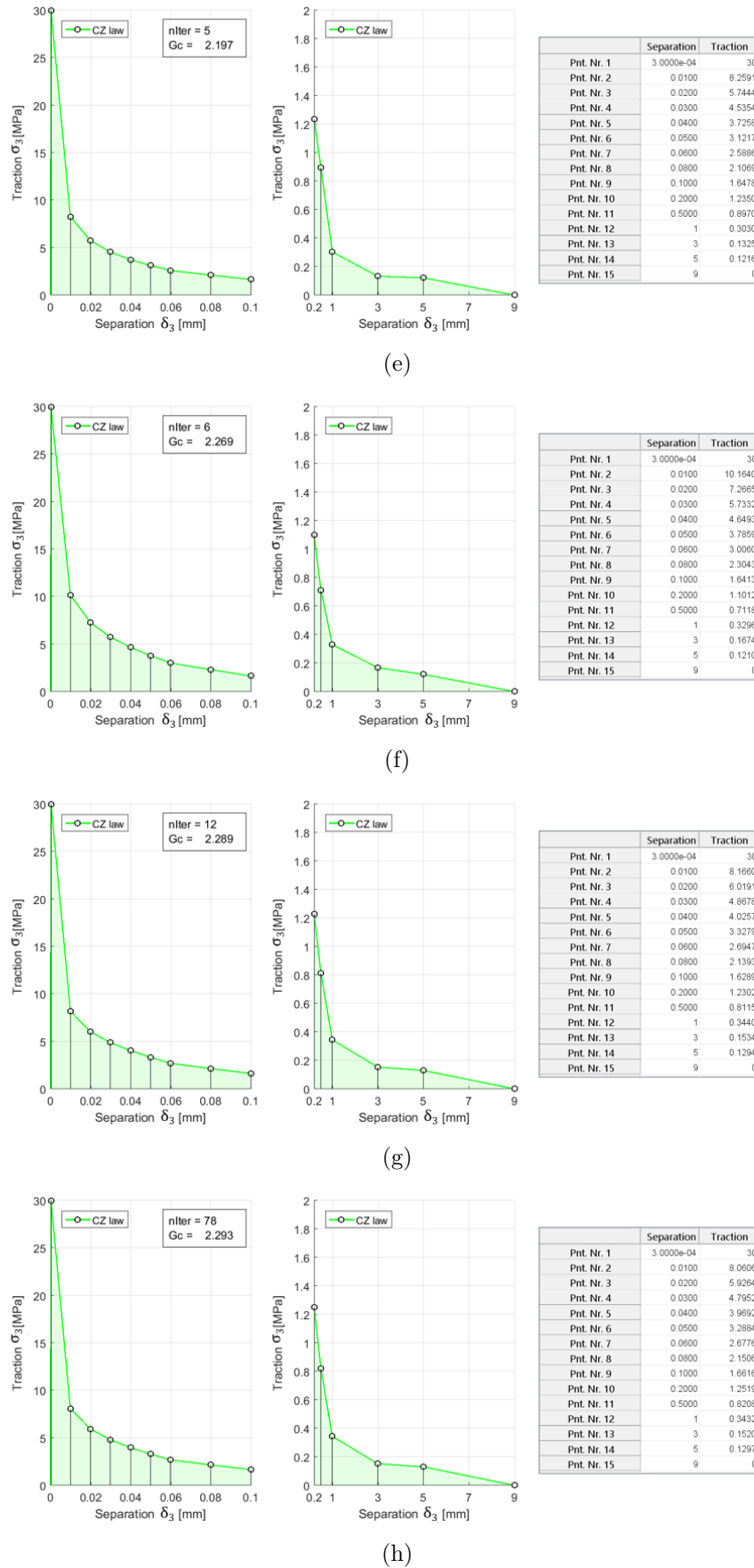


Figure 5.11: Evolution of the global structural response for the execution IG3. (a) Initial guess (b) through (g) 1'st to 6'th iteration (h) converged solution.

region $\varphi : [2^\circ; 5^\circ]$, being the transition between linear elastic and nonlinear response. The flat part at the end of the numerical curves may appear strange, but is due to the fact that the steady state fracture toughness has been reached. If the fiber-bridging was a smoother phenomenon, a clear horizontal line would be seen in the experimental curve, just as in the numerical simulations. Moreover, recalling Fig. 5.3b, a horizontal line can be insinuated at the end of the curve 0deg - 5, indicating a steady state response, with a moment value of $M \approx 600 \frac{Nmm}{mm}$ between angles of $\varphi \approx 14^\circ$ and $\varphi \approx 24^\circ$.

The differences between optimum solutions for all initial guesses IG1-4 vanish in the converged solution obtained after restarting IPIT-CZL using the finer step tolerance ϵ_F . All solutions converged to the same global structural response as shown in Fig. 5.13b, and the linear-nonlinear transition is no longer shown as a kink in the numerical models, but lies on top of the experimental curve. The same CZ law is consistently reached as illustrated in Fig. 5.12b. Additionally, special attention should be drawn to the critical energy release rate G_c in Tab. 5.6; all solutions converged to the same value of $G_c \approx 2.3 \text{ kJ}/m^2$.

ID n.	Number of Iterations	Number of f. evals.	Time [h m s]	Stopping criterion	$f(\bar{x})$
CIG1	28	406	21 h 57' 18.78"	Step size tolerance	656.43
CIG2	31	448	24 h 25' 31.09"	"	1502.00
CIG3	78	1106	72 h 34' 46.26"	"	342.42
CIG4	61	868	53 h 54' 25.48"	"	294.98
CIG1R	54	770	46 h 42' 2.22"	"	266.77
CIG2R	43	616	36 h 0' 50.28"	"	266.87
CIG3R	33	476	27 h 31' 33.38"	"	265.11
CIG4R	78	1106	68 h 29' 57.03"	"	265.04

Table 5.5: Results obtained from IPIT-CZL for the selected experiment with four initial guesses. Part I

ID n.	Converged Point, \bar{x}												G_c [$\frac{kJ}{m^2}$]	
	[MPa]													
CIG1	10.316	7.373	5.8149	4.6991	3.7824	2.9618	2.2308	1.5674	1.1013	0.7423	0.3387	0.16724	0.12217	2.293
CIG2	12.902	9.1663	7.1627	5.7115	4.5112	3.4207	2.4552	1.5658	0.95456	0.60921	0.33216	0.18393	0.11069	2.287
CIG3	8.0606	5.9264	4.7953	3.9692	3.2885	2.6776	2.1506	1.6617	1.252	0.82084	0.34326	0.15201	0.12979	2.293
CIG4	7.5081	5.4784	4.4383	3.6975	3.0992	2.5714	2.1327	1.7209	1.3583	0.81005	0.34882	0.14424	0.13372	2.297
CIG1R	6.1406	4.3223	4.0728	3.9195	3.3406	2.131	2.0838	2.0476	1.4691	0.75265	0.36395	0.13663	0.1366	2.296
CIG2R	6.158	4.3993	4.0805	3.8745	3.2528	2.1668	2.0964	2.0429	1.4676	0.75373	0.36354	0.13676	0.13671	2.297
CIG3R	7.2707	4.1879	3.858	3.7184	3.1613	2.138	2.0844	2.0305	1.4495	0.7594	0.36095	0.1382	0.13818	2.302
CIG4R	7.4007	3.9411	3.8495	3.8175	3.304	2.0741	2.0596	2.0335	1.4534	0.75685	0.36127	0.13819	0.13818	2.302

Table 5.6: Results obtained from IPIT-CZL for the selected experiment with four initial guesses. Part II

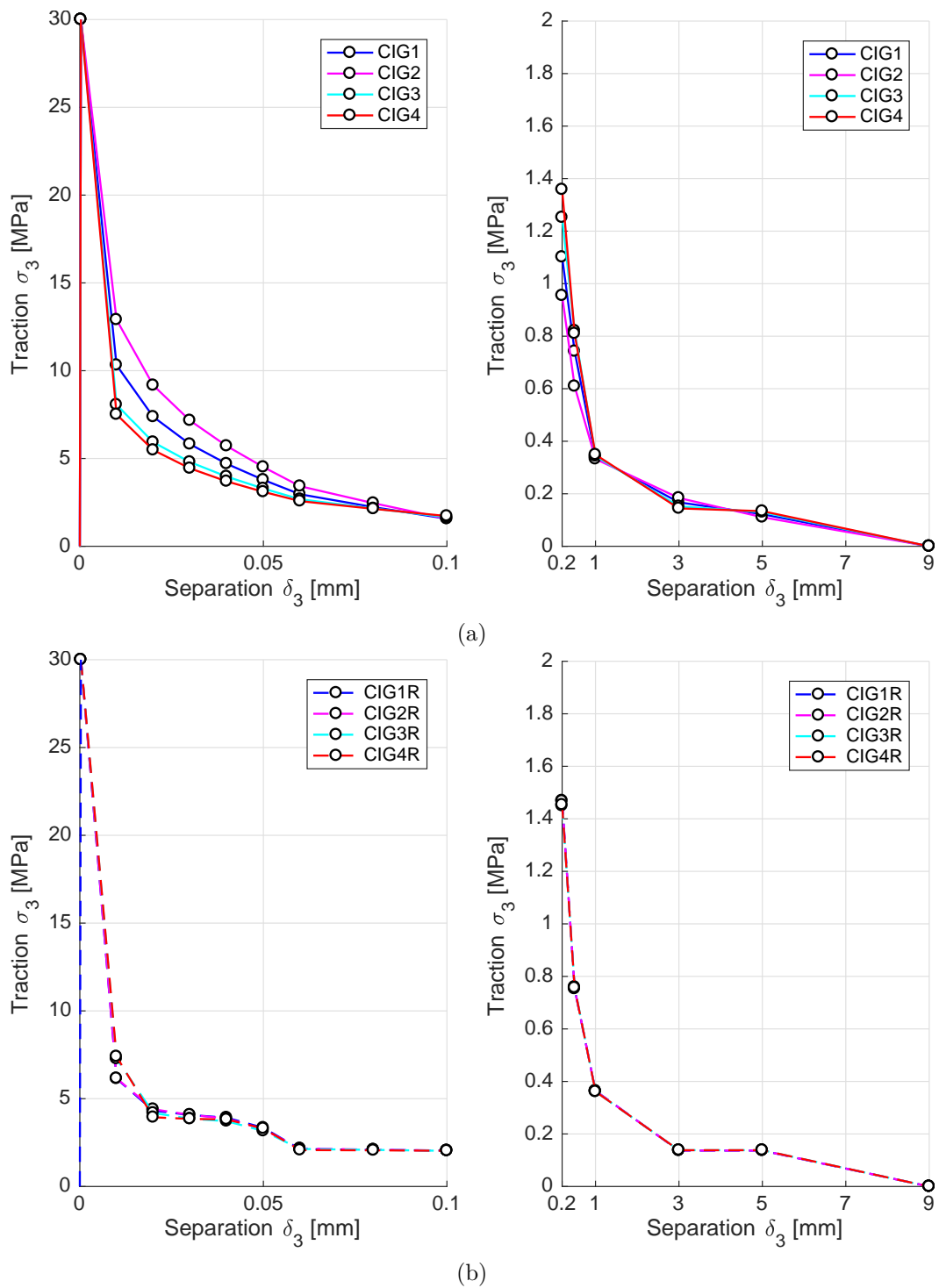
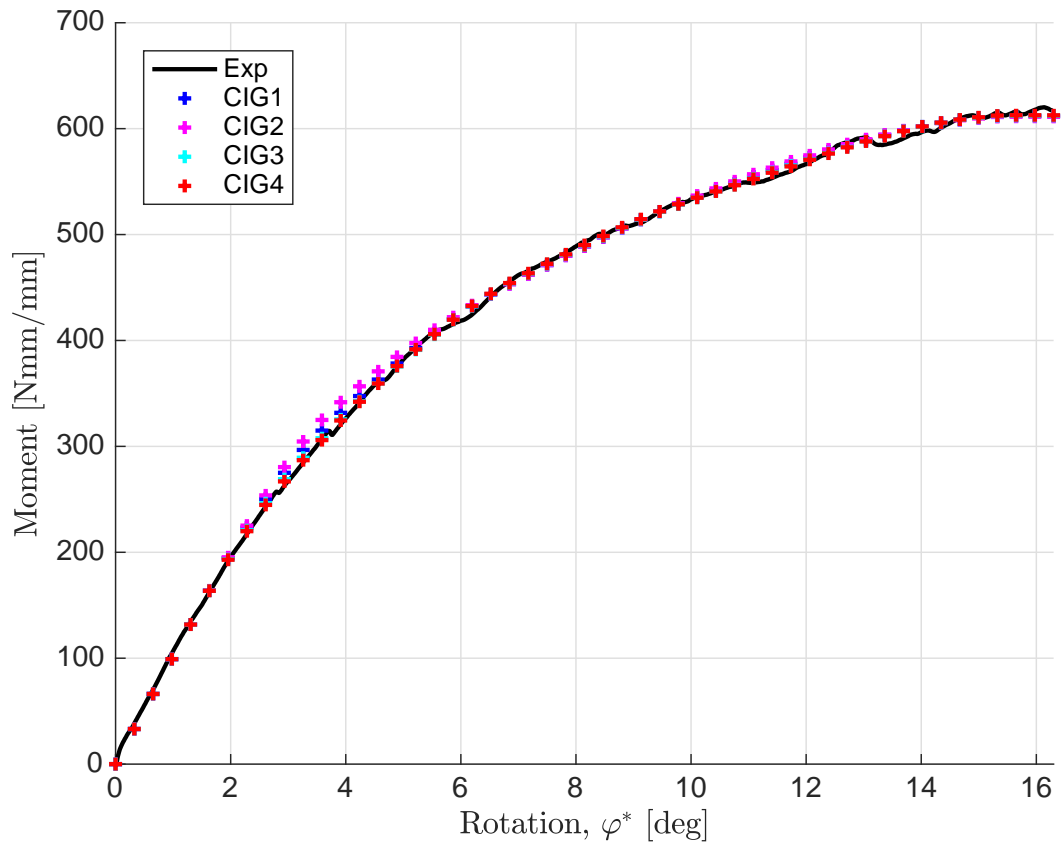
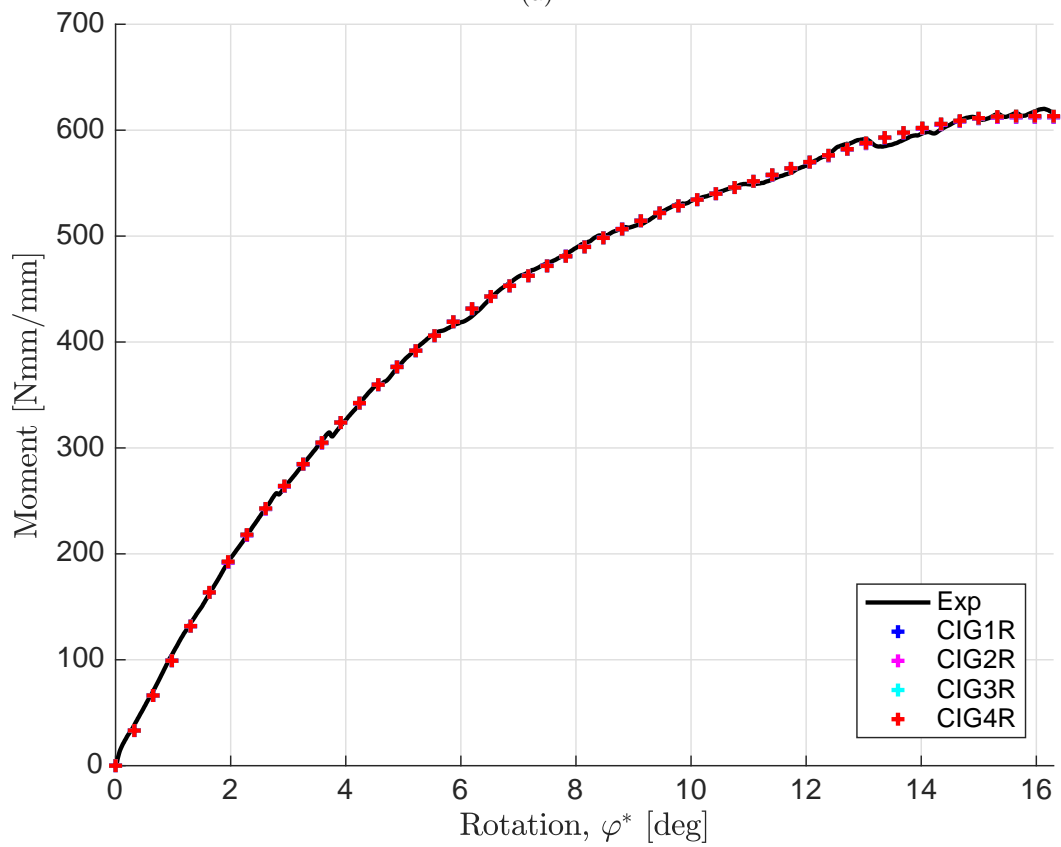


Figure 5.12: Converged CZ laws of (a) IG1 through IG4 (b) restarted IG1 through IG4.



(a)



(b)

Figure 5.13: Converged global structural responses of (a) IG1 through IG4 (b) restarted IG1 through IG4.

An alternative measure of structural response is available from the experiment in terms of moment versus end opening separation δ^* . The agreement in this response is investigated here. This comparison is of interest, since this moment-end-opening measure is independent of the angular measure used for the characterization of the CZ law. In general terms, there is a good concordance between the numerical and the experimental response as illustrated in Fig. 5.14b. However, the transition between linear and nonlinear structural response in Fig. 5.14b seems to occur prior to the numerical simulation around 250 Nmm/mm than the experiment around 300 Nmm/mm. One could suggest that some energy should be shifted from the bridging to the crack tip part of the CZ law, but that contradicts what is seen in the moment-rotation global structural response in Fig. 5.14a where the responses completely agree.

The discrepancy in the moment-end-opening curve in Fig. 5.14b could be due to numerous reasons; most likely including different bulk material properties of the specimen in the numerical and experimental model, variations in experimental measurements and 3D effects. The latter is probably the most prominent source of uncertainty, it is excelled by anticlastic bending, which leads to an apparently larger interfacial strength on the side of the specimen [Joki et al.]. This influences the end-opening measurements δ^* , as these are measured on the specimen sides, and consequently are delayed with respect to the crack openings at the specimen midplane. In addition, the specimen in the numerical model has unit width as opposed to the true width of 24.6mm in the physical experiment. Hence, a disagreement in Fig. 5.14b should be expected due to 3D effects. Similarly, the anticlastic bending does not affect the slope of the beam's longitudinal axis. This could also explain why there is an agreement for the linear/nonlinear transition in Fig. 5.14a but not in Fig. 5.14b.

Nonetheless, there is another relevant issue concerning the experimental measurement of the end-opening separation, that explains why a greater apparent interface strength is expected. The maximum clip gauge tolerance achievable is 0.1 mm since a caliper was used for its calibration and the onset separation is in the order of $1e-4$ mm. Therefore even if a displacement equal to the onset separation takes place on the side of the specimen, the measuring device will not be able to capture it. Thus, despite the fact that anticlastic bending can be included in the simulations, there will still be differences in the moment-end-opening displacement responses due to the sensitivity of the measuring device.

The previous conjectures and statements motivate a more thorough analysis of the results. Sensitivity studies of the global structural response to changes in the CZ law and 3D effects is the topic of the following chapter, which is crucial to conclude if some of the hypotheses stated here hold true or not.

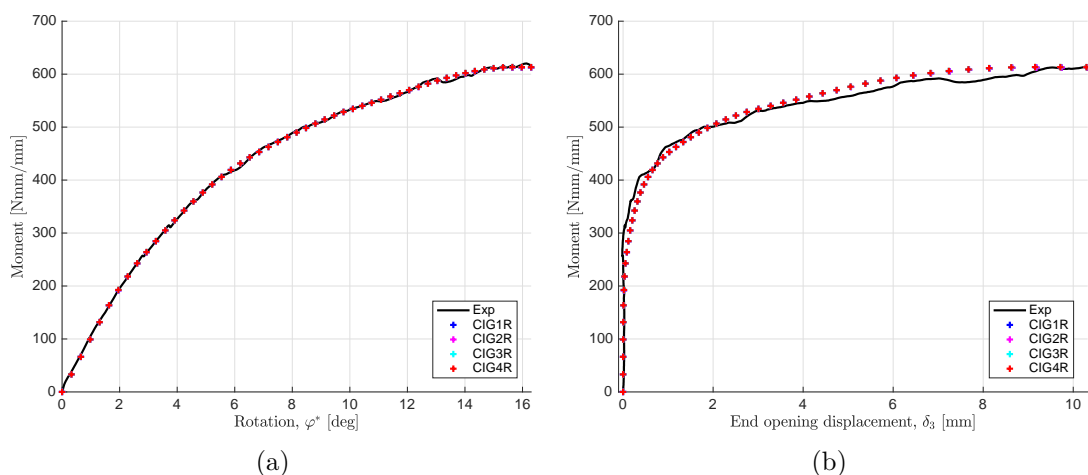


Figure 5.14: Comparison of numerical and experimental global structural responses for all solutions: (a) Applied moment versus angle of rotation (b) Applied moment versus end opening separation.

5.5 Progression of IPIT-CZL Optimizer

In this section it is elaborated further on the restart of the optimization process and the history of design variables, gradients, Hessian matrix eigenvalues, and objective function values. The optimization process is again presented by considering the third initial guess IG3, however, results and findings for this section are general tendencies and applies for all initial guesses IG1-4. During the optimization process, information concerning the convergence rate, objective function, design variables, gradients and Hessian matrices has been monitored. The history for two design variables are shown in Fig. 5.15a through 5.15d in terms of the iteration number $nIter$. The design variables under consideration are DV1 and DV11, corresponding to tractions of points $(\delta_3^{(2)}; \sigma_3^{(2)})$ and $(\delta_3^{(10)}; \sigma_3^{(10)})$ respectively of a pure mode I multilinear CZ law. They represent a point in the NCT region and a point in the FB region.

Note the scale of the secondary axis is different for each plot. Additionally, in Fig. 5.15b and 5.15d, a zoom-in is done such that the oscillations for a large range of iteration numbers can be seen. Initially, the magnitudes of the gradients are several orders of magnitude larger, and drops significantly within the first 5 iterations, which is illustrated in the small figures inside Fig. 5.15b and 5.15d.

Fig. 5.15f and 5.15g plots the objective function value as the optimizer progresses. Recall, that the optimization algorithm is restarted when $nIter=78$. Fig. 5.15e shows the evolution of the Hessian matrix condition number, defined as the ratio of the largest and smallest eigenvalue in absolute value. From all the history plots, four essential observations are noted, which are discussed in more detail:

- (1) The convergence rate is reduced significantly after around $N=13$ iterations, corresponding to the number of design variables.
- (2) After restarting the algorithm, significant changes are again seen and the optimizer progresses towards the minimum.
- (3) Severe zigzagging in positive and negative values of the gradients are observed in some regions.
- (4) There is a large span in Hessian eigenvalues.

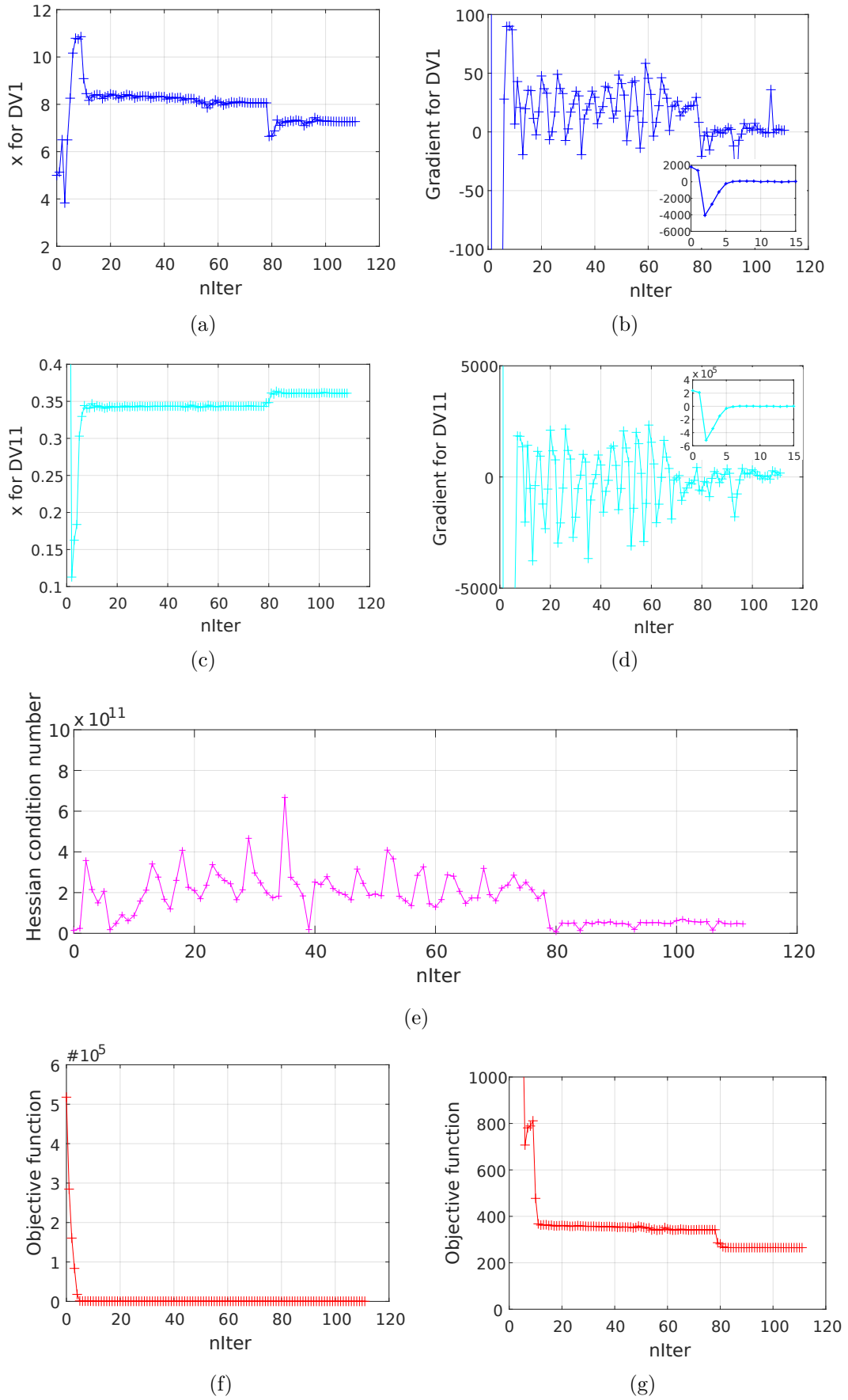


Figure 5.15: History data for initial guess 3.

The restart of the optimizer at $nIter=78$ with an initial guess of the latest converged iteration ($\vec{x}_0 = \vec{x}|_{nIter=78}$, shows significant changes in the design variables and the objective function, and the gradients decreases towards zero. The combined effect of items (1) and (2), suggests restarting the optimizer for every about $(N+1)$ iterations during the whole optimization process, to have effective changes in the design variables towards the minimum, and to do so within a reasonable number of iterations. Imagine e.g. that the nearly horizontal line from $nIter \approx 20$ until $nIter = 78$ could be avoided, and how that would be computationally efficient.

The concept of restating optimization schemes and seeing an improvement in the performance of the optimizer is not surprising. It is stated in [Arora, 2012], that quasi-Newton methods needs to be restarted at every $(N+1)$ iteration for general objective functions, such that $\vec{x}_0 = \vec{x}_{(N+1)}$, for computational stability. Restarting optimizers after some number of iterations typically holds for optimizers using second order information, since Hessian approximations may have been calculated with information not valid at the current design point due to highly nonlinear functions or nonconvexity etc.

Not only second order methods can benefit by a restart. Conjugate gradient methods will find a minimum in N iterations for positive definite quadratic functions having N design variables (and so would quasi-Newton methods for that sake). However, for general functions conjugate gradient methods should be restarted after $(N+1)$ iterations [Arora, 2012], since invalid direction enforcements of successive design iterates may deteriorate the convergence, which is solved by a restart.

The optimization algorithm used for IPIT is an interior point algorithm according to [Waltz et al., 2006], which is able to switch between a quasi-Newton method in combination with a line search method (QN-LS) to calculate the step size, and a trust-region method with a conjugate gradient method (TR-CG). The switch between QN-LS and TR-CG depends on function non-convexity and Hessian rank deficiency, as explained previously in Sec. 4.2.2. Thus, the optimizer used for IPIT is neither a direct quasi Newton method nor a direct conjugate gradient method, which should be restarted after $(N+1)$ iterations [Arora, 2012], however, it relies on both of them. Consequently, restarting IPIT after some iterations may be beneficial.

This hypothesis is tested, by starting IPIT from IG3, and for every $(N+1)$ iteration the algorithm is restarted such that $\vec{x}_0 = \vec{x}_{(N+1)}$. It has been observed, that restarting the algorithm at every $(N+1)$ iteration is effective for sets of design variables that are far away from the optimum point. However, as the design variables approaches the optimum point, the restarts become less effective. It is not recommended to restart the algorithm when design variables are close to the optimum. In one test, the algorithm is restarted two times. It is restarted at $nIter=14$ and again at $nIter=28$, and it gives a converged solution in agreement with those shown in Fig. 5.13 at $nIter=80$. Consequently, the restarting of the algorithm reduced the total number of iterations by 30, and is proven to be effective for initial design iterates which are still far from the optimum point.

Observation (4) is related to a large span in Hessian eigenvalues. Throughout the iterations, the condition number of the Hessian matrix is on the order of 10^{11} , as illustrated in Fig. 5.15e, which indeed categorizes the problem as being ill-conditioned. This merely supports the findings from the initial benchmark tests using a bilinear CZ law in Sec. 4.2.6, but here in a more extreme case based on the condition number of the Hessian matrix.

It is noted, that the Hessian matrix is approximated at some design iterate based on the computed gradients. Consequently, the statements concerning the Hessian matrix are not exact but suggest tendencies. The Hessian matrix is concerned with second order derivatives, whether it is approximated or exact, and clearly there is a significant difference in second order derivatives, indicating a difference in the relative dominance of the design variables.

This can be attributed to a difference in work of separation/energy release rate associated with each design variable. For instance a change in a design variable in the FB region would result in a greater change in the energy of the system due to the relatively coarse discretization of separation points here, compared to the fine discretization in the NCT region. A priori the energy in the system is known to be dominant, this is also seen using IPIT-CZL, which converges to the correct critical energy release rate within few iterations.

Another reason that influences the relative dominance of design variables is the formulation of the objective function. The objective function is defined as the difference in structural response at discrete points, shown as blue crosses in the plots of global structural response. These points are distributed equidistant in the rotation φ -space, but a larger amount of the moment-rotation curve is associated with the FB region than the NCT region. This is evident by comparison of Fig. 5.12a and Fig. 5.13a; for relatively large differences in NCT region, only a small difference is shown in the structural response.

Sensitivity Studies and 3D Effects

6.1 Sensitivity Studies of IPIT-CZL

In the previous section, IPIT-CZL was shown to be robust in finding the same optimum point for four different initial guesses for the specific set-up of IPIT-CZL. During the development of IPIT-CZL various assumptions and decisions have been taken, which effect the characterization of the CZ parameters. Some of these decisions are reviewed in the current section, sensitivity to these are examined. This serves as a study of the robustness of the methodology. At first, the following sensitivity studies are undertaken:

- (A): Subject the fixed location of $\delta_3^{(i)}$ to small variations.
- (B): Reducing number of line segments.
- (C): Variations in sets of experimental data.

A major source of uncertainties is 3D effects. This topic is given its own special treatment and is considered in Sec. 6.2.

6.1.1 Redistribution of CZ Separation Points and Line Segments

The design problem is set up, such that only tractions $\sigma_3^{(i)}$ of the CZ law are treated as design variables, while the separations $\delta_3^{(i)}$ are fixed quantities. This issue was a topic of interest in Sec. 5.3 and Sec. 5.1. It was argued, that experimental data, as measurements of the end opening at the initial crack tip, could guide the placement of the fixed separation values. This suggested the final separation value, and which regions the separation-point density should be high. However, the specific location of $\delta_3^{(i)}$, the number of line segments in the near crack tip (NCT) region and the far bridging (FB) region are all user-defined. This subsection is concerned with items (A) and (B) above, and their influence on CZ parameters obtained using IPIT-CZL.

At first, the original CZ law obtained using IPIT-CZL for the discretization of separation points given in Tab. 5.3, and repeated in the "Original"-column of Tab. 6.1, is compared to a solution obtained with IPIT-CZL using an alternative discretization of the same number of separation points. The discretization for sensitivity study (A) is obtained by subjecting every $\delta_3^{(i)}$ in the "Original" column to a small variation. The resulting separation points are shown in the (A)-column of Tab. 6.1.

Separation Pnt.: $\delta_3^{(i)}$	Original [mm]	(A) [mm]	(B) [mm]	(C) [mm]
Pnt. Nr. 1	3.000e-04	3.000e-04	3.000e-04	3.000e-04
Pnt. Nr. 2	0.010	0.005	0.010	0.010
Pnt. Nr. 3	0.020	0.015	0.020	0.020
Pnt. Nr. 4	0.030	0.025	0.040	0.030
Pnt. Nr. 5	0.040	0.035	0.060	0.040
Pnt. Nr. 6	0.050	0.045	0.100	0.050
Pnt. Nr. 7	0.060	0.055	0.200	0.060
Pnt. Nr. 8	0.080	0.070	1.000	0.080
Pnt. Nr. 9	0.100	0.090	3.000	0.100
Pnt. Nr. 10	0.200	0.190	9.000	0.200
Pnt. Nr. 11	0.500	0.400	-	0.500
Pnt. Nr. 12	1.000	0.900	-	1.000
Pnt. Nr. 13	3.000	2.500	-	3.000
Pnt. Nr. 14	5.000	5.500	-	5.000
Pnt. Nr. 15	9.000	9.000	-	9.000

Table 6.1: Various distributions of fixed separation points $\delta_3^{(i)}$ for a pure mode I CZ law. Changes compared to the original distribution are marked in **bold text**.

Secondly, the (B) item is considered. Here, the number of line segments of the CZ law is reduced by five, resulting in a 10-segmented multilinear CZ law. The separation points used are shown in the (B)-column of Tab. 6.1.

For the (A) and (B) distributions of separation points, IPIT-CZL is started from initial guess IG2, according to Tab. 5.4. The converged solution of the sensitivity analysis (A) and (B) are gathered in Tab. 6.2 and plotted in Fig. 6.1 together with the original solution. The corresponding global structural responses are shown in Fig. 6.2.

In general, similar results have been obtained, the overall shape of the CZ law is clearly of general character, and the solutions agrees in terms of total energy and energy distribution in the NCT and FB regions. Due to the piecewise linear nature of the CZ law, an adjustment of every traction point $\sigma_3^{(i)}$ is naturally expected, when the CZ law is reduced from a 15- to 10 segmented CZ law or when small variations in the discrete separation points are given, to keep the energy consistent.

Regarding sensitivity study (A), one should expect to obtain traction points $\sigma_3^{(i)}$ in the neighbourhood of the original ones, when separation points are subjected to small variations. This is also the case as seen from Fig. 6.1. Points in the NCT region, especially $\sigma_3^{(2)}$ and $\sigma_3^{(3)}$, shows the largest differences, but it should also be expected, since the slopes of the line segments are larger in this region.

In terms of specific details of the CZ law shape, the original CZ law obtained shows a bump in the region $\delta_3 : [0.02; 0.06]$ which is most clear in Fig. 5.13a, a similar bump is not seen in the sensitivity studies (A) and (B). Additionally, the (A) solution shows results in an objective function value of $f_{(A)} = 253.2$ as opposed to the original objective function value of $f = 265.1$. This indicates that the distribution of separation points in (A) is actually better than the original formulation. For completeness, the objective function value of sensitivity study (B) is $f_{(A)} = 388.7$, which is rather high, however, there is a small and almost negligible difference in the global structural response, and a converged solution is obtained in just 42 iterations.

Traction Pnt.: $\sigma_3^{(i)}$	Original-CIG2R [MPa]	(A) [MPa]	(B) [MPa]	(C) [MPa]
Pnt. Nr. 1	30.000	30.000	30.000	30.000
Pnt. Nr. 2	6.1580	14.0761	8.4985	7.6138
Pnt. Nr. 3	4.3993	6.0383	4.2935	4.9519
Pnt. Nr. 4	4.0805	4.5556	3.1757	3.9814
Pnt. Nr. 5	3.8745	3.9520	2.4526	3.3753
Pnt. Nr. 6	3.2528	3.3385	2.1457	2.9245
Pnt. Nr. 7	2.1668	2.5686	1.2289	2.5446
Pnt. Nr. 8	2.0964	2.1631	0.3124	2.2286
Pnt. Nr. 9	2.0429	1.9015	0.1773	1.9551
Pnt. Nr. 10	1.4676	1.6511	0	1.6349
Pnt. Nr. 11	0.7537	0.8328	-	0.7156
Pnt. Nr. 12	0.3635	0.4412	-	0.3274
Pnt. Nr. 13	0.1378	0.1424	-	0.1056
Pnt. Nr. 14	0.1367	0.1288	-	0.1002
Pnt. Nr. 15	0	0	-	0

Table 6.2: Traction $\sigma_3^{(i)}$ of the converged CZ law for each sensitivity study. The separations can be seen in the previous table.

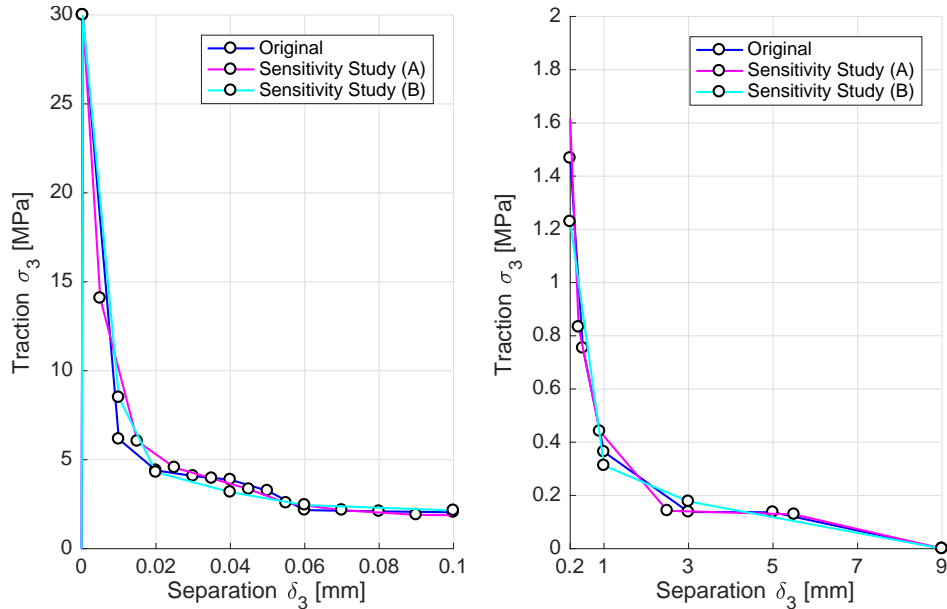


Figure 6.1: Comparison of CZ laws obtained for the different sensitivity studies with the original result.

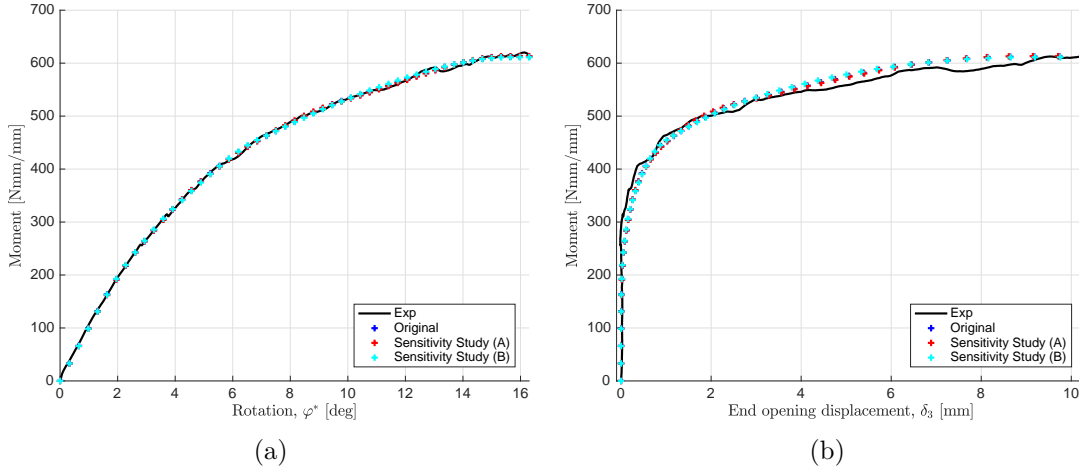


Figure 6.2: Converged solution for the sensitivity studies (A) and (B). Comparison of numerical and experimental global structural responses : (a) Applied moment versus angle of rotation (b) Applied moment versus end opening separation.

Any shape of a CZ can be approximated by piecewise linear functions, as long as the discretization is fine enough. The choice of the number of line segments depends on the application, if only a simulation of global structural responses are needed, or if a study of failure mechanisms is of interest, with the latter being more dependent on the actual shape of the CZ law. It is a compromise between computation time and application.

6.1.2 Variations in Sets of Experimental Data

Having discuss about the influence of the separation discretization of the CZ law in the previous subsection, now reproducibility of the results for different sets of experimental data is of concern. Prior to this analysis, the data set for the test specimen 0deg - 5 has been uniquely considered. Here, the data set for test specimen 0deg - 3 is used. The differences with respect to the test specimen 0deg - 5 are illustrated in Fig. 6.3. Note that both test specimens belong to the same series and share geometry, material properties and test set up, however as seen in Fig. 6.3a the elastic response differs significantly. This fact is believed to be due to the uncertainties related to the bending modulus, since the authors have observed variations up to 5 GPa in similar specimens which were tested in a three-point bending test, and related to the effective length of the DCB arms as discussed in Sec. 5.2.

A compromised decision needs to be taken, since there are uncertainties related to both quantities, it is decided to match the initial linear elastic response by changing the parameter a_0^* , as done previously in Sec. 5.2. Accordingly, the initial crack in the simulation will be $a_0^{Num} = a_0 - a_0^* = 66 - 46 = 20 \text{ mm}$. The global structural responses for the converged solution can be seen in Fig. 6.4 and the original CZ law obtained for the data set 0deg - 5 is compared with the CZ law obtained for the data set 0deg - 3 in Fig. 6.5, labeled as sensitivity study (C).

The numerical structural responses present an excellent agreement with the experimental data 0deg - 3 as can be seen in Fig. 6.4. In regards to the comparison between the CZ law obtained, there are some variations in each traction $\sigma_3^{(i)}$ with less implications in NCT region but at FB region all tractions are lower than in the original CZ law, leading to a significant change in the total fracture energy G_c , which is 2.297 kJ/m^2 for the original CZ law (experimental data 0deg - 5) and 2.112 kJ/m^2 for the other one (experimental data 0deg - 3). Furthermore, the shape of the CZ law in the FB region is identical to the original law.

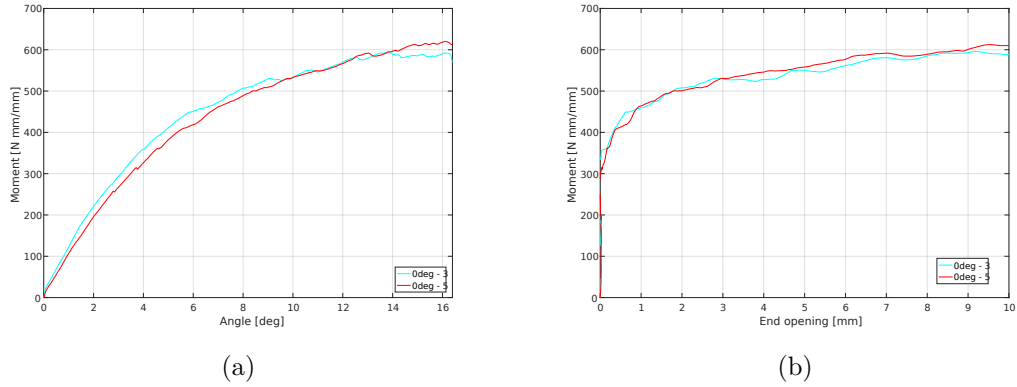


Figure 6.3: Global structural responses for test specimen 0deg - 3 and 0deg - 5 (a) Applied moment versus angle of rotation (b) Applied moment versus end opening separation.

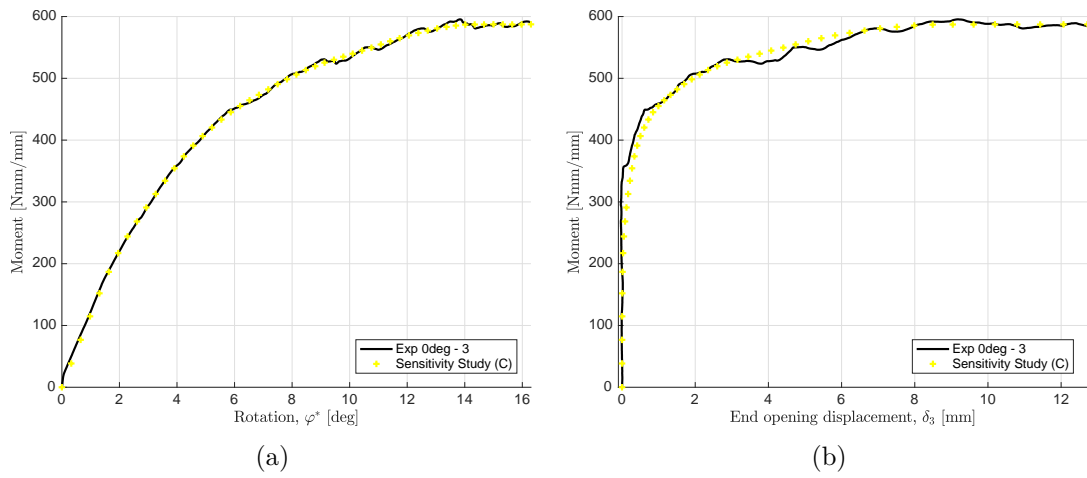


Figure 6.4: Converged solution using the data set 0deg - 3. Comparison of numerical and experimental global structural responses : (a) Applied moment versus angle of rotation (b) Applied moment versus end opening separation.

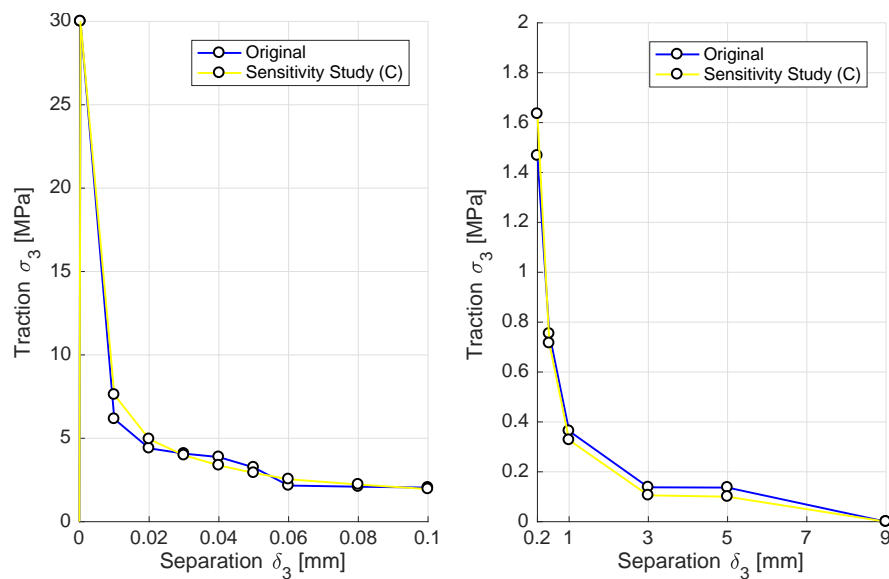


Figure 6.5: Comparison of CZ laws obtained for the data set 0deg - 5 (Original) and 0deg - 3 (Sensitivity Study (C))

6.2 3D Effects

So far in this work, only unitary width models have been dealt with. The goal of this section is to explore the changes in the CZ law obtained from the optimization program, when a full width model accounting the variation of the stress σ_3 across the width, owing to anticlastic bending, is used in the simulations.

Let one consider a structure subjected to bending, where there is a linear variation of the longitudinal stress σ_x through the thickness with tension and compression at opposite ends. The Poisson effect alters the cross section such that in the tension zone the material will shrink, whereas in the compression zone the material will expand. This deformation of the cross section modifies the curvature perpendicular to the bending direction of the structure, as illustrated in Fig. 6.6. This phenomenon is known as anticlastic bending.

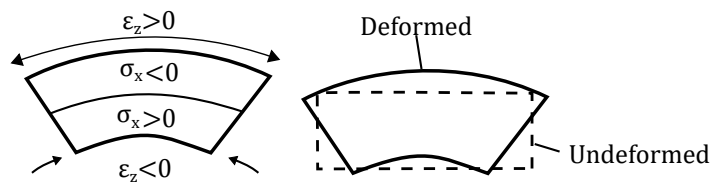


Figure 6.6: Poisson effect leading to anticlastic deformation of the cross section.

In a DCB specimen loaded by pure moments of equal value and opposite signs, both arms experience the same anticlastic bending and, at the process zone, the cross section of the laminate starts splitting into two subsections which are mirror images of one another as illustrated in Fig. 6.7. In addition, at the crack front, all the points lying at the interface have the same contribution to the interface traction σ_3 stemming from the bending load. However, in the central region, the total interface traction σ_3 is greater than that at the edges due to the contribution from the anticlastic deflection, as illustrated in Fig. 6.7b $\delta_3^{edge} < \delta_3^{middle}$ and so is $\sigma_3^{edge} < \sigma_3^{middle}$ before the onset of delamination. Therefore, the onset traction will be reached at the center of the crack front before it is reached at the edges, explaining the thumb nail shape of the crack front seen in Fig. 6.7a.

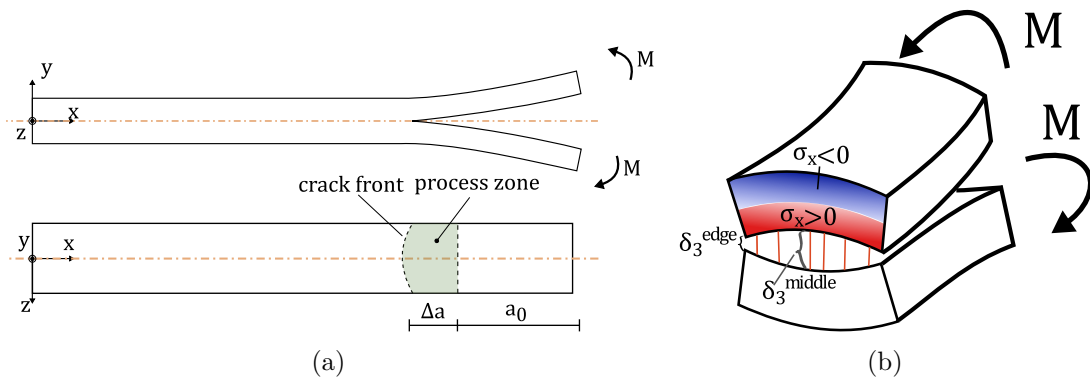


Figure 6.7: (a) DCB specimen loaded by pure moments in pure mode I crack opening (b) Cutaway of a section in the process zone where the separation δ_3 at the edge is larger than 0.

Having introduced a 3D effect and how it affects the delamination propagation, a comparison of results obtained using IPIT-CZL for a unit- or full width model is regarded. Furthermore, it is considered of interest to obtain results of a full width model where the Poisson's ratio ν_{xz} is set to zero, which in principle should give the same result as that from the unit width

model. The initial guess under consideration is IG4, presented in Sec. 5.4.

The CZ laws obtained from the three models are shown in Fig. 6.9, and the corresponding global structural responses: Moment versus angle of rotation and moment versus end-opening separation are shown in Fig. 6.10a and Fig. 6.10b, respectively. Note that the IPIT-CZL solution for the full width model gets stuck in local minima, even if it is restarted closer to the solution obtained for unit width model. The reason for this is unknown, but is a topic for further work.

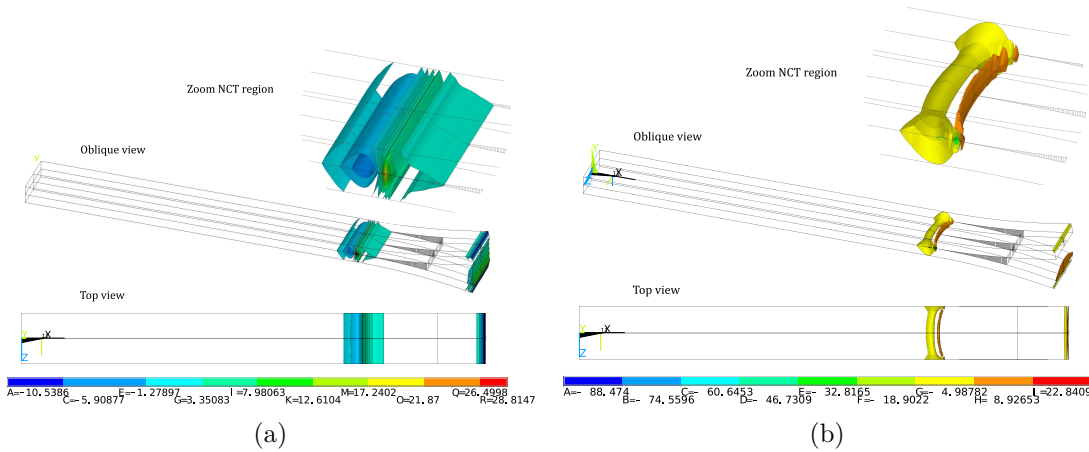


Figure 6.8: Isosurface contour plots at angle of rotation $\varphi^* = 11.41^\circ$, σ_y is displayed (a) Full width $\nu_{xz} = 0$ model (b) Full width model.

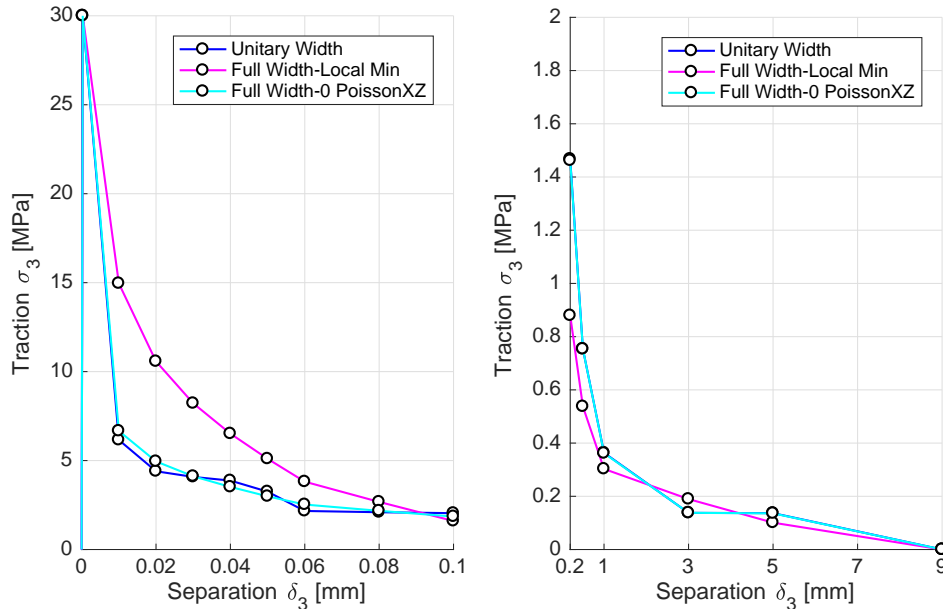


Figure 6.9: IPIT-CZL solutions: Comparison of CZ laws obtained of the full width, the full width-zero Poisson's ratio ν_{xz} and the unit width model

Firstly, the IPIT-CZL solutions in Fig. 6.9 are of concern. Besides the solutions for the full width model, there is a perfect agreement in the FB region and a good agreement in the NCT region of the CZ laws between the unit width model and the full width with $\nu_{xz} = 0$, as expected.

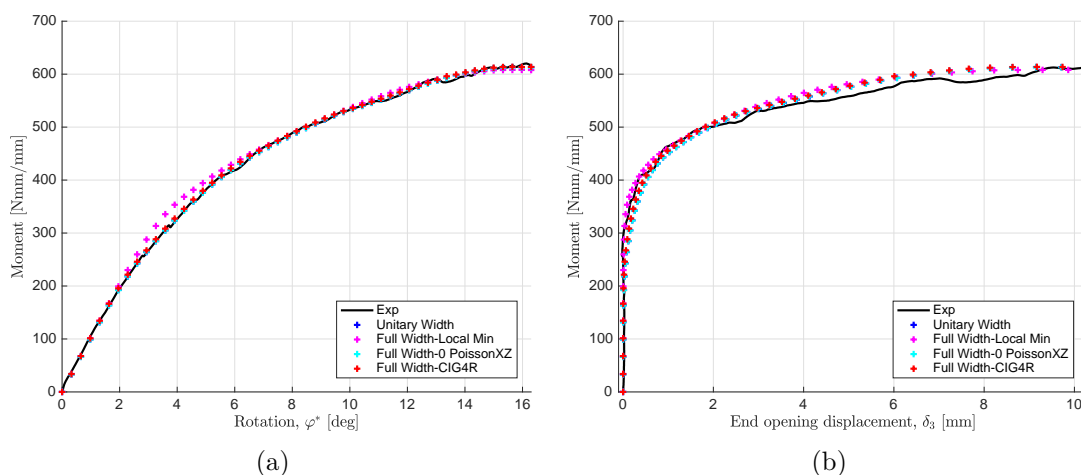


Figure 6.10: IPIT-CZL solutions: Comparison of numerical global structural responses of the full width, the full width-zero Poisson ratio ν_{xz} and the unit width model: (a) Applied moment versus angle of rotation (b) Applied moment versus end opening separation.

As argued in Sec. 5.5, the interface tractions in the NCT region are dominated, in an optimization context, by the tractions in the FB region, ergo it is expected that the optimizer will have more difficulties to determine the optimum value of those design variables. Regarding the structural responses in Fig 6.10, no significant differences are seen and both solutions are considered equally as good.

Since no converged solution for the full width model with non-zero Poisson's ratio is obtained, the global structural responses associated with the light red CZ-law in Fig. 6.9 is not considered. Nevertheless, the effect of anticlastic bending in the structural response will be illustrated by comparing the full width models with $\nu_{xz} = 0$ and $\nu_{xz} \neq 0$ for a given CZ law. For that purpose, the CZ law CIG4R shown in Tab. 5.6 is used. Moreover, the unit width model is included as well, to highlight that there are no differences with respect to the full width with $\nu_{xz} = 0$ model, as presumed.

In Fig. 6.11a, there are no significant differences that can be noticeable from the global structural responses. Nonetheless, a finer measure of the agreement with the experimental data is provided by the objective function. The objective function of the unit width model is 265.04 and of the full width with $\nu_{xz} = 0$ is 273.93, hence there is only small difference. On the other hand, the objective function of the full width model is 423.75 which compared to the 273.93 of the full width with $\nu_{xz} = 0$ constitute a significant difference. Furthermore, in Fig. 6.11b the full width model gets closer to the experimental data compared to the other two curves, which practically lay on top of each other. The reason is the anticlastic effect illustrated in Fig. 6.7. It is important to note that the only difference between these two models is one single parameter the Poisson's ration ν_{xz} . Thereby, it is shown that the global structural responses are affected by the anticlastic bending, and consequently it is believed that a different CZ law would be obtained from the optimizer. However, the prove of this is left as further work due to lack of time, especially for running simulations of full width.

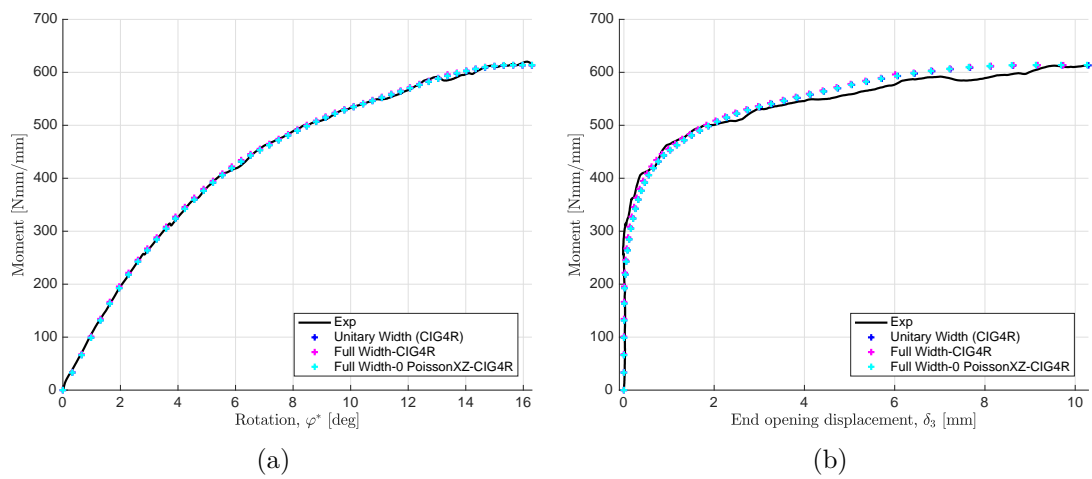


Figure 6.11: Anticlastic effect: Comparison of numerical global structural responses of the full width, the full width-zero Poisson ratio ν_{xz} and the unit width model for the same CZ law named CIG4R: (a) Applied moment versus angle of rotation (b) Applied moment versus end opening separation.

Conclusion

In this master thesis a methodology for parameter identification of multilinear cohesive zone laws for numerical assessment of quasi-static delamination in composite materials is developed and tested. The parameter identification is done inversely from outputs of a parametric finite element model and experimental data, and relies on minimization of a residual between the two responses.

The experimental specimen under consideration is a UD glass fiber DCB specimen showing sever R-curve behaviour due to fiber-bridging. In order to accurately simulate the delamination propagation for such material systems, a CZ law capable of modelling large scale bridging failure mechanisms is a necessity. In a previous semester, this has been addressed by simply extending a bilinear CZ law to a trilinear one. Here, the trilinear CZ law has been extended to a CZ law having an arbitrary number of line segments, which has been necessary to model the experimental response adequately.

Additionally, the multilinear CZ law has been generalized to be able to model mixed mode crack opening. The mixed mode CZ law is formulated as a one-dimensional equivalent CZ law. The multilinear CZ law is constructed from discrete traction-separation points interconnected by lines. Interpolation formulae are defined for these discrete traction-separation points. Traction are interpolated using a quadratic interaction criterion, while separations are interpolated such that the resulting CZ law is energy consistent with the BK-criterion.

The process of parameter identification is done through optimization techniques and is implemented in MATLAB in a program denoted IPIT-CZL. A first draft of IPIT-CZL has been developed at the previous semester. Here, the optimization problem is ironically enough optimized, by reformulating objective function as a least squares formulation, allowing the computation of a reasonable approximation of second order information, which is seen to significantly improve the optimizer performance. Subsequently, different algorithms have been considered by implementing them in IPIT-CZL and running simple benchmark tests.

IPIT-CZL is used for characterization of a 15-segmented multilinear CZ law for the previously mentioned DCB specimen under pure mode I crack opening. The method succeeds in consistently obtaining the same CZ parameters for different initial guesses. Further studies of the performance of the optimizer suggests improvements for further work and general guidance for using the methodology. Ill-conditioning and restart of optimizer. The promising results prove that in essence the presented methodology works and could be an alternative candidate to current approaches proposed in the literature based on J-integral. However, this should be proven by comparison with one of such methods, which unfortunately is left for further work.

Lastly, the robustness and general applicability of the methodology is investigated by conducting sensitivity studies and discuss influences from 3D effects. A dependence was found to the discretization of the separation points $\delta_3^{(i)}$ in the CZ law. However, the dependence indicates a robust method rather than crucial influence of the separation point locations. Regarding the influence of the obtained results to the inclusion of 3D effects, the dependence could not be proven as the optimizer got stuck in local minima, but it is believed that it cannot be disregarded. Also, the natural variation of this kind of phenomenon is considered by using different experimental data in IPIT-CZL. Related to this, it is argue that the same shape of the far bridging region of the CZ law is obtained for the two coupon test specimens of the series although the total fracture energy differs in approximate 0.2 kJ/m^2 . Another key aspect discussed is the ill-conditioning of the optimization problem. It is believed that the global minimum has not been found yet and by treating the problem and transform it into an well-conditioned one, the global minimum would eventually be found. Furthermore, it is believed that the global minimum would be less sensitive to the discretization of the separation points. In essence, by improving the ill-conditioning issue a more robust methodology will be obtained.

Further Work

During this master thesis plenty of work has been done and main objectives have been achieved. Nonetheless, a large amount of further development can be foreseen by the authors. Some tasks are specific to the methodology, these are listed first. Thereafter, the perspective is broadened out to discuss future potential of the current work.

Specific tasks for the current work are listed first, and are sorted by topic. These are mainly concerned with improving the current methodology, things that have not been done due to lack of time, and perform further numerical and experimental studies to evaluate assumptions introduced.

Cohesive Zone Modelling:

- Optimize the code of the user-defined element subroutine.
- Implementation of a deformation-history dependent mode mixity parameter B . Currently the mode mixity B is based on instantaneous nodal displacement values. However, it is reported in [Abaqus] to be favorable to introduce deformation history in the calculation of B in case of large scale fiber bridging.
- Experimental study of the interpolation formulae to be used for predicting mixed mode equivalent properties.
- Elaborate further on the results of the sensitivity studies; hereby the location of the separation points in the CZ law and the number of line segments to be used.

IPIT-CZL (Optimizer):

- Investigate the ill-conditioning of the optimization problem further. E.g. can the design problem be formulated differently to help reducing ill-condition and improve the convergence rate. Note that built-in functions in MATLAB, as the interior-point algorithm, cannot be modified. Thus, it is very likely that an open source algorithm or a self-made one will be required for doing such tasks.
- Related to the previous item, it would be beneficial extracting more information about the algorithm, e.g. printing in screen the search direction, step size and step type (Newton or conjugate gradient) in order to assess whether ill-conditioning or other difficulties arise during the optimization problem, and if it does, when does it happen.
- IPIT-CZL has been used for obtaining CZ laws for pure mode I. IPIT-CZL should be tested for pure mode II and subsequently mixed mode crack openings too.

- The results obtained using IPIT-CZL should be compared to other approaches for characterization of CZ laws, e.g. [Hansen et al., 2009].

Experiments and Finite Element model:

- Perform experimental study of the specimen bulk material properties (especially E_{xx}, ν_{xy}), to reduce assumptions in FE model. In order to finally determine the cohesive zone law for the material system under consideration, the results should be based on multiple test specimens rather than a single measurement.
- Automate the data extraction and ease the process of data acquisition. For example, a script could be created to read the raw data file and provide an output file where spurious data, commonly seen at the beginning of the test, is deleted.
- Search for local measures in the numerical model and the experiment to be used in the objective function. Possibly combined with a global structural response by using a multiobjective function.

Future Potential:

Having presented specific suggestions for further work with IPIT-CZL, the perspective is broaden out to a discussion about the potential of the methodology. A novel methodology for determination of CZ laws is presented, which in principle puts no restrictions on the shape of the CZ law, apart from being piecewise linear, however in the limiting case of a fine discretization of separation points in the CZ law, the CZ law shape is free to vary. In the report the methodology is proven to be able to determine a 15-line segmented CZ law for a DCB specimen under pure mode I loading. The CZ law shape contains valuable information of the nature of the failure mechanisms in the fracture process zone [Sørensen and Kirkegaard, 2006]. Identification of failure mechanisms is important for development of new materials and microstructural optimization in terms of strength increase and fracture resistance. This motivates for further work with the current methodology.

In this report, the CZ law shape is determined based on structural response. In terms of failure mechanism identification, it is likely that local measures in the fracture process zone are more convenient. However, in principle there are no limitations on the responses from the numerical model and the physical experiment to use for the parameter identification. Experimental measurements of local response in the fracture process zone can be obtained using e.g. strain gauges or digital image correlation [Laurin et al., 2012], these could be replace the current objective function of global structural response, or be combined using multiobjective function definitions.

In the report, the parameter identification is tested on coupon tests usually used for assessment of fracture related properties. Apart from heavier simulations, nothing cancels the opportunity of applying the current method on real structures or submodels of real structures. The idea of this approach is to perform the CZ law characterization on a specimen experiencing the same deformation history as the engineering structure to be modelled subsequently.

Bibliography

- Abaqus. *6.14 - Abaqus Analysis User's Guide*. URL <http://50.16.225.63/v6.14/books/usb/default.htm>. 32.5.6 Defining the constitutive response of cohesive elements using a traction-separation description. 31, 32, 107
- G. Alfano and M. A. Crisfield. Finite element interface models for the delamination analysis of laminated composite: mechanical and computational issues. *International Journal for Numerical Methods in Engineering*, 50:1701–1736, 2001. 5, 6
- J. H. Andreasen. Fracture mechanics. In *Master Course Notes: Fracture Mechanics*. Department of Mechanical and Manufacturing Engineering, Aalborg University., 2015. 29
- I. ANSYS. *ANSYS Documentation. Mechanical APDL. Element Reference. 5.1.2.1.2 Enhance Strain Formulation*, 2016. 57
- J. S. Arora. *Introduction to Optimum Design*. Engineering Optimisation. Elsevier Inc, third edition, 2012. 58, 92
- B. L. V. Bak, E. Lindgaard, and E. Lund. Analysis of the integration of cohesive elements in regard to utilization of coarse mesh in laminated composite materials. *International Journal for Numerical Methods in Engineering*, 99(8):566–586, 2014. ISSN 0029-5981. doi: 10.1002/nme.4688. 6, 20, 43, 75
- G. I. Barenblatt. Concerning equilibrium cracks forming during brittle fracture. the stability of isolated cracks. relation with energetic theories. *Journal of Applied Mathematics Mechanics*, 23:622–636, 1959. 6
- M. L. Benezeggagh and M. Kenane. Measurement of mixed-mode delamination fracture toughness of unidirectional glass/epoxy composites with mixed mode bending apparatus. *Composites Science and Technology*, 56(4):439–449, 1995. 28
- C. Boffoli. A disassembled carbon fiber fuselage section of the boeing dreamliner 787 in everett, washington. Wikimedia Commons, 2007. URL <https://en.wikipedia.org/wiki/File:787fuselage.jpg>. ix, 4
- R. H. Byrd, R. B. Schnabel, and G. A. Shultz. Approximate solution of the trust region problem by minimization over two-dimensional subspaces. *Mathematical Programming*, (40):247–263, 1988. 57, 59
- P. P. Camanho, C. G. Davila, and M. F. De Moura. Numerical simulation of mixed-mode progressive delamination. *Composite Materials*, 37, No. 16/2003:24, 2003. 6, 28
- E. T. Christensen, J. H. Sjølund, and J. A. Glud. Formulation of cohesive finite element for analysing strength of wrinkles in glass-epoxy laminates. M. sc. design of mechanical systems, Institute for Mechanic and Production. Aalborg University, 2013. 51

- R. D. Cook, D. S. Malkus, M. E. Plesha, and R. J. Witt. *Concept and Applications of Finite Element Analysis*, volume 4. John Wiley & Sons, 2002. 19, 41
- D. S. Dugdale. Yielding of steel sheets containing slits. *Journal of the Mechanics and Physics of Solids*, 8:100–104, 1960. 6
- V. K. Goyal. *Analytical modeling of the mechanics of nucleation and growth of crack*. PhD thesis, Virginia Polytechnic Institute and State University, Blacksburg, VA 24060, 2003. 5, 11, 14, 15, 17, 18, 19, 42
- V. K. Goyal-Singhal, E. R. Johnson, and C. G. Davila. Irreversible constitutive law for modeling the delamination process using interfacial surface discontinuities. *Composite Structures*, 65(3):289–305, 2004. 6, 77
- A. A. Griffith. The phenomena of rupture and flow in solids. *Philosophical Transactions of the Royal Society of London. Series A*, 221:163–198, 1921. 5
- A. L. Hansen and E. Lund. A mixed mode cohesive law for modeling interfacial fracture and fiber bridging. Unpublished, 2009. ix, 6, 23, 26, 29, 30, 31, 77
- A. L. Hansen, E. Lund, and B. F. Sørensen. Simulation of crack growth and r-curve behavior using cohesive zone modeling. Unpublished, 2009. 8, 29, 76, 108
- D. J. Haugen. Fracture of skin-stiffener intersections in composite wind turbine blade structures. M. sc. mechanical engineering, Montana State University Bozeman, 1998. ix, 3, 4
- T. K. Hellen. On the method of virtual crack extensions. *International Journal for Numerical Methods in Engineering*, 9:187–207, 1975. 5
- A. Hillerborg, M. Modeer, and P. E. Petersson. Analysing of crack formation and crack growth in concrete by means of fracture mechanics and finite elements. *Cement and Concrete Research*, 6:773–782, 1976. 6
- G. R. Irwin. Analysis of stresses and strains near the end of a crack traversing a plate. *Journal of Applied Mechanics*, 1957. 5
- P. A. Jensen and J. F. Bard. *Operations Research Models and Methods*. Wiley, 2003. 60
- S. M. Jensen and M. J. Martos. Inverse parameter identification for mode i multilinear cohesive laws. Student report 3rd semester of the m. sc. program design of mechanical systems, Department of Mechanical and Manufacturing Engineering, Aalborg University, 2016. 7, 55, 65, 71
- R. K. Joki, F. Grytten, B. Hayman, and B. F. Sørensen. Determination of a cohesive law for delamination modeling - accounting for variation in crack opening and stress state across the test specimen width. In *Composite Science and Technology*. 89
- R. M. Jones and K. S. Devens. *Mechanics of Composite Materials*. Materials Science and Engineering Series. Taylor & Francis Group, second edition, 1998. 28
- A. Kildegaard. *Elasticitetsteori*. 2013. 13
- F. Laurin, L. S. Charrier, D. Lévêque, J. F. Maire, and P. Núñez. Determination of the properties of composite materials thanks to digital image correlation measurements. *Elsevier*, pages 106–115, 2012. 108

-
- E. Lund and L. C. T. Overgaard. First ply failure analysis using max stress and strain criteria. In *Master Course Notes: Mechanics of Composite Materials and Structures, Exercise 6 notes*, 2016. LaTeX slides. 28
- L. E. Malvern. *Introduction to The Mechanics of a Continuous Medium*. Prentice-Hall, Inc., 1969. 11, 14
- Inc. MathWorks. *Optimization Toolbox User's Guide*. The MathWorks, Inc., September 2016. 57
- A. Needleman. A continuum model for void nucleation by inclusion debonding. *Journal of Applied Mechanics*, 54((3)):525–531, 1987. 6
- J. Nocedal and S. J. Wright. *Numerical Optimization*. Springer Science+Business Media, LLC., second edition, 2006. doi: 10.1007/978-0-387-40065-5. 57, 59
- L. C. Overgaard and E. Lund. Failure modes in composite materials, part 1. In *Master Course Notes: Mechanics of Composite Materials and Structures*. Department of Mechanical and Manufacturing Engineering, Aalborg University., February 2014. 3
- L. C. T. Overgaard, E. Lund, and P. P. Camanho. A methodology for the structural analysis of composite wind turbine blades under geometric and material induced instabilities. *Computers & Structures*, 88(19-20):1092–1109, 2010. 27, 38, 42, 43
- J. R. Rice. A path independent integral and the approximate analysis of strain concentration by notches and cracks. *Journal of Applied Mechanics*, 35:379–386, 1968. 5, 29
- R. Robere. Interior point method and linear programming. *University of Toronto*, 2012. 60
- C. Sarrado, A. Turon, J. Renart, and I. Urresti. Assessment of energy dissipation during mixed-mode delamination growth using cohesive zone models. *Elsevier Composites: Part A*, pages 2128–2136, 2012. 29, 30
- B. F. Sørensen and P. Kirkegaard. Determination of mixed mode cohesive laws. *Engineering Fracture Mechanics*, 73:2642–2661, 2006. 6, 8, 78, 79, 108
- S. M. Spearing and A. G. Evans. The role of fiber bridging in the delamination resistance of fiber-reinforced composites. *Acta metall. mater.*, 40(9):2191–2199, 1992. 78
- A. Turon, P.P Camanho, J. Costa, and C.G. Davila. A damage model for the simulation of delamination in advanced ccomposite under variable-mode loading. *Mechanics of Materials*, 38:1072–1089, 2006. 5, 6, 11, 12, 21, 28, 29, 30, 31, 33, 38, 77
- A. Turon, P.P. Camanho, J. Costa, and J. Renart. Accurate simulation of delamination growth under mixed-mode loading using cohesive elements: Definition of interlaminar strength and elastic stiffness. *Elsevier Composites Structures*, pages 1857–1864, 2010. 30
- V. Tvergaard and J. W. Hutchinson. The relation between crack growth resistance and fracture process pparameter in elastic-plastic solids. *Journal of the Mechanics and Physics of Solids*, 40(6):1377–1397, 1992. 6, 77
- R. A. Waltz, J. L. Morales, J. Nocedal, and D. Orban. An interior algorithm for nonlinear optimization that combines line search and trust region steps. *Mathematical Programming, Ser. A*(107):391–408, 2006. 57, 58, 59, 92